

**Fog in Indo-Gangetic Plains: Climatology, Detection, and
Forecasting using Data-Driven Methods**

A Thesis

Submitted in Partial Fulfilment

of the Requirements For the Degree of

Doctor of Philosophy

by

DESHPANDE PRASAD JAYANT

17103270

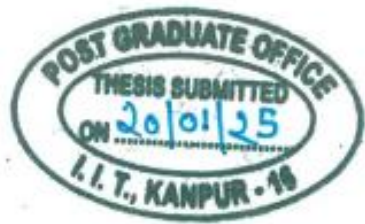


To

DEPARTMENT OF CIVIL ENGINEERING

INDIAN INSTITUTE OF TECHNOLOGY KANPUR

January, 2025



Certificate

It is certified that the work contained in the thesis titled "Fog in Indo-Gangetic Plains: Climatology, Detection, and Forecasting using Data-Driven Methods," by Deshpande Prasad Jayant (17103270) has been carried out under my supervision and that this work has not been submitted elsewhere for a degree.

Shivam Tripathi
Professor
Department of Civil Engineering
Indian Institute of Technology Kanpur
Kanpur 208016 (INDIA)

January 16, 2025

Declaration

This is to certify that the thesis titled

**Fog in Indo-Gangetic Plains: Climatology, Detection, and Forecasting
using Data-Driven Methods**

.....
has been authored by me. It presents the research conducted by me under
the supervision of.....**Prof. Shivam Tripathi**.....

To the best of my knowledge, it is an original work, both in terms
of research content and narrative, and has not been submitted elsewhere,
in part or in full, for a degree. Further, due credit has been attributed to
the relevant state-of-the-art and collaborations (if any) with
appropriate citations and acknowledgements, in line with established
norms and practices.



Signature

Name:.....**Deshpande Prasad Jayant**.....

.... Programme:PhD/MTech/MDes

Department:.....**Civil Engineering**.....
.. Indian Institute of Technology
Kanpur

Kanpur 208016

ABSTRACT/SYNOPSIS

Name:	Deshpande Prasad Jayant
Roll no.:	17103270
Degree for which submitted:	Doctor of Philosophy
Department:	Civil Engineering (Hydraulics and Water Resource Engineering)
Thesis Title:	Fog in Indo-Gangetic Plains: Climatology, Detection, and Forecasting using Data-Driven Methods
Thesis supervisor:	Prof. Shivam Tripathi
Month and year of thesis submission:	January 2025

Dense fog frequently blankets the Indo-Gangetic Plains (IGP) during winter, significantly impacting transportation, agriculture, and public health. Accurate fog detection and forecasting help in mitigating its adverse impacts. This study uses data-driven methods for understanding fog climatology, detecting fog using satellite data and forecasting it.

First, long-term meteorological observations (1991–2020) from seven cities are analyzed to identify fog events, classify them based on formation mechanisms, and study their spatial-temporal characteristics. Results show that ~84% of fog events are radiation fog, while ~13% are advection fog, with January being the peak month for fog occurrences. Spatially, fog onset exhibits an east-west trend, while northern cities show relatively more intense fog events. Seasonal fog hours show a higher inter-annual variability, while durations of fog events exhibit inter-city variability.

Second, a Bayesian neural network is developed that uses INSAT-3D satellite observations to detect probability of fog. The model is developed using data from eighteen cities

from 2017-2022. The model quantifies detection uncertainty and separates its epistemic and aleatoric components. The model outperforms the operational INSAT-3D Fog product, achieving a critical success index (CSI) of 0.48 compared to 0.12 for INSAT-3D Fog. The model could correctly detect more than 90% of very dense fog observations (visibility < 50 m). The uncertainty analysis reveals that the aleatoric uncertainty is usually higher than the epistemic uncertainty, suggesting potential avenues for future improvements.

Finally, a Bayesian neural network-based fog forecasting model named FogCast is developed using the outputs from a machine learning global weather prediction model, GraphCast. The proposed model forecasts fog/no-fog with lead times ranging from 6 hours to 10 days. The model is developed using data for seven cities from 2017-2023. The model achieves CSI values between 0.44 (for 6-hour lead time) to 0.36 (for 10-day time) and can correctly detect over 90% of very dense fog observations. This data-driven approach offers a promising tool for improving fog forecasting capabilities in the IGP region.

Dedicated to
Late Prof. Sameer Khandekar

Acknowledgement

Foremost, I would like to express my profound gratitude to my thesis supervisor, Dr. Shivam Tripathi, for his motivation, encouragement, constant support, and exemplary guidance. His enthusiasm and insights have been a great source of inspiration throughout my journey at IIT Kanpur. It was truly a memorable and enriching experience to work under his supervision.

I extend my sincere thanks to all the HWRE faculty members in the Department of Civil Engineering — Dr. Rajesh Srivastava, Dr. Ashu Jain, Dr. Saumyen Guha, Dr. Richa Ojha, Dr. Gourabananda Pahar, Dr. Tushar Apurv, Dr. Chunendra K. Sahu, and Dr. Shubhadip Das — for their valuable teachings and guidance. I also thank Dr. Onkar Dikshit, Dr. S.N. Tripathi, Dr. Bharat Lohani, Dr. Suparno Mukhopadhyay, Maj. Gen. (Dr.) B. Nagarajan, and Dr. Balaji Devraju from Civil Engineering, along with Dr. Vipul Arora (Electrical Engineering), Dr. Piyush Rai (Computer Science and Engineering), and other faculty members whose lectures helped me build the skills essential for this work.

I am grateful to Dr. Arnab Bhattacharya (Computer Science and Engineering) and Dr. M.K. Verma (Physics), and all members of the Fog Prediction group at IIT Kanpur. I would also like to acknowledge the support of Sunil Ji, Deepak Ji, and the Hydraulics Lab staff. My thanks also go to Dr. Anurag Tripathi (Chemical Engineering) and Dr. Vinod Tare for giving me opportunities to engage in co-curricular activities.

I am especially thankful to my seniors — Dr. Anudeep Sure, Dr. Aniruddha Katti, Dr. Vinayak Bhanage (IITB), and Dr. Harshal Kulkarni (IITR) — for their guidance and motivation. I would also like to thank my colleagues and friends Ishank Agarwal, Pravesh Singh, Saurabh Kumar, Vishal Singh, Ravi Shukla, and Anirudh Belwalkar for their friendship and support.

During my time at IIT Kanpur, I've been fortunate to be surrounded by amazing people who made my non-research hours equally memorable. Special thanks to Sanket, Madhu, Umang, Isha, and other Scavenger friends, Ashwani, Bandopant, Vivek Kumar Sahu, Nitin, and others from Saptahik Milan, Mahesh Ji and others from the Adventure Club, Vitthal, Ganesh,

Abhishek Gidde from Maharashtra Mandal, and Saurav Bhattacharjee from the History Society, as well as the volleyball group. I also feel fortunate to have had the chance to attend numerous guest lectures and concerts (especially Indian classical music), which enriched my time at IITK.

I express my sincere appreciation to the mess and canteen workers, cleaners, dhobis, SIS security staff, Health Center doctors, and cab drivers who played a vital role in making my stay at Hall 11 and SBRA comfortable and worry-free.

Lastly, I have no words to express my gratitude to my parents, to whom I owe everything. A special mention goes to my wife, Gauri, whose unwavering love and support made this journey so much smoother. Her encouragement has been my greatest strength. I also extend heartfelt thanks to my entire family for their constant support and blessings.

This journey has further strengthened my commitment to research and its potential to serve humanity, and I look forward to continuing along this path with purpose and passion.

Thank you IIT Kanpur.

Table of Contents

Acknowledgement	vii
Table of Contents	ix
List of Figures	xii
List of Tables	xiv
1 INTRODUCTION	1
1.1 Background.....	1
1.2 Fog and atmospheric visibility.....	2
1.3 Datasets for monitoring and modelling fog	3
1.3.1 <i>In situ</i> observations.....	3
1.3.2 Remote sensing of fog	4
1.3.3 Numerical Weather Prediction (NWP) models	5
1.4 Types of fog.....	6
1.4.1 Based on formation	6
1.4.2 Based on visibility range	7
1.4.3 Based on onset time.....	7
1.5 Motivation	8
1.6 Objectives	8
1.7 Organization of the Thesis.....	9
2 FOG CHARACTERIZATION	10
2.1 Introduction	10
2.2 Study area and datasets	13
2.3 Methodology.....	15
2.3.1 Identification and removal of low visibility no-fog episodes.....	15
2.3.2 Extraction of fog events	15
2.3.3 Missing data imputation	17
2.3.4 Fog typology	18
2.3.5 Analysis of fog events	19
2.4 Results of fog climatology and typology.....	19
2.4.1 Intra-seasonal distribution of fog events	20
2.4.2 Diurnal distribution of fog events	21
2.4.3 Fog typology	25
2.4.4 Transition probabilities for fog events	26
2.4.5 Duration of fog events	27
2.4.6 Inter-event duration	29

2.4.7	Inter-seasonal distribution of fog events	30
2.4.8	Fog event climatology	34
2.5	Discussion.....	38
2.5.1	Inferences from the analysis.....	38
2.5.2	Comparison of fog in IGP with other parts of the world.....	39
2.6	Chapter summary.....	40
3	SATELLITE FOG DETECTION	42
3.1	Introduction	42
3.2	Study area and datasets.....	45
3.3	Methodology.....	46
3.3.1	Theoretical background of Bayesian neural networks	46
3.3.2	Reliability of the proposed model	49
3.3.3	Feature engineering	49
3.3.4	Model implementation	51
3.3.5	Sensitivity analysis for hyperparameters.....	52
3.4	Results	52
3.4.1	Model results	53
3.4.2	Comparison with baseline	55
3.4.3	Uncertainty analysis	57
3.4.4	Classification results for different subsets.....	58
3.5	Discussion.....	61
3.6	Chapter summary.....	63
4	MEDIUM-RANGE FOG FORECASTING.....	65
4.1	Introduction	65
4.2	Datasets and study area.....	68
4.3	Methodology.....	70
4.3.1	Model architecture.....	70
4.3.2	Training and testing.....	70
4.3.3	Feature importance analysis	71
4.4	Results and discussion	71
4.4.1	Model evaluation.....	71
4.4.2	Model evaluation for visibility-based fog categories	74
4.4.3	Uncertainty analysis	75
4.4.4	Feature importance	76
4.4.5	Realism of FogCast forecasts	79
4.4.6	Further discussion	81

4.4.7	Limitation and future scope.....	82
4.5	Chapter summary.....	83
5	SUMMARY AND CONCLUSION.....	85
5.1	Summary.....	85
5.2	Future directions	86
5.2.1	Development of low-cost sensors and citizen science.....	87
5.2.2	Relationship between fog and agriculture	87
5.2.3	Improved dissemination of fog forecasts	87
	REFERENCES.....	89
	APPENDIX	103
	A 1 Appendix 1	103
	A 2 Appendix 2	104
	A 2.1 Data availability and interpolation	104
	A 2.2 Sensitivity of M-of-N events.....	105
	A 2.3 Boxen-plots and violin-plots	106
	A 2.3.1 Boxen-plots	106
	A 2.3.2 Violin-plots.....	107
	A 2.4 Correlations of inter-seasonal distribution of fog events	109
	A 3 Appendix 3	110
	A 3.1 Comparison of INSAT-3D Fog with <i>in situ</i> visibility observations.....	110
	A 3.2 Additional details of the Bayesian neural network.....	111
	A 3.3 Effect of hyperparameters on model performance	112
	A 3.3.1 Number of past observations as input	112
	A 3.3.2 Effect of KL-weight	113
	A 3.3.3 Effect of prior distribution.....	114
	A 3.3.4 Effect of training proportion.....	115
	A 3.4 Combined effect of prior distribution and KL-weight hyperparameter	116
	A 3.5 Fog detection images generated by proposed model.....	117
	A 4 Appendix 4	119
	A 4.1 Past studies related to fog forecasting	119
	A 4.2 FogCast performance with and without lagged input features.....	125
	A 4.3 Model performance during LOOCV	125
	A 4.4 Reliability diagram.....	126

List of Figures

Figure 1.1. A visibility sensor installed at IITK Fog Observatory, IIT Kanpur, India.	3
Figure 2.1. Seven cities selected for the fog characterisation.	13
Figure 2.2. Illustration of fog event identification.	16
Figure 2.3. Algorithm for fog typology based on fog formation process.	18
Figure 2.4. Heatmap showing the percentage of fog events.	21
Figure 2.5. Heatmaps showing (a) fog onset, (b) dissipation timings of fog events, (c) probability (percentage) of the presence of fog during each hour of a day.....	23
Figure 2.6. (a) Formation-based fog classification, (b) Visibility-based fog classification, (c) Onset time-based fog classification.	24
Figure 2.7. Transition probabilities for the visibility-based fog types.	27
Figure 2.8. Duration of fog events for visibility-based fog types.	28
Figure 2.9. Violin-plots showing the duration of fog events based.	28
Figure 2.10. Duration between the onset of two fog events.....	29
Figure 2.11. Time-series of characteristics of fog events.	32
Figure 2.12. Maximum and minimum temperature distribution for different cities.	33
Figure 2.13. Boxen-plots showing temperature distributions during fog and no-fog conditions.	33
Figure 2.14. Boxen-plots showing relative humidity distributions fog and no-fog conditions... ..	33
Figure 2.15. Temperature and relative humidity distribution for visibility-based fog types.	33
Figure 2.16. Distribution of wind direction during fog and no-fog scenario.	36
Figure 2.17. Land cover around the weather stations of seven cities used in the study.....	37
Figure 3.1. Locations of 18 cities in Indo-Gangetic Plains for BNN model development.	46
Figure 3.2 Proposed BNN model architecture.	52
Figure 3.3. Overall accuracy (OA) and critical success index (CSI) for different threshold probabilities for the main test dataset (solid line) and the held-out dataset (dashed line).	53
Figure 3.4. Reliability diagram showing the calibration of the proposed BNN-model.	54
Figure 3.5. Scatterplot showing the relation between aleatoric and epistemic uncertainty..	56
Figure 3.6. Model and baseline performance for different hours of the day.....	59
Figure 3.7. Variation of CSI for different cities against the proportion of fog (in %)..	60
Figure 4.1. Locations of 7 cities in Indo-Gangetic Plains used for model training and testing..	68
Figure 4.2 Flowchart showing the methodology of FogCast.	69
Figure 4.3. Bayesian neural network used in the FogCast.	71
Figure 4.4. FogCast performance for different lead times.	73
Figure 4.5. Scatterplot for aleatoric and epistemic uncertainty.....	75
Figure 4.6. (a) Feature importance plot showing the input features in descending order of feature importance. (b,c,d,e) Scatterplots for feature value and corresponding SHAP value	77
Figure 4.7 Probability of fog for 4 January 2025 at 5:30 am IST, forecasted by FogCast.	80
Figure 4.8 INSAT-3D Fog map for 4 January 2025 at 5:30 am IST.	80

Appendix Figures

Figure A2.1 Distribution of missing values in METAR	105
Figure A2.2 Boxen-plot using quantiles.....	107
Figure A2.3 Components violin-plot	108
Figure A3.1 Effect of the number of past observations as input to model on CSI.....	112
Figure A3.2 Effect of KL-weight hyperparameter on CSI.....	113
Figure A3.3 Effect of standard deviation of prior distribution on CSI.....	114
Figure A3.4 Effect of the size of training dataset on CSI.....	115
Figure A3.5 Contour plot showing the ELBO values.....	116

Figure A3.6 Probability of fog detected by the proposed BNN model	117
Figure A3.7 Epistemic and aleatoric uncertainties by the BNN model.....	118
Figure A4.1 Reliability diagram of FogCast.....	126

List of Tables

Table 1.1. Details of the different bands of INSAT-3D satellite and INSAT-3D Fog.	5
Table 1.2. Visibility-based fog classification as per WMO.	7
Table 2.1. Location of the weather stations at seven cities used in the characterisation study...	13
Table 2.2. A summary of fog event comparison in IGP with other regions of the world.....	39
Table 3.1. Confusion matrix for the proposed BNN.	53
Table 3.2. Quantitative results of proposed BNN and baseline.	55
Table 3.3. Various statistics related to uncertainty analysis.	56
Table 3.4. Model performance by limiting total uncertainty.	56
Table 3.5. Model performance for different visibility-based fog-categories.	59
Table 4.1. Model performance for fog forecasting averaged over all lead times.....	73
Table 4.2. Model performance for different visibility-based fog categories for 6-hour and 10-day lead times and all seven cities during testing.	74
Table 4.3. Various statistics related to uncertainty analysis.	75
Table 4.4. Model performance for a severe fog event in Delhi (India) on 14th January 2022..	78
Table 4.5. Comparison of fog forecast from FogCast, INSAT-3D Fog, and METAR	81

Appendix Tables

Table A1.1. Visibility-based fog classification as per Indian Railways	101
Table A1.2. Minimum visibility requirements for airport categories as per ICAO	101
Table A2.1. Summary of the datasets used in the characterization of fog in IGP.....	105
Table A2.2. Sensitivity of the number of events identified by the M-of-N algorithm.....	106
Table A2.3. Boxen-plot quantiles.....	107
Table A2.4. Correlation among seasonal values of fog characteristics.....	109
Table A3.1. Comparison of in situ (METAR) fog observations with INSAT-3D Fog.....	111
Table A3.2. Implementation details of the BNN model.....	111
Table A4.1. Comparison of past fog forecasting studies.....	119
Table A4.2. Comparison of model performance with and without lagged features.....	125
Table A4.3. Model performance for different cities by LOOCV.....	125

LIST OF ABBREVIATIONS

ANN – Artificial Neural Network

AUROC – Area under the Receiver Operating Characteristic

BLSTM – Bayesian Long Short-Term Memory

BNN – Bayesian Neural Network

BT – Brightness Temperature

BTD – Brightness Temperature Difference

CSI – Critical Success Indices

CSIR – Council of Scientific and Industrial Research (India)

CV – Coefficient of Variation

ECE – Expected Calibration Error

ELBO – Evidence Lower Bound

FN – False Negative (miss)

FP – False Positive (false alarm)

GMT – Greenwich Mean Time

IFS – Integrated Forecast Systems by ECMWF

IGP – Indo-Gangetic Plains

IEM – Iowa Environmental Mesonet

IITK – Indian Institute of Technology Kanpur

INR – Indian National Rupee

INSAT-3D Fog – INSAT-3D Derived Binary Fog

INSAT-3D – INSAT-3D Geostationary Satellite

IMD- India Meteorology Department

ISRO – Indian Space Research Organization

IST – Indian Standard Time

KL Divergence – Kullback-Leibler Divergence

LOOCV – Leave-One-Out Cross-Validation

LLM – Large Language Model

METAR – METeorological Aerodrome Reports

MOR – Meteorological Optical Range

NCEI – National Centre for Environmental Information

NDVI – Normalized Difference Vegetation Index

NOAA – National Oceanic and Atmospheric Administration

NWP – Numerical Weather Prediction

MLWP – Machine Learning (or AI-driven) Weather Prediction

MIR – Middle InfraRed band ($3.9 \mu\text{m}$ wavelength)

OA – Overall Accuracy

PoD – Probability of Detection

RAM – Random Access Memory

RNNs – Recurrent Neural Networks

RMSE – Root Mean Square Error

ReLU – Rectified Linear Unit

RVR – Runway Visual Range

SHAP – SHapley Additive exPlanations

SWIR- Shortwave InfraRed band ($1.6 \mu\text{m}$ wavelength)

TFP – TensorFlow Probability

TIR1 – Thermal InfraRed 1 band ($10.8 \mu\text{m}$ wavelength)

TIR2 – Thermal InfraRed 2 band ($12.0 \mu\text{m}$ wavelength)

TN – True Negative (correct negative)

TP – True Positive (hit)

TRMM- TMPA–Tropical Rainfall Measuring Mission Multisatellite Precipitation Analysis

UAE – United Arab Emirates

USD – United States Dollar

VIS – Visible spectrum band ($0.6 \mu\text{m}$ wavelength)

WMO – World Meteorological Organisation

WRF – Weather Research and Forecasting model

WVIR – Water Vapour InfraRed band ($6.7 \mu\text{m}$ wavelength)

1 INTRODUCTION

1.1 Background

Fog is a common and disruptive weather event, particularly during the winter months (November to February) in the Indo-Gangetic Plains (IGP) of northern India. It causes severe disruptions to transportation services- air, rail, and road- leading to delays, cancellations, and an increased risk of accidents. These interruptions have considerable economic consequences. For example, fog-related disruptions at Delhi airport alone resulted in losses exceeding 3000 Crore INR (~3.9 billion USD) between 2011 and 2016 (Kulkarni et al., 2019). Besides transportation, fog also contributes to hazardous smog when combined with smoke, creating additional health risks (Terry et al., 2018). Prolonged foggy days are associated with seasonal depression and gloom, further affecting public health (Zheng et al., 2024).

Fog's impact extends beyond transportation and health. In agriculture, it restricts sunlight, reducing the amount of photosynthetically active radiation, which is essential for plant growth (Shrestha et al., 2018). On the other hand, it also supplies dew, which provides moisture for vegetation growth in the absence of rainfall. Though the quantity of fog water may seem to be often neglected in hydrological modelling, it may sometimes be considerable, especially in water-limited environments (Li et al., 2018; Qiao et al., 2020; Wang et al., 2019).

Despite its relatively low probability of occurrence, fog has a high disaster potential, especially in densely populated regions like the IGP, which is home to nearly one-seventh of the world's population. Accurate fog monitoring and timely fog forecasts are, therefore, vital in minimising its adverse effects. Fog monitoring and forecasting are directly linked to two of the United Nations Sustainable Development Goals (UN-SDGs): "Climate Action" and "Sustainable Cities and Communities," while also supporting "Good Health and Well-being" and "Decent Work and Economic Growth." Accurate fog monitoring and forecasting requires understanding the nature of fog and its climatology.

This chapter presents the definitions of fog and atmospheric visibility, methods of monitoring and modelling fog, and discusses types of fog. The chapter concludes with the motivations, objectives and layout of this thesis.

1.2 Fog and atmospheric visibility

Fog is a suspension of tiny, usually microscopic water droplets in the air, reducing visibility at the Earth's surface. The term 'fog' is used when microscopic droplets reduce horizontal visibility at the Earth's surface to less than 1 km; otherwise, it is mist (WMO, 2011). Another approach to identifying fog is through the deposition of water droplets on the fog collector. The first approach is more relevant to studies relating fog to the transportation sector, whereas the second approach is related to studies dealing with fog as a freshwater source.

Atmospheric visibility is the most important proxy for fog. It refers to the greatest distance in the horizontal direction at which objects can be discerned visually. It is measured in length units. Visibility can be measured manually or using automated visibility sensors (i.e., visiometers, visibilimeters, transmissometers). A visibility sensor consists of an emitter and receiver of light sources, and attenuation of light due to both absorption and scattering by the particles in the air along the path of light are measured in terms of extinction coefficient. The extinction coefficient is converted to visibility using Koschmieder's Law at daytime and Allard's Law at nighttime (Gultepe et al., 2007). Technically, visibility sensors measure the Meteorological Optical Range (MOR), i.e., the distance required in the atmosphere to reduce the light from a standard lamp to 5% of its original value, measured using a specific photometric method. World Meteorological Organisation (WMO, 2011) defines MOR as: "the length of path in the atmosphere required to reduce the luminous flux in a collimated beam from an incandescent lamp, at a colour temperature of 2700 K, to 5 per cent of its original value, the luminous flux being evaluated by means of the photometric luminosity function of the International Commission on Illumination." For aviation sector, the surface MOR is measured at a height of 2.5 m above the ground surface. MOR is also sometimes referred to as general

visibility or meteorological visibility. In this thesis, it referred to as visibility. A photograph of a visibility sensor installed at IITK Fog Observatory is shown in Figure 1.1.



Figure 1.1. A visibility sensor installed at IITK Fog Observatory, IIT Kanpur, India.

1.3 Datasets for monitoring and modelling fog

1.3.1 *In situ* observations

Visibility is a crucial factor for airport operations; thus, airports maintain historical records visibility along with other hydrometeorological observations such as METAR records. METAR, i.e., Meteorological Aerodrome Reports, are standardised formats for reporting real-time weather conditions at airports. These reports are usually published in the public domain at a half-hourly frequency. METAR observations include key parameters such as visibility, air temperature 2m above ground, dew point temperature, relative humidity, rainfall, wind speed and direction. The visibility data in METAR reports is crucial for fog forecasting, as it helps monitor current fog conditions and assess fog intensity.

In this thesis, the METAR data are acquired from the Iowa Environmental Mesonet (IEM) archive (IEM, 2021) an automated airport weather observation collection website that offers real-time data for airports worldwide. This platform obtains data from the National Centre for Environmental Information (NCEI), a repository maintained by the National Oceanic and Atmospheric Administration (NOAA). Since the METAR records are based on *in situ* observations and are considered reliable, they are selected as a source of *in situ* observations in

this thesis. The METAR records from IEM datasets have been used in many climate studies, including fog studies (e.g. Stevens, 2019). In India, around 2010, automated visibility sensors started replacing manual observations. This increased the frequency of observations from daily twice up to half-hourly, leading to improved monitoring of fog. Drishti Transmissometer is an example of an Indigenous visibility sensor developed by CSIR-National Aerospace Laboratories that is generally used at Indian airports (Mohan et al., 2015).

1.3.2 Remote sensing of fog

The *in situ* visibility monitoring covers a limited spatial extent. They are sparse and mostly available only at airports. Satellite observations can address this problem of limited spatial coverage. Multispectral satellites are conventionally used for fog detection (Gultepe et al., 2007). However, lidar-based satellite observations have also been developed recently (Qiao et al., 2022). Satellite-based fog monitoring started in the 1990's (Gultepe et al., 2007), though the theory for fog detection using brightness temperature difference (BTD) was developed in 1973 (Hunt, 1973). The brightness temperature (BT) of an object is a measure of its radiance expressed as the temperature of a hypothetical blackbody having the same radiance at a given wavelength. BT is the measure of "hotness" of an object in the infrared part of the spectrum and is a function of the temperature of the object and wavelength. The BTD of an object is the difference between brightness temperatures of thermal infrared (TIR1; 10.8 μm) and mid-infrared (MIR; 3.9 μm) wavelength bands. Since fog droplets are smaller in size, they show lower emissivity in the MIR band, leading to a lower BT of the MIR band as compared to the BT of the TIR1 band. The combined effect of lower wavelength and lower emissivity of the MIR band leads to negative BTD in the presence of fog. However, this relationship remains valid during nighttime only as during the daytime; solar radiation also contributes to the MIR1 band without affecting TIR1. Thus, during daytime, the BTD is positive in the presence of fog. When the fog is absent, the BTD is nearly zero or slightly positive (due to the contribution of solar radiation). The high clouds (e.g. cirrus) are extremely cold (sometimes below -50° C), hence they can be identified using the TIR1 band easily (Gultepe et al., 2007).

Both polar-orbiting satellites (e.g., MODIS) and geostationary satellites (e.g., INSAT-3D, Himawari) commonly comprise TIR1 and MIR bands, making them suitable for fog detection. While both types of satellites can be used for this purpose, geostationary satellites offer the advantage of real-time observations at an hourly scale, unlike polar-orbiting satellites. Therefore, observations from geostationary satellites are used in this thesis.

Currently, fog monitoring is carried out in India using the Indian Space Research Organization's (ISRO) fog product (INSAT-3D Fog). It provides binary fog status with 4 km spatial resolution at every half-hour frequency using a conventional threshold-based fog detection algorithm (ISRO, 2015). INSAT-3D Fog is derived from the INSAT-3D geostationary satellite, which was built by ISRO and launched in 2013. The satellite has a repeat period of 30 minutes. INSAT-3D standard product has six bands (Table 1.1) viz., VIS, SWIR, MIR, WVIR, TIR1, and TIR2 (ISRO, 2015).

Table 1.1. Details of the different bands of INSAT-3D satellite and INSAT-3D Fog.

Band	Description	Wavelength (μm)	Spatial resolution (km)
VIS	Visible	0.6	1
SWIR	Shortwave infrared	1.6	1
MIR	Middle infrared	3.9	4
WVIR	Water vapour infrared	6.7	8
TIR1	Thermal infrared 1	10.8	4
TIR2	Thermal infrared 2	12.0	4
INSAT-3D Fog	Derived fog product	-	4

1.3.3 Numerical Weather Prediction (NWP) models

Numerical Weather Prediction (NWP) models use mathematical relationships of the atmosphere and land and ocean to simulate and forecast future weather conditions. Recent studies claim that machine learning weather prediction (MLWP) models, e.g., FourCastNet, GraphCast, GenCast, can outperform conventional NWP models (Kurth et al., 2023; Lam et al., 2023; Price et al., 2024).

NWP and MLWP models play a critical role in fog research, even though they do not directly forecast fog or visibility. These models provide forecasts of key atmospheric variables

such as temperature, humidity, wind speed, and surface pressure, which are essential for diagnosing and forecasting fog formation (Menut et al., 2014). A popular NWP model, Weather Research and Forecasting (WRF) model is routinely used for fog modelling and forecasting (Parde et al., 2022). Various parameterization schemes (Long et al., 2021) and thresholding techniques (Singh et al., 2018) have been proposed for estimating fog (or visibility) using the WRF outputs. Moreover, NWP models coupled with other datasets (e.g., soil moisture; Smith et al. 2024) are also being explored.

1.4 Types of fog

Fog can be classified in various ways, depending on the application or objectives of the study. For instance, classifying fog based on onset time is particularly useful for traffic management and planning. In contrast, visibility-based classification relies on the optical thickness of fog and is linked to the freshwater potential of fog. Additionally, the physical processes driving the formation and dissipation of fog serve as the basis for classification by formation mechanism. Thus, the typology of fog helps us understand the patterns of fog, which can be translated into data science models for fog forecasting. Below are a few key classification types.

1.4.1 Based on formation

1. *Radiation Fog*: Radiation fog forms on cold, clear nights when heat radiates away from the ground, cooling the surface and nearby air. When the temperature drops below the dew point, fog forms near the ground, typically extending a few meters. It usually dissipates as the sun warms the surface in the morning.
2. *Advection Fog*: Advection fog occurs when warm, moist air is pushed inland by the wind over cooler ground or water surfaces. As the air cools to its dew point, fog forms, often covering large areas.
3. *Valley Fog*: In valleys, advection fog can extend up to 500 m above ground level. Due to the weak winter sun, it may not evaporate fully but can lower in height as the ground warms slightly. This fog can persist for days until strong winds from a storm clear it away.

4. *Upslope Fog*: Cold air is pushed up hills or mountains by winds, cooling as it ascends. Once the air reaches its dew point, fog forms, drifting upward along the slope.

5. *Steam Fog*: This fog forms when cold air moves over a much warmer water surface, causing water to evaporate into the cooler air. As the air reaches its dew point, it condenses into fog.

6. *Precipitation Fog*: When warm rain falls into cooler air, some of it evaporates, increasing the air's dew point. This added moisture causes vapor to condense into tiny fog droplets.

A detailed discussion on various fog types and factors influencing fog is presented in Lakra and Avishek (2022).

1.4.2 Based on visibility range

India Meteorological Department (IMD) and WMO classify fog based on visibility range as per Table 1.2. Similar classification schemes exist in other countries as well (e.g., USA, Japan), but the thresholds on visibility range may vary. Tables A 1.1 and A 1.2 in Appendix A.1 show the visibility-based fog classification used by Indian Railways and International Civil Aviation Organization (ICAO).

Table 1.2. Visibility-based fog classification as per WMO.

Type of fog based on visibility	Visibility range (m)
Shallow (Light)	500 to 1000
Moderate (Medium)	200 to 500
Dense (Thick)	50 to 200
Very dense (Very thick)	0 to 50

1.4.3 Based on onset time

Fog is classified as day-fog and night-fog based on its onset time. If the onset is after sunrise and before sunset, it is classified as a day-fog. Otherwise, it is a night-fog.

1.5 Motivation

Fog formation is an intricate and unresolved process driven by the interaction of moisture, aerosols, and wind. Fog forecasting is especially challenging due to its sporadic nature and a combination of local and large-scale climate processes that influence its development. The mechanisms behind fog formation vary by region, which makes creating universally applicable models difficult. Since fog affects both the water cycle and Earth's radiation balance, its study is critical for advancing climatology and meteorology. However, fog's dynamic and multifaceted nature complicates efforts to model and forecast it accurately.

Fog is studied from various perspectives. Meteorologists focus on improving fog forecasts through NWP models (Pithani et al., 2020), while air quality experts examine its chemical properties. Agriculturalists assess fog's impact on crop growth, and hydrologists estimate the potential for fog water collection, which serves as a valuable source of freshwater in some regions (Kaseke and Wang, 2012; Klemm et al., 2012). Meanwhile, novel algorithms are being developed to improve large-scale fog monitoring using earth observation satellites. Some studies have analysed individual fog events by conducting hydro-meteorological measurements at various heights to understand the physical processes behind fog formation (Ghude et al., 2017). The insights from such experiments are integrated into NWP models to enhance forecast accuracy. However, NWP models often fail to capture the intricacies of fog formation limiting their forecasting accuracy (Wagh et al., 2023). Fortunately, data science provides a promising method for studying fog. A large amount of data on fog, moisture, temperature, wind, etc. are now available. The motivation of this study is to investigate the utility of these datasets for developing data science models for real-time fog detection and forecasting.

1.6 Objectives

The thesis explores data science, i.e., machine learning (ML) applications for monitoring and forecasting fog using *in situ*, remote sensing observations and Machine Learning Weather Prediction models (MLWP). Initially, the characterization of fog in IGP is carried out to

understand the nature of fog. Then, the models for fog monitoring and forecasting are developed. Considering the implications of fog on transportation sector, this thesis aims to develop practical, real-time methods for fog monitoring, forecasting, and disseminating forecasts to the public. The main objectives of the thesis are as follow:

- (i) To understand the climatology and typology of the fog to identify relevant features and variables for fog forecasting.
- (ii) To develop a probabilistic satellite fog detection model using INSAT-3D observations.
- (iii) To develop FogCast, a medium-range (10 days lead time) fog forecasting model.

The dynamic and heterogeneous nature of fog can be more accurately detected and forecasted using uncertainty-aware models. Therefore, Bayesian Neural Networks (BNNs), capable of estimating uncertainty are utilised for satellite fog detection and forecasting in this thesis. Background information and further details on BNNs are presented in Chapter 3.

1.7 Organization of the Thesis

This thesis is composed of 5 chapters. Chapter 1 introduces the importance of fog monitoring and forecasting in IGP. It also contains the motivation and objectives of the thesis. Chapter 2 analyses the characteristics of fog in IGP using *in situ* observations. Chapter 3 develops a probabilistic satellite fog detection model using INSAT-3D observations. Chapter 4 develops FogCast, a spatial fog forecasting model using outputs of global weather prediction model. Chapter 5 summarises and concludes the thesis.

This chapter is a modified version of an article (under review) with the following details:

Deshpande, P., Bhattacharya, A., & Tripathi, S. (2025). Data-Driven Fog Forecasting for North India, *Current Science*.

2 FOG CHARACTERIZATION

2.1 Introduction

Fog characterization includes studying climatology and typology of fog. Fog climatology explores long-term patterns, frequency, distribution, and environmental factors influencing fog formation, persistence, and dissipation in a specific region. The approach to studying fog climatology differs according to the study objectives and data availability. The study of fog climatology typically involves analysing observed climate data for single or multiple locations. The analysis is usually performed on visibility data to identify foggy days and investigate their trends (Syed et al., 2012), spatial variability and relationship with other climate variables (Izett et al., 2019). In such studies, the intraday variation of fog is not considered. Alternatively, some studies analyse hourly or sub-hourly visibility observations to investigate the nature or type of fog (Roux et al., 2021), the duration of fog (Cséplő et al., 2019), and the role of local factors (e.g., terrain, land cover, proximity to sources of moisture) in the formation, evolution, and dissipation of fog (Akimoto & Kusaka, 2015). In the following paragraphs, we review recent fog climatology studies, particularly those over the Indian sub-continent, to highlight the gaps in the literature.

The first type of fog climatology studies, i.e., studies that do not consider intraday variations of fog, are the most common. They study long-term trends in fog occurrence (Húnová et al., 2020) or relate fog occurrence to external climate factors (Izett et al., 2019) to predict fog. Kutty et al. (2019) and Srivastava et al. (2017) studied fog trends over single cities, namely, Bengaluru and Ghaziabad, respectively. India Meteorological Department (IMD) data, which have lots of missing observations, are often used in such studies, but the imputation methodology is seldom discussed. While most of the fog climatology studies are limited to a single city, a few regional studies of fog climatology have also been reported (Hingmire et al., 2019; Kutty et al., 2020; Sawaisarje et al., 2014; Syed et al., 2012). All these studies identified fog at daily or monthly scales without considering intra-day variation in fog. Such approaches

tend to exaggerate the actual duration of fog, as the fog is usually present for a few hours on a foggy day (Jayakumar et al., 2021).

The second type of fog climatology studies analyse fog using sub-daily or hourly data. Over India, Jenamani (2012) studied fog at sub-daily timestep using data collected at airports. Srivastava et al., (2016) used IMD data from 1971 to 2010 over 32 cities in IGP to find fog occurrence time, trends, and spatial variability in fog during December and January.

The two types of fog climatology studies described above do not provide sufficient details to identify the mechanisms influencing the formation of fog. This limitation is addressed by the third type of fog climatology studies that identify fog events out of periodic measurements. Identifying fog events enables determining fog types (fog typology) based on fog formation. It also facilitates understanding of the physical processes governing fog onset and dissipation. Tardif & Rasmussen (2007) was among the earliest studies to present an event-based fog climatology for New York using hourly data of 20 years (1977 to 1996) collected at 17 locations. Apart from climatology, they classified fog events based on their formation using a condition-based algorithm. Akimoto & Kusaka (2015) performed a similar climatological study of fog in Japan using data from 60 locations from 2004 to 2008. The thesis proposes a simpler version (as compared to Tardif & Rasmussen, 2007) of the fog typology algorithm and compares the fog characteristics across different terrains (e.g., mountains, plains). Belorid et al. (2015) studied the distribution and long-term trends in various fog types using 3-hourly observations covering 25 years (1989 to 2013) for 24 stations in South Korea. Mohan et al. (2020) characterised fog events at 8 airport weather stations in the United Arab Emirates (UAE) using hourly data from 1995 to 2008. In a recent study from Southern Hemisphere, Roux et al. (2021) reported fog climatology at Perth Airport, Australia, using data from 2002 to 2019 available at a 10-minute frequency.

The IGP is one of the major fog-prone areas of the world (Pithani et al., 2020); however, to the best of my knowledge, an event-based fog characterisation and fog typology for

it has not been reported. Further, unlike most other fog-prone areas of the world where fog occurs throughout the year due to the presence of the coast (Tardif & Rasmussen, 2007), most of the cities in the IGP are far from the coast, and the fog season is confined only to winter months. Hence, the characteristics of fog events in IGP are expected to be significantly different from those reported for other regions. These two reasons - the absence of fog event characterization in the IGP and IGP's unique geographical setting, motivated this study.

The specific objectives of this chapter are:

- 1) Detection of fog events using observed visibility data;
- 2) Classification of fog events based on different features, namely, fog formation process, onset time, and visibility;
- 3) Investigation of fog variability at monthly, weekly, and daily scales.
- 4) Identification of typical timings of onset and dissipation of fog.
- 5) Analysis of the duration and frequency of fog events.
- 6) Comparison of fog characteristics in IGP with other fog-prone regions of the world.

To achieve these objectives, METAR observations of seven cities in IGP are analysed, enabling the study of the geographical variation of fog characteristics.

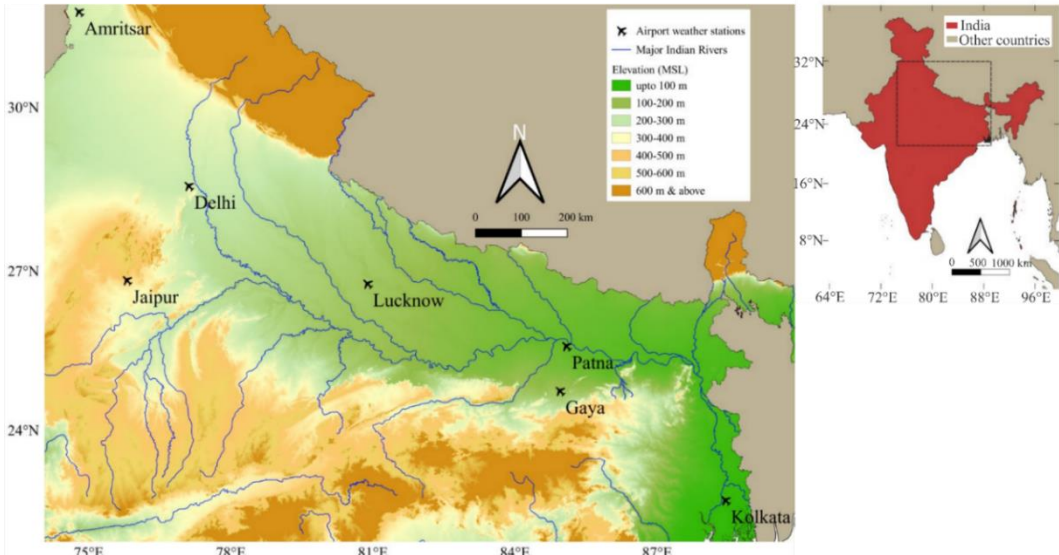


Figure 2.1. Seven cities selected for the fog characterisation with digital elevation model as background.

Table 2.1. Location and physical characteristics of the weather stations at seven cities used in the characterisation study.

City	Latitude (°N)	Longitude (°E)	Elevation (m)	Setting	Urban fraction of winter seasons	Number of winter seasons
Kolkata	22.65	88.45	5	Urban Costal	0.69	29
Gaya	24.74	84.95	116	Irrigated cropland	0.03	16
Patna	25.59	85.09	52	Urban	0.51	28
Lucknow	26.76	80.89	123	Semi-urban	0.28	26
Jaipur	26.82	75.81	385	Urban	0.65	22
Delhi	28.57	77.12	237	Urban	0.55	23
Amritsar	31.71	74.80	230	Irrigated cropland	0.02	22

2.2 Study area and datasets

Seven cities, well distributed across the IGP, are selected from 18 airport weather stations, based on data availability and criteria defined in this section. Figure 2.1 shows the location of the selected cities, and Table 2.1 provides their physical characteristics. The elevation of the cities (above mean sea level, MSL) varies from 5 m (Kolkata, an eastern coastal city near the mouth of the river Ganges) to 385 m (Jaipur, a city bordering Aravalli ranges in the western part of the Gangetic plains). The urban fraction of the area surrounding the weather stations (Table 2.1) is calculated using the ESA-CCI land-cover map having a spatial resolution of 350 m (Hollmann et al., 2013).

The METAR weather observations from 1991 to 2020 are used. They constitute a period of the recent 30 years, which is the recommended period for defining climate by the World Meteorological Organization (WMO, 2017). However, many of the selected stations have insufficient records for 1991; hence effectively, only 29 years of data are used. For ease of interpretation, the results of fog timings are reported in local time, i.e., Indian Standard Time (IST, i.e., GMT + 5:30). The data analysis revealed that most of the fog events in the study area occur during the winter months. The winter season of a year denotes January- February of that year and November- December of the previous year. For example, the winter season of 2020 represents January-February months of 2020 and November-December months of 2019. Cities having at least 15 winter seasons with a minimum of 85% data availability at an hourly scale in every season are selected. The numbers of winter seasons meeting this eligibility criterion for different cities are shown in Table 2.1.

Sub-daily rainfall data are essential input for determining fog typology. Though METAR records contain rainfall data, they have many missing values. Hence, the rainfall data are taken from satellite-derived precipitation product Tropical Rainfall Measurement Mission Multisatellite Precipitation Analysis (TRMM-TMPA) (Adler et al., 2003; Huffman et al., 2007). With a 3-hour temporal resolution and a 0.25° (~ 25 km at the Equator) spatial resolution, this dataset is available from 1998 onwards. Google Earth Engine (Gorelick et al., 2017), a cloud-based platform, is used for retrieving rainfall data for each city. Though the satellite-derived rainfall data are not as accurate as *in situ* data; however, they have reasonable accuracy for India (Kneis et al., 2014; Shukla et al., 2019), which is deemed sufficient for fog classification. The 3-hourly rainfall is disaggregated into half-hourly rainfall, assuming uniform rainfall intensity over the observation period of 3 hours (Barton et al., 2020). Table A 2.1 in Appendix 2.1 summarises the datasets used in this chapter.

2.3 Methodology

This section describes the fog terminologies, strategies employed for filling missing data, algorithms for identifying and classifying fog events, and discusses the concept, procedure, and assumptions behind the analysis of fog data presented in this chapter.

2.3.1 Identification and removal of low visibility no-fog episodes

Though fog is defined in terms of visibility, sometimes, lowering of visibility may be caused not only by fog but also by other phenomena, including the presence of thick smoke or dust storms (Dey, 2004; Terry et al., 2018). Hence, non-fog low visibility episodes should be identified and removed from the data to study fog climatology. Dust and smoke increase the aerosol loading in the atmosphere, causing haze and thereby reducing visibility. Methods have been developed to distinguish fog and haze using aerosol and meteorological data (Ma et al., 2014; Zou et al., 2021). However, due to the lack of historical aerosol data, such methods are not applied in this study. Instead, methods that distinguish haze and fog by applying thresholds on visibility and relative humidity are used (Ding & Liu, 2014; Guo et al., 2020; Ram et al., 2012; Yang et al., 2021) and are described in the next sub-section.

2.3.2 Extraction of fog events

Like most other meteorological phenomena, fog also shows persistence. Typically, at the beginning of a fog event, the visibility starts decreasing (fog onset); it reaches a minimum value and then starts increasing (i.e., fog dissipation, burnout, dissolution). To extract fog events from periodic measurements of visibility, we have used the ‘M-of-N’ construct introduced by Tardif & Rasmussen (2007), where M represents the number of measurements with fog within N consecutive measurements. Following the Tardif & Rasmussen (2007) defined the presence of fog when observed visibility is less than 1.61 km (1 mile). However, to provide consistency with the WMO fog definition, an additional requirement of the presence of visibility of less than 1 km during a fog event was imposed. Figure 2.2 summarises the fog extraction by the M-of-N algorithm.

Symbols:

	: Half hourly observation of visibility (vsby)		
	: Fog observation : vsby < 1.6 km		
	: Peak fog observation : 0 < vsby < 1 km		
	: Fog event	: Onset of event	: Dissipation

Definition:

Fog event : M-of-N : 3 within 5 + atleast 1

Examples:

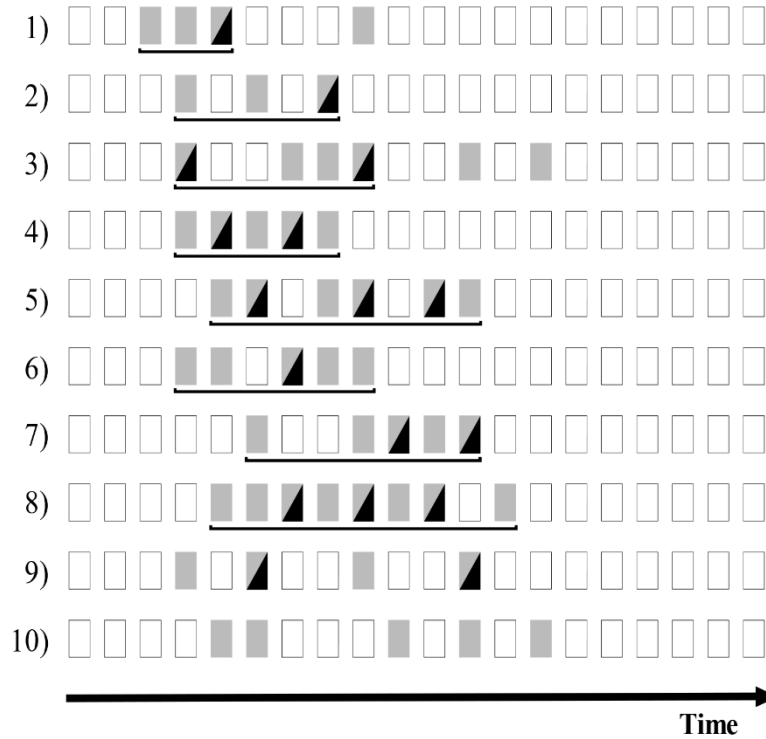


Figure 2.2. Illustration of fog event identification from hourly periodic observations by M-of-N method.

In the M-of-N algorithm, the choice of M and N depends on the target fog event duration. Thus, a sensitivity analysis of the M-of-N algorithm is carried out (Appendix A 2.2), based on which M and N are selected as 3 and 5, respectively. Since the visibility observations in our study were at half-hourly intervals, the choice corresponds to the minimum fog duration of 1.5 hours. The M-of-N algorithm is applied to visibility data rather than fog directly. However, the lowering of visibility may be caused due to other incidents, which should be

removed before calculating the fog statistics. Herein, non-fog low visibility events identified by the M-of-N algorithm are removed by imposing thresholds on wind speed and relative humidity. Figure 2.2. A threshold of 80% average relative humidity during an M-of-N event is set to distinguish a fog event from a low visibility event caused due to haze (Guo et al., 2020; Kumari et al., 2021). Additionally, a threshold on average wind speed (25 km/h) is applied to separate low visibility storm events from fog events.

2.3.3 Missing data imputation

The METAR data have many missing records. Since the M-of-N algorithm for fog event identification requires periodic observations with no missing values, data imputation is necessary. Also, the missing values may be unequally distributed over a day or a season, which can lead to incorrect inferences about fog characteristics.

For this chapter, the missing data are imputed by linear interpolation (Kim et al., 2021). Since most of the gaps in the visibility data were less than 3 hours ($> 97\%$), the maximum length of the interpolation windows is set as 3 hours. This short-time window for interpolation does not affect diurnal and seasonal periodicities present in most meteorological variables. A sensitivity analysis is carried out to study the effect of interpolation (in terms of the length of the interpolation window) on the root mean square error (RMSE) of the imputed visibility values (see Appendix A 2.1).

If the gaps in the visibility data are longer than 3 hours, the interpolation is not performed, and consequently, fog events are not identified during that period. However, since the number of such long gaps was very small ($< 3\%$), ignoring them would not have resulted in any significant bias in the reported results.

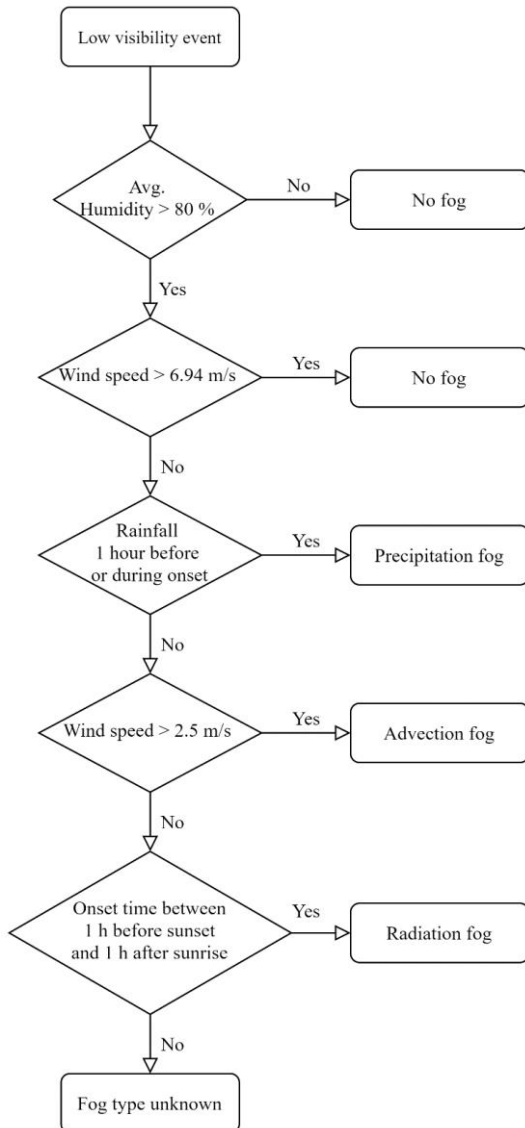


Figure 2.3. Algorithm for fog typology based on fog formation process.

2.3.4 Fog typology

Fog can be classified in many ways depending upon the objectives of the study. To understand fog climatology, we have used the following three classifications.

2.3.4.1 Based on fog formation

Among the various types of fog, radiation, advection (Pithani et al., 2019), and precipitation fog (as winter rainfall is observed during the Western Disturbances; Dimri et al., 2015) were deemed to be predominant over IGP and hence were considered in this study. The events that do not fall under any of the above three categories are labelled as unknown fog class.

The algorithm used for fog typology (Figure 2.3) is a modified version of the algorithm proposed by Tardif & Rasmussen, (2007). The algorithm is modified to remove low visibility non-fog events due to the presence of haze. In the original algorithm, morning evaporation fog and cloud-base lowering fog are classified. However, these two types of fog are not included in the study due to the non-availability of evaporation and cloud-base and evaporation data, respectively. Further fog typology is carried out from 1998 onwards because TRMM-TMPA data are available since 1998. Moreover, fog events are classified based on their onset time and visibility range, as discussed in Section 1.3. The sunrise and sunset timings are calculated using the ‘Suntime’ library of Python programming language (Krzysztof et al., 2019).

2.3.5 Analysis of fog events

2.3.5.1 Transition probabilities of fog events

The transition probability concept is used in Markov Chains (Weisstein, 2010) to study the transition of different states. Herein we analysed transition probabilities to study the evolution of sequences of different fog events classified based on visibility range. The events that happened in the same winter season are only considered while calculating the transition probabilities.

2.3.5.2 Duration of fog events

The hazardous impact of a fog event scales with its duration, and hence analysis of fog duration is crucial. In this study, the duration of fog events is analysed with the help of boxen-plots and violin-plots. Boxen-plots, also known as letter-value plots (Hofmann et al., 2017), are special kinds of box-plots designed to improve the representation of data distribution beyond quartiles of traditional box-plots. A brief description of boxen-plots and violin-plots is provided in Appendix 2.3.

2.4 Results of fog climatology and typology

The results of the seven cities are arranged in the ascending order of their latitudes, i.e., from the south (Kolkata) to the north (Amritsar), to visualise the latitude effect on fog characteristics.

However, in IGP, the elevation also generally increases with latitude (Figure 2.1), a trend also observed among the study sites (Tables 2.1), with the exception of Patna, which has a higher latitude than Gaya but a lower elevation. Thus, it is difficult to completely disentangle latitude and elevation effects.

2.4.1 Intra-seasonal distribution of fog events

Figure 2.4 shows the percentage of fog events that originated in all weeks of the winter months (November to February) for different cities. Averaged across cities, November has the lowest percentage of fog events (~16%), with Lucknow (23%) and Amritsar (22%) witnessing a relatively higher number of fog events in November compared to other cities. The maximum number of fog events occurs in the first week of January, followed by the last week of December in most cities. Overall, January and December constitute 37% and 29% of all fog events across the cities, respectively. In February, the number of fog events reduces to ~18%, except in Delhi, that witnesses an extended fog season with about 31% of all fog events occurring in February. Jaipur has the shortest fog season, where the majority (20%) of the events are observed in the first week of January.

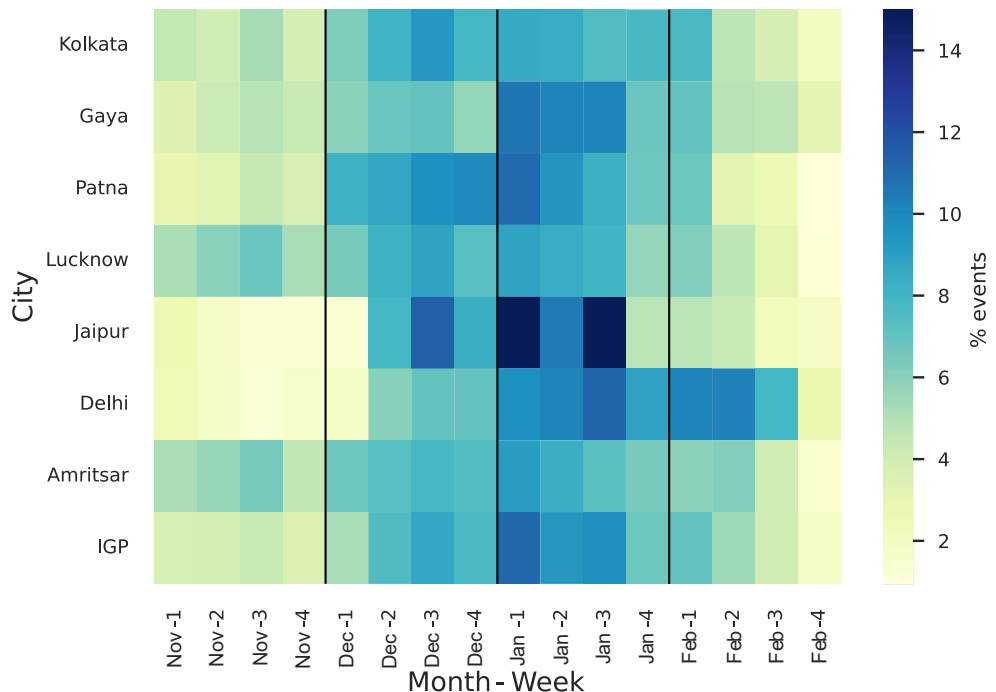


Figure 2.4. Heatmap showing the percentage of fog events during different weeks of a winter season. Month and week are shown on X-axis in the format month-week. The percentage is calculated city-wise, i.e., each row sums up to 100%. Black vertical lines indicate the end of months. (Jaipur shows the maximum of 20% events in the first week of January, this value is curtailed to 14% for better visualisation of the rest of the values.)

2.4.2 Diurnal distribution of fog events

The onset and dissipation time of fog events may not be uniformly distributed over a day. Hence knowing the typical onset time helps to predict fog events. The percentage frequencies of the onset, dissipation, and presence of fog during a diurnal cycle are shown as heatmaps in Figure 2.5. In these plots, the percentages are calculated city-wise, i.e., each row sums up to 100%. Since the data availability may not be the same for all hours of the day, the fog frequencies are normalised with respect to the number of observations to reduce the effect of unequal data availability. Additionally, in some cases the visibility observation may be missing at the onset (16% of total fog events) or dissipation (8% of total fog events) of an event. Such events are not considered while calculating the percentages of diurnal distribution.

The typical onset time of a fog event is between 5 pm and 8 am (Figure 2.5 a). Averaged over all cities, it constitutes 61% of all fog events, with 24% originating between 8 pm and 11 pm, 20% between 11 pm and 2 am, and 17% between 2 am and 5 am. Further, about 17% of fog events originate during dawn (5 to 8 am) hours as well as during dusk (5 to 8 pm)

hours. A geographical trend is apparent in the onset timings, as the onsets in western cities (Amritsar and Jaipur) are delayed by up to 2 hours compared to eastern cities (Kolkata, Gaya, and Patna).

The distribution of fog dissipation (Figure 2.5 b) is not as widespread as the distribution of onset timings (Figure 2.5 a). On average, about 70% of all fog events across all the cities dissipate between 9 am to 1 pm, with a maximum of 23% between 11 am and 12 noon. Further, around 6% of events dissipate during 8 and 9 am, as well as during 1 and 2 pm. Kolkata shows exceptional behaviour, with about 14% of fog events dissipating before 8 am compared to only 5% in other cities.

Figure 2.5 (c) shows the (percentage) probability of the presence of fog during each hour of the day in the winter season. There exists a non-zero probability of fog presence throughout the day with a maximum probability of 7% (averaged across all cities) between 7 and 8 am. The probability decreases as the day progresses and reaches a minimum value of 2% between 5 and 6 pm. It then increases during the night before reaching the maximum value. Delhi shows a more uniform distribution of fog (coefficient of variation, i.e., CV of 0.24) compared to other cities (CV of 0.46).

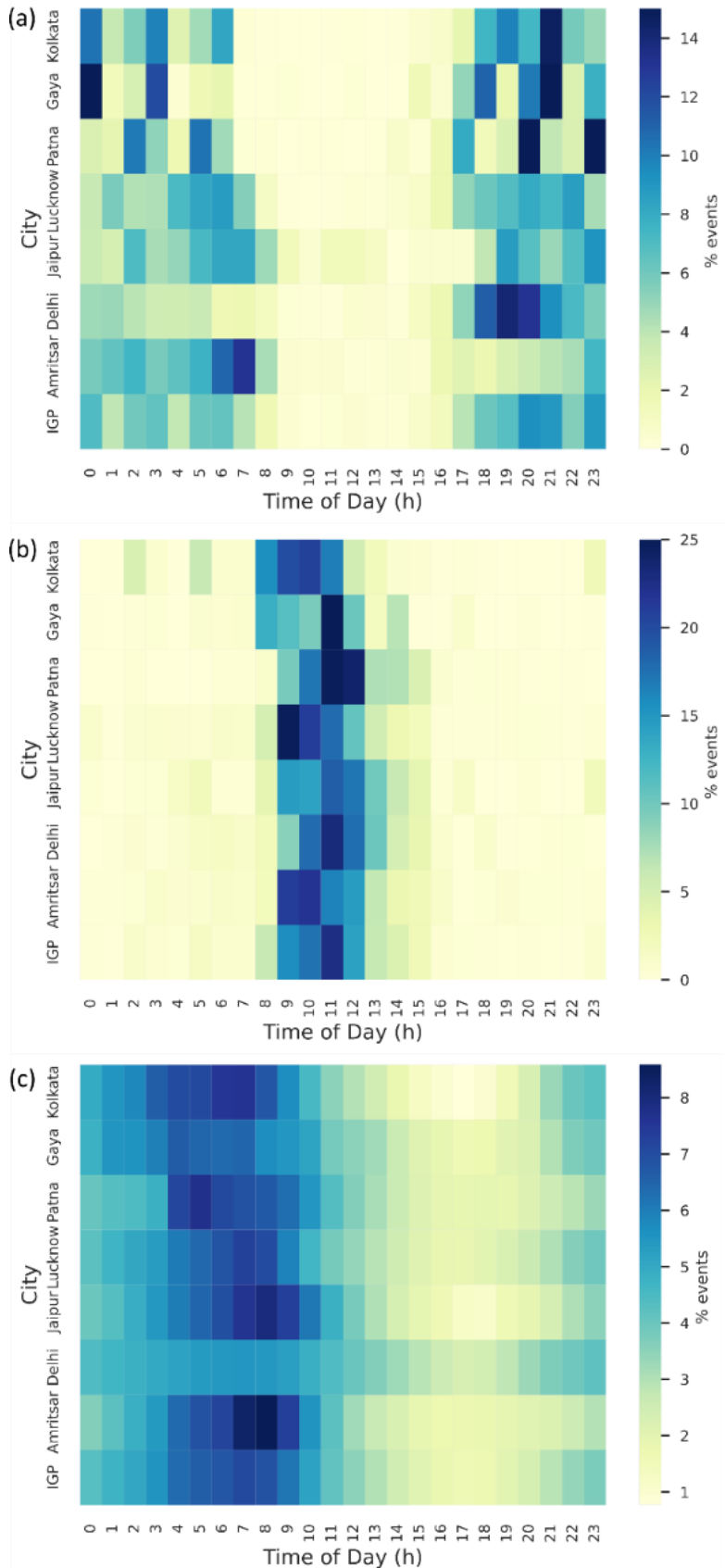


Figure 2.5. Heatmaps showing (a) fog onset, (b) dissipation timings of fog events, (c) probability (percentage) of the presence of fog during each hour of a day. The percentage is calculated city-wise, i.e., each row sums up to 100%. (In Figure 2.5 (a), from 8 pm to midnight, Gaya and Patna have few values up to 19 and 23%, respectively. Such values are curtailed to 14% for better visualisation of the rest of the values.)

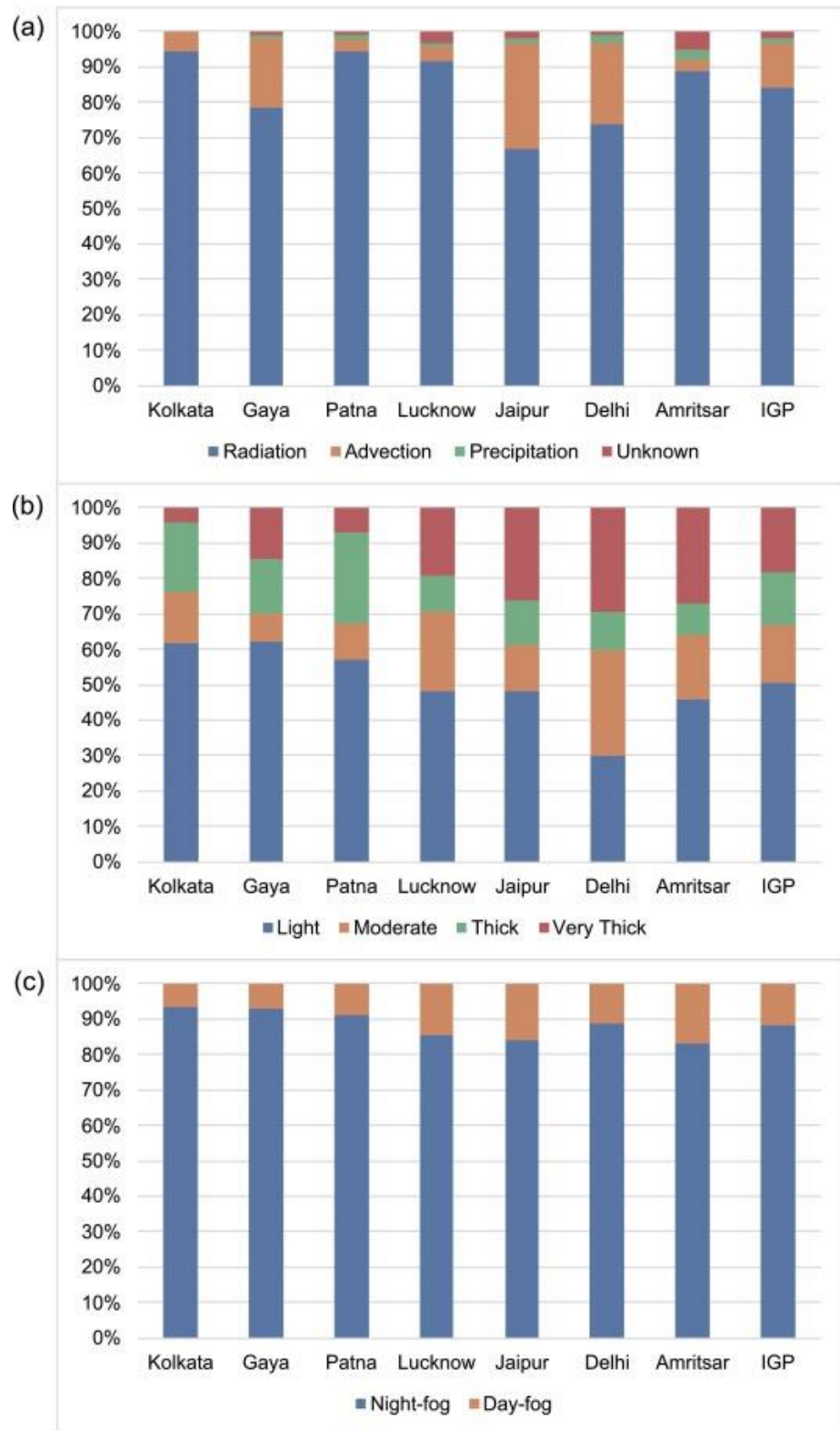


Figure 2.6. (a) Formation-based fog classification, (b) Visibility-based fog classification, (c) Onset time-based fog classification.

2.4.3 Fog typology

2.4.3.1 Based on fog formation

Figure 2.6 (a) shows that the predominant fog type is radiation fog constituting 84% of all fog events averaged across all the cities. On the other hand, precipitation fog is rare (<3%). A significant percentage of fog events (>20%) is classified as advection fog for Jaipur and Delhi, with an average contribution of 13% over all the cities. Kolkata, Patna, and Lucknow mostly exhibit radiation fog events (>90%). The percentage of fog events that cannot be classified (unknown fog class) is <2%, with a maximum value of <6% for Amritsar.

2.4.3.2 Based on visibility range

Figure 2.6 (b) shows that most fog events are categorised as light fog events (about 50% of all fog events across all cities). Kolkata (19%), Gaya (15%), and Patna (26%) show an above-average percentage of thick fog, whereas the average over all the cities is 14%. Jaipur, Delhi, and Amritsar show a higher percentage (>25%) of very-thick fog events, which is much more than the average of all cities together (18%). On the other hand, Kolkata and Patna have very few thick fog events (<10%). About 40% of events in Delhi are either thick or very thick fog, which is the highest among the cities, whereas the percentage is lowest for Kolkata (24%). Overall, the intensity of fog events appears to increase with the increase in the latitude of the station.

Figure 2.6 (b) shows that the percentage of very thick fog events is comparable to thick as well as moderate events. The visibility range of very thick fog events is very narrow (50 m) compared to thick (150 m) and moderate (300 m) fog events. This suggests that a significant probability mass of visibility is concentrated between 0 to 50 m.

The predominant fog type based on fog formation is radiation fog. Hence the visibility-based classification reflects the characteristics of radiation fog. Since Jaipur and Delhi have a relatively higher percentage of advection fog events, they were selected to study the visibility-

based classification of advection fog. The analysis showed no significant differences in the visibility-based classification of the radiation and advection fog events.

2.4.3.3 Based on onset time

The percentages of day-fog and night-fog for different cities (Figure 2.6 c) show that the night-fog is predominant. Hence, most fog events (88% averaged over all cities) start after sunset but before sunrise. Kolkata and Gaya show the highest percentage of night-fog (93%), whereas Jaipur shows the highest percentage of day-fog (84%).

2.4.4 Transition probabilities for fog events

The transition probabilities of fog events classified based on visibility range are shown using heatmaps in Figure 2.7. The results suggest that light fog events are likely to be followed by light fog. Further, in most cities, moderate and thick fog events are also followed by light fog events. Moreover, very thick fog events are likely to be followed by very thick fog events in all the cities except Kolkata and Patna. In other words, light fog events and very thick fog events are likely to get repeated.

The transition probabilities shown in Figure 2.7 are estimated by considering fog events in the same winter season, irrespective of the duration between the events. We also estimated transition probabilities by restricting the duration between two subsequent events (end of current and start of next event) to 48 hours. The maximum absolute difference between the two estimates for different cities varies from 4% to 8%. Hence, duration between the events does not significantly affect the transition probabilities.

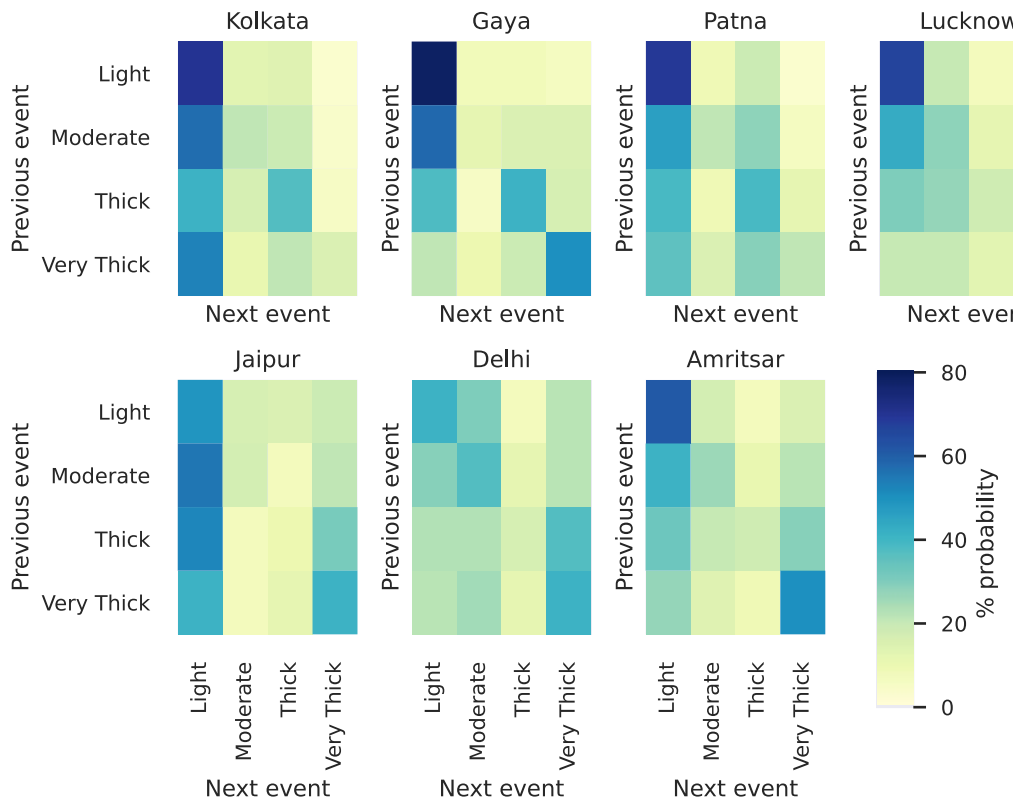


Figure 2.7. Transition probabilities for the visibility-based fog types. The previous and next events correspond to the same winter season, irrespective of the duration between the two events.

2.4.5 Duration of fog events

2.4.5.1 Based on visibility

The distribution of duration of fog events for different cities and different fog types (based on visibility range) exhibits enormous variation (Figure 2.8). The average duration of all cities considering all the fog types together (Combine) is 11.9 hours, whereas the median fog duration is 9.5 hours suggesting that the distribution of fog-event durations is positively skewed. City-wise average duration of combined fog is lowest for Jaipur (9 hours) and highest for Delhi (14.9 hours). The duration of the longest fog event observed in Delhi is 14 days (16th to 30th December 2019). Kolkata and Jaipur have a relatively shorter duration of fog events. Among all the fog types, thicker fog events are usually longer, i.e., there is a tendency for thicker fog to persist for a longer time. The average fog hours in a foggy day (defined as a day with at least

one fog event) is less than 12 hours, with fog more likely to be present during morning hours (Figure 2.5 c). Thus, despite a day being foggy, around half of the day is without fog.

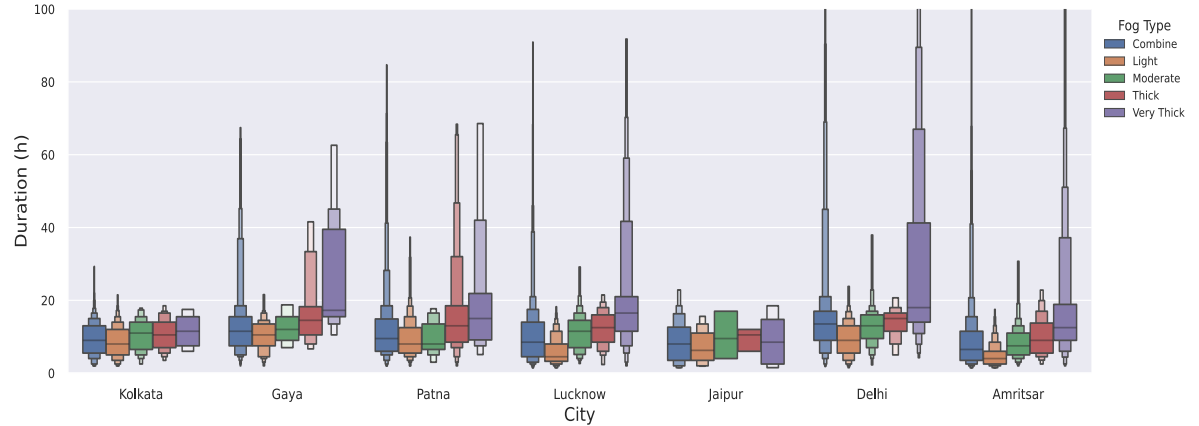


Figure 2.8. Duration of fog events for visibility-based fog types and a “combine” category that includes all fog types (Very few fog events (<0.4%) longer than 100 hours are identified, but they are not shown in the figure).

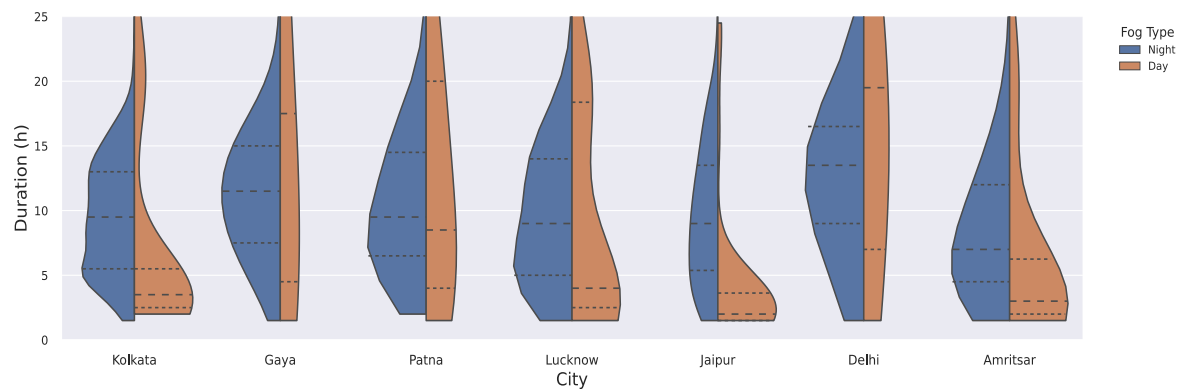


Figure 2.9. Violin-plots showing the duration of fog events for different fog types based on their onset time. Day-fog events have onset time between sunrise and sunset; otherwise, the fog event is considered Night-fog.

2.4.5.2 Based on onset time

Figure 2.9 shows that the average fog durations calculated over all the cities for the day-fog and night-fog events are nearly the same (12.3 and 11.9 hours, respectively). In comparison, the median duration of day-fog events (4 hours) is significantly less than the median duration of night-fog events (9.5 hours). This suggests that most of the day-fog events are short-lived, with a few very long-duration day-fog events. For some cities (Kolkata, Lucknow, Jaipur, and Amritsar), the duration of day-fog events tends to be bimodal. This bimodal nature of durations

indicates that the fog events started after sunrise either dissipate in the same morning (showing a shorter duration) or continue until the next morning (showing a longer duration).

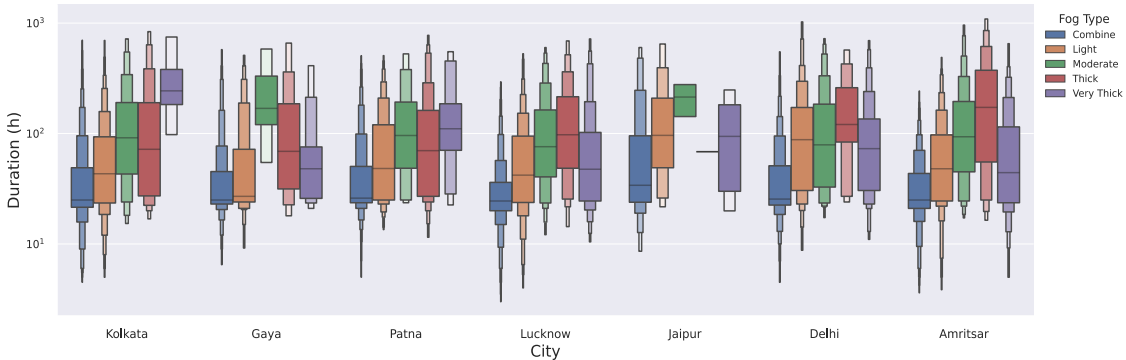


Figure 2.10. Duration between the onset of two fog events (inter-event duration) of different fog types and a “combine” category that includes all the four fog types.

2.4.6 Inter-event duration

Inter-event duration is defined as the duration between the start of two fog events. Since the inter-event durations show large variations across cities, they are shown using a logarithmic scale in Figure 2.10. The average inter-event duration across all cities is 49 hours, whereas the median duration is 25 hours. Fog spells having many fog events with small inter-event durations, followed by a no-fog spell, can be the cause of a significant difference between the mean and median.

Amritsar and Lucknow have the least average inter-event duration (37 hours), while Jaipur has the longest (130 hours, i.e., ~5 days). Kolkata has a relatively shorter inter-event duration for combined fog events (56 hours) than Jaipur (115 hours). However, Kolkata has the highest median value (243 hours, i.e., ~10 days) for very thick fog events, whereas Jaipur has the highest median value (96 hours, i.e., 4 days) for light fog events. A comparison of different fog types shows that light and very thick fog events have lesser inter-event duration, i.e., a light or a very thick fog event is quickly followed by another light or very thick fog event. The comparison also suggests that these two fog types are frequent in the IGP; this conclusion is also inferred from the transition probabilities (Figure 2.7).

2.4.7 Inter-seasonal distribution of fog events

Figure 2.11 shows inter-seasonal (i.e., inter-annual) variation of different fog event characteristics, viz., the number of fog events, the average duration of fog events, and total fog hours for different cities. Seasonal fog hour is the product of the number of fog events and their average duration in a winter season and is same as the sum of fog hours in that season. The mean series (thick black line in Figure 2.11) is the average across the cities for the corresponding season. Linear trend in the mean series is investigated by regressing it against time (dotted line in Figure 2.11), and corresponding regression equations and coefficients of determination (R^2) are shown in the figure.

The mean number of fog events shows a considerable inter-annual variation (Figure 2.11 a). A few cities always have more fog events than the mean (viz., Amritsar, Lucknow), while some other cities (viz., Jaipur and Delhi) always have fewer fog events than the mean. Jaipur and Kolkata show higher variations as compared to other cities. The CVs of these two cities are 0.85 and 1.05, respectively, compared to 0.37 of the mean series. Lucknow and Amritsar show the least variability in the number of fog events (CVs near 0.20).

The mean duration of fog events (Figure 2.11 b) exhibits less inter-annual variability (CV of 0.23) compared to the mean number of fog events (CV of 0.37). For most of the years, mean durations of fog events in Patna and Delhi are above the mean of all cities, while Jaipur always remains below the mean of all cities. All cities have CVs in the range of 0.3 to 0.4, which is more than the CV of the mean series (0.23).

The mean series of total fog hours (with CV of 0.41) in a season (Figure 2.11 c) shows a variation pattern similar to the mean number of fog events (Figure 2.11 a). Delhi and Lucknow remain above the mean, while Jaipur remains below the mean. The rest of the cities remain near the mean without any distinct pattern. The mean of total fog hours is significantly smaller (using Student's t-test at 95% confidence interval) for some years (1995, 2008, 2019) and significantly higher for some other years (1998, 2014, 2020). Most cities follow the

behaviour of the mean line. Linear regression of the means series shows a significant (at 95% confidence interval) increasing trend in the average duration of fog events (Figure 2.11 b) and total fog hours in a season (Figure 2.11 c). In contrast, no significant trend is present in the number of fog events in a season (Figure 2.11 a).

The seasonal fog hours (Figure 2.11 c) and correlation values (Table A2.4) show that almost all the cities are positively intercorrelated in terms of seasonal fog hours. The exception is Kolkata which is either negatively correlated or not significantly correlated with other cities. Other exceptions are pairs of Delhi-Patna and Gaya-Patna, which show a positive but non-significant correlation. The correlation coefficient of the mean series of the number of events with seasonal fog hours is 0.83, which is higher than the correlation coefficient between the mean series of average duration of fog events and seasonal fog hours (0.69), and the number of fog events and the average duration of fog events (0.23). Thus, the number of fog events and seasonal fog hours are more correlated.

The number of fog events and seasonal fog hours exhibit relatively higher variation in the inter-annual time-series (CV of 0.37 and 0.41, respectively) compared to the average duration of fog events (CV of 0.23), suggesting that non-local phenomena may have a greater influence on the number of fog events and the seasonal fog hours than the average duration of fog events. Further, though the average duration of fog events shows smaller inter-annual variability (CV of 0.23), it varies largely among the different cities (CV of 0.36). Therefore, local factors have a greater effect on the average duration of fog events. In this sense, fog characteristics at a site depend on local topographical factors (e.g., land cover, urban fraction, presence of moisture source nearby) that may be driving the inter-city variability, as well as on non-local (global) climate factors that may be driving the inter-annual variability.

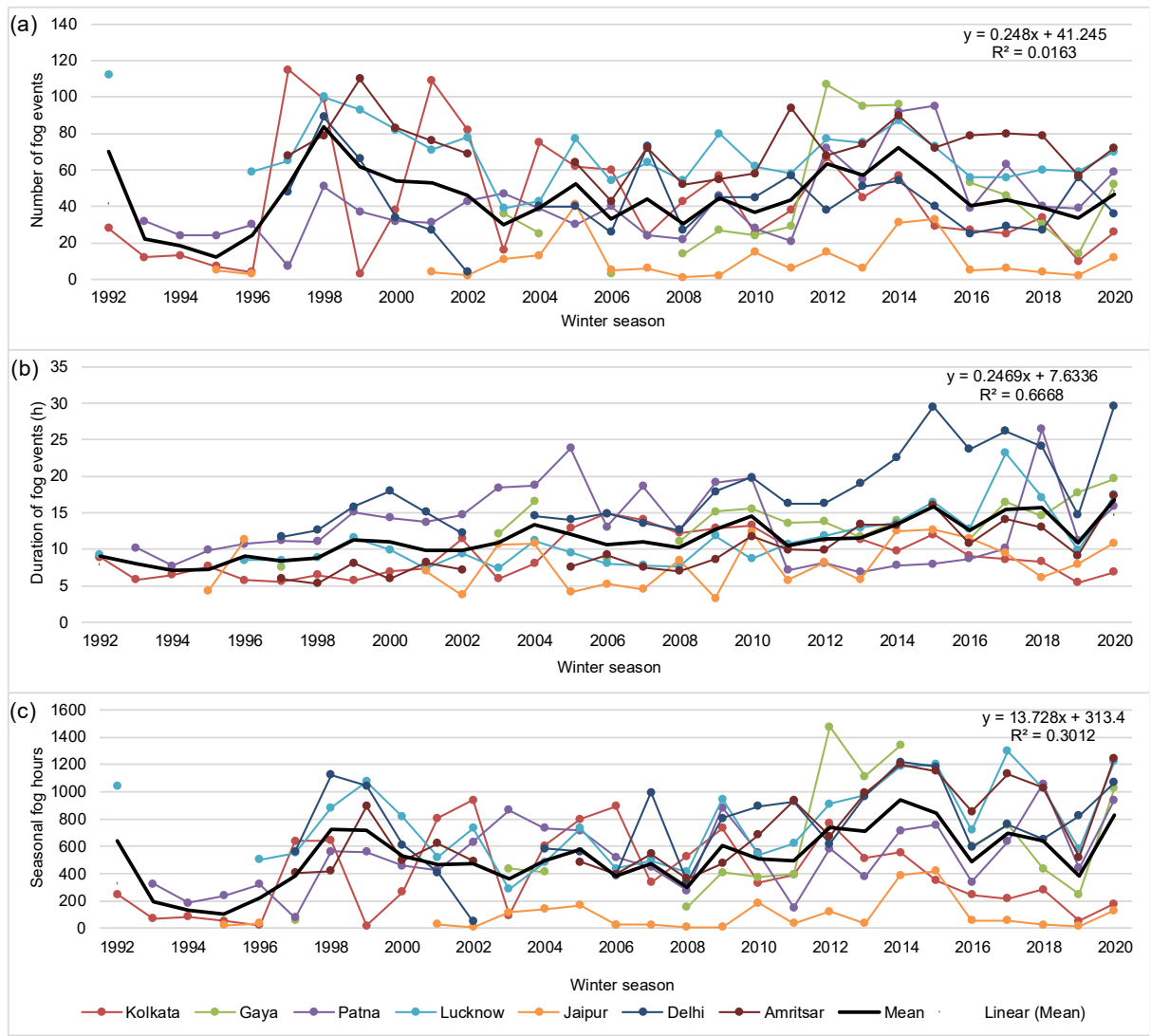


Figure 2.11. Time-series of characteristics of fog events – (a) number of fog events, (b) seasonal average of the duration of fog events, and (c) seasonal total fog hours - for different cities and different winter seasons. The mean value for all the cities (thick black line) and the fitted linear regression trendline (dotted line) is also shown.

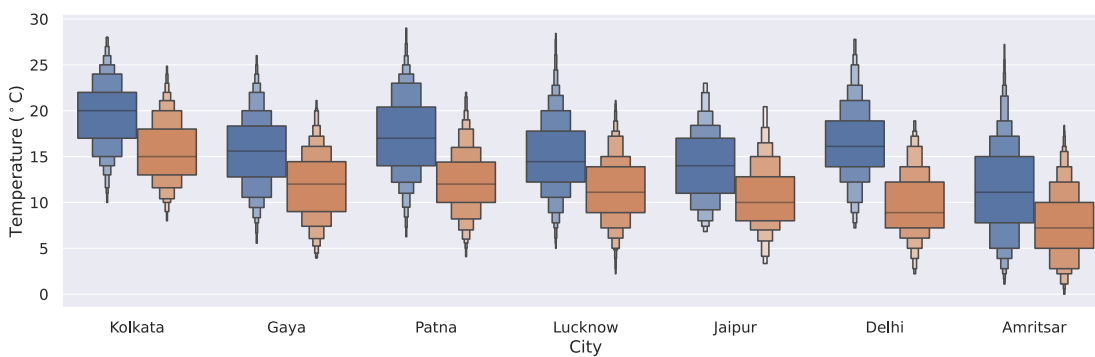


Figure 2.12. Maximum and minimum temperature distribution for different cities.

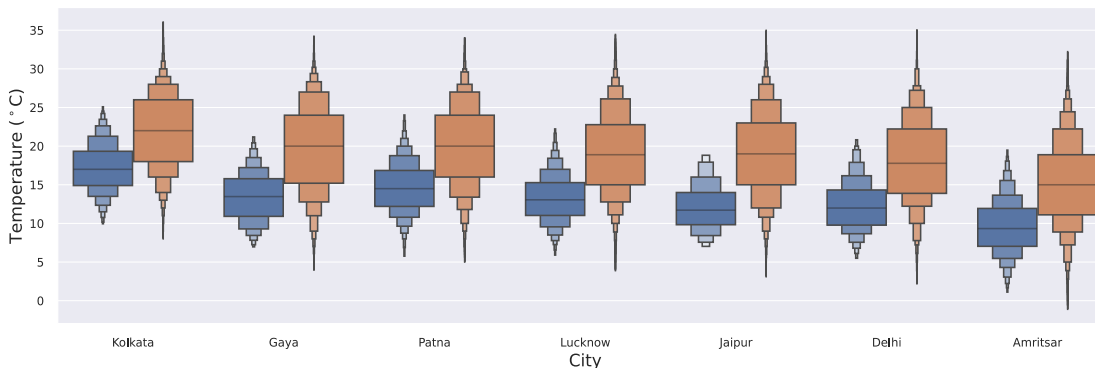


Figure 2.13. Boxen-plots showing temperature distributions during fog and no-fog conditions.

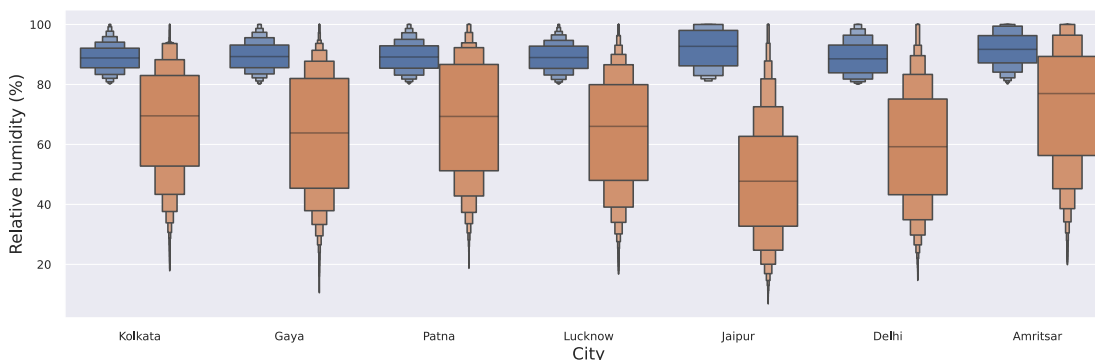


Figure 2.14. Boxen-plots showing relative humidity distributions fog and no-fog conditions.

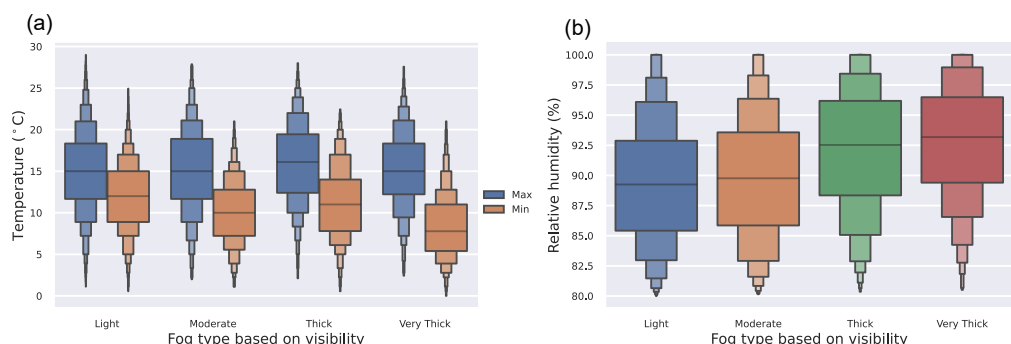


Figure 2.15. (a) Temperature and (b) relative humidity distribution for visibility-based fog types.

2.4.8 Fog event climatology

To study the prevailing conditions of the meteorological variables (viz. temperature, relative humidity, wind speed and direction) during fog events, their distributions are plotted (Figures 2.12 to 2.16). Figure 2.12 shows that during fog events, the median of minimum temperatures is between 7°C to 15°C, whereas the median of maximum temperatures is between 13°C to 20°C. In both cases, temperature decreases with latitude. The only exceptions are Patna and Gaya. Patna is north of Gaya, but its temperature during fog events is slightly higher than Gaya. The median temperature difference (maximum minus minimum temperature observed during a fog event) for all the cities is around 5°C, except Delhi and Patna, for which the median temperature differences is 7.5°C and 6°C, respectively (Figure 2.12). Moreover, the median temperature during the no-fog scenario is slightly more (~5 °C) than during the fog events (Figure 2.13).

Relative humidity during fog events shows little variation among cities. The median relative humidity during fog events is above 88% in all cities, with most of the values being greater than 80%. The median relative humidity during no-fog events is nearly 30% less than during fog events for all the cities except Jaipur, where the difference is around 50% (Figure 2.14).

The prevailing conditions for different visibility-based fog classes are studied by comparing their distributions of temperature and relative humidity. The difference between the minimum and maximum temperature observed during fog events is higher during very thick fog events compared to light fog events. This indicates more temperature variability during very thick fog events (Figure 2.15 a). Also, generally, the minimum temperature during a fog event decreases from light to very thick fog (Figure 2.15 a) while relative humidity increases (Figure 2.15 b).

Typically, the surface winds in IGP are Westerly or North-Westerly during winter. The same is observed for most cities (Figure 2.16) except Kolkata and Jaipur, where the prevailing wind direction during winter is north and east, respectively. Figure 2.16 compares the distributions of wind direction during fog and no-fog conditions to study the effect of wind on fog. The land cover maps around the airport weather stations are shown in Figure 2.17. In the case of Gaya, Westerly winds are observed during no-fog, whereas during fog events, the winds are observed from the South-East. Patna and Lucknow show typically Westerly winds for both fog and no-fog conditions. For Lucknow, during ~15% of the fog events, the winds come from the east, the direction with irrigated croplands. Unlike other cities, the prevailing winds in Jaipur are Easterly, and the same direction is also observed during advection fog events. Moreover, 70% of fog events show the Easterly and the North-Easterly winds. The fog during the Easterly winds can be attributed to the forest area present North-East of the city. Delhi shows Westerly winds in winter, along with some observations of Easterly winds. During advection fog events in Delhi, the winds are mostly Westerly. Amritsar shows Westerly and North-Westerly winds during fog and no-fog conditions, with only around 15% of fog events showing the presence of Easterly winds.

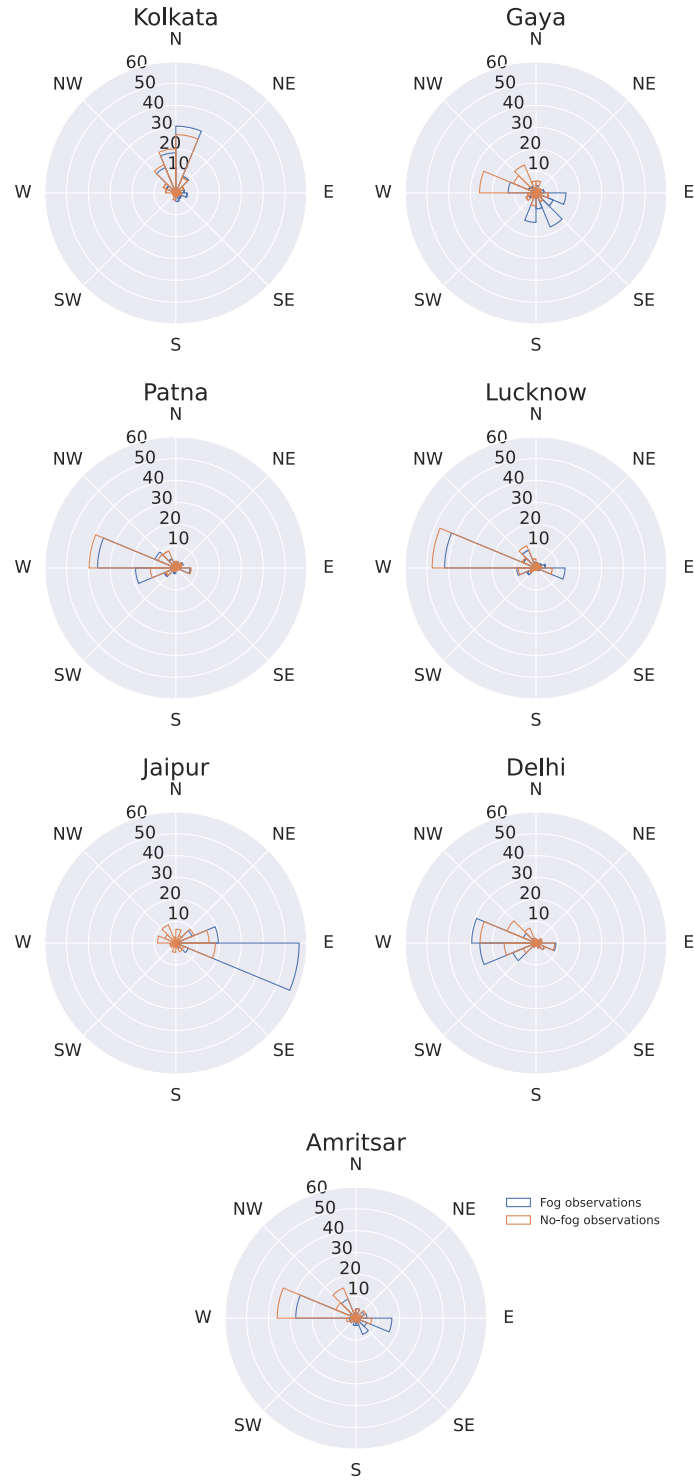


Figure 2.16. Distribution of wind direction for different cities during fog and no-fog scenario. The values are shown in percentage. They are calculated city-wise and category-wise, i.e., each subplot sums up to 100% for fog observations and winter observations separately

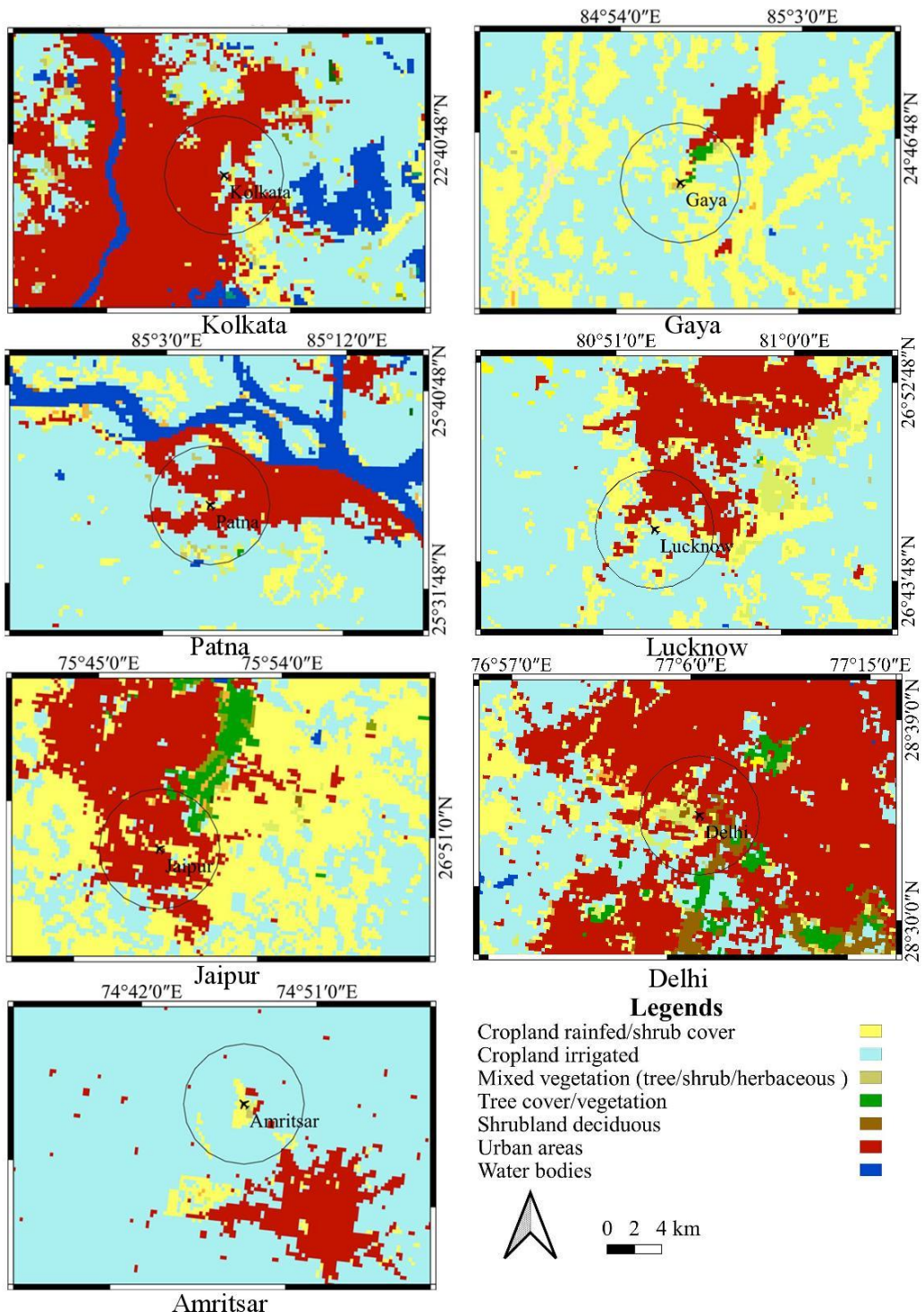


Figure 2.17. Land cover around the weather stations of seven cities used in the study (All the circles are of 5 km radius)

2.5 Discussion

2.5.1 Inferences from the analysis

The cities included in the study have similar topographical characteristics (flat terrain and away from seacoast), except Jaipur (hills nearby) and Kolkata (presence of seacoast). The results show that both Kolkata and Jaipur have relatively shorter durations of fog events (Figure 2.8). Unlike any other city, Kolkata witnesses an earlier fog dissipation (during 8 to 11 am) and has a relatively smaller number of very thick fog events. Amritsar and Gaya are geographically located far from each other, but both cities show longer durations of fog events. Moreover, Gaya is correlated to Amritsar (along with Lucknow) in all three fog event characteristics, viz., the number of fog events, the average duration of fog events, and the seasonal fog hours (Table A 2.4). Both, Gaya and Amritsar are surrounded by irrigated croplands (Figure 2.17), providing necessary moisture for fog formation. Thus, the results suggest that local factors (e.g., land cover and proximity to moisture source) may affect the duration of fog events. Except for minor variations, the rest of the cities are broadly similar in terms of fog characteristics.

Table 2.2. A summary of fog event comparison in IGP with other regions of the world. The symbol “*” refers to the studies having different start years and “†” refers to the study having two separate study periods. The onset and dissipation timings are mentioned in local time.

Study area (# stations)	Authors (year of publication)	Years of study	Frequency of analysis	Foggy months	Major fog type (% occurrence)	Avg. duration (or events) of events /year	Foggy days Typical Onset- Dissipation
IGP, India (7)	Present study	1991-2020	30 min	Nov-Feb	Radiation fog (84%)	12 h	10-72 events 9 am-1 pm
Perth, Australia (1)	Roux et al., (2021)	2002-2019	10 min	May-Jul	Radiation fog (61%)	2 h	-
Czech Republic (12)	Hůnová et al., (2020)	1961-2018	24 h	June-Sept	Radiation fog in lowland areas, low status in hills	-	-
UAE (8)	Mohan et al., (2020)	(1944,2010) - 2018*	1 h	Nov-Feb	Radiation fog (70%)	<6 h, mode 3h)	27-50 events am- 2 pm
Netherlands (29)	Izett et al. (2019)	1955-2000, 2012-2018†	10 min	Sept-Feb	Radiation fog (50%)	<3 h	~120 days Onset around 1 am
Plains of North Serbia (14)	Veljović and Vujović (2019)	(1973,1989) - 2005*	3 h	June-Sept	Radiation fog (65%)	3-7 h	32-69 days
Hungary (8)	Cséplő et al., (2019)	1956-2017	3 h	Nov-Feb	-	3-9 h	40 events Onset: 7-10 am
Terai in Nepal (4)	Shrestha et al. (2018)	1980-2015	4	Nov-Feb	-	-	22-55 days -
Japan (60)	Akimoto and Kusaka (2015)	2004-2008	1 h	All months	Radiation (50%), precipitation (37%)	8 h <60 days	Dissipation: 8- 11 am
South Korea (24)	Belorid et al., (2015)	1989-2013	3 h	2 seasons with peaks in Jul, Oct	Radiation (38%), precipitation fog (21%).	-	<50 events -
New York (17)	Tardif and Rasmussen (2007)	1977-1996	1 h	All months	Radiation in inland, advection fog in coastal areas	<8 h6 7-32 events	Onset: 7 pm- 7am onset, Dissipation: 7am-11 am

2.5.2 Comparison of fog in IGP with other parts of the world

The characteristics of the fog events in IGP are compared with other regions of the world in Table 2.2. The regions are compared in terms of the occurrence of fog in different months, duration, frequency, and type of fog. Though the definition of fog event and observation period of these studies are different, the comparison provides a synoptic understanding of fog in

different regions. The number of fog events in IGP varies from 10 (in Jaipur) to 72 (in Amritsar), with an average of 46 events per season, which is not significantly different from values reported for other regions of the world (Table 2.2). Radiation fog is prominent in all the regions, including UAE (contributing to 70% during DJF), Perth (61%), and north Serbia (65%); however, it is highest in the IGP (84%). Also, unlike most other regions of the world that witness fog throughout the year, fog in IGP is confined to the winter season. Further, the mean duration of a fog event in IGP (about 12 hours) is longer than that reported for other regions. In Serbia, 90% of fog events have a duration in the range of 3 to 7 hours. New York exhibits distinction in fog duration based on fog formation type - as a majority (75%) of the radiation fog events have a duration of less than 8 hours, while most of the precipitation and advection fog events last more than 8 hours. In UAE, 75% of the events have a duration of up to 6 hours, with a mode of nearly 3 hours. IGP has relatively high aerosol loading during winter (Babu et al., 2013). The higher aerosol loading leads to a higher concentration of small fog droplets, which have a longer residence time in the atmosphere (Quan et al., 2011). This may be the reason for the longer duration of fog events in IGP; nevertheless, further investigation is needed to ascertain this hypothesis.

2.6 Chapter summary

A fog climatology and typology study is carried out to characterise fog events in the IGP. METAR observations from seven cities with long-term records are first imputed and then used for fog characterisation. The conclusions of the study are -

- 1) Fog in the IGP occurs from November to February, with January witnessing the highest proportion of fog events.
- 2) Most fog events (61%) have an onset time between 5 pm to 8 am, and dissipation (70%) between 9 am to 1 pm. The western cities of IGP have delayed onset of fog as compared to the eastern cities.
- 3) The mean value of fog event duration is 11.9 hours, with very thick fog events having a relatively longer duration (22.8 hours).

- 4) Around 84% of all fog events in the IGP are due to radiation fog.
- 5) Half of the events are categorised as light fog events, i.e., the minimum visibility attained is between 500 m to 1000 m.

The results of this chapter indicate that local factors (viz., terrain, land cover, proximity to sources of moisture) may have a larger influence on the duration of fog events (higher inter-city but lower inter-annual variability). In contrast, the number of fog events and total fog hours in a season exhibit more inter-annual variability and are related to large-scale climate phenomena. Moreover, a comparison of fog events with other fog-prone regions of the world shows that IGP experiences a relatively higher percentage of radiation fog, which can be attributed to its geography (flat topography with little coastal influence). Further, fog events in IGP have relatively longer duration, which may be due to the higher concentration of aerosol in IGP during the winter months. However, further research is required to make these findings definitive.

This chapter is a modified version of a published article cited below:

Deshpande, P., Meena, D., Tripathi, S., Bhattacharya, A., & Verma, M. K. (2023). Event-based fog climatology and typology for cities in Indo-Gangetic plains. *Urban Climate*, 51, 101642.
<https://doi.org/10.1016/j.uclim.2023.101642>

3 SATELLITE FOG DETECTION

3.1 Introduction

Indian Space Research Organization's operational INSAT-3D Fog product provides near real-time satellite-based fog maps over India. We compared the output of INSAT-3D Fog model with *in situ* visibility observations over IGP. The results reveal limitations of the model and its poor performance (Appendix A3.1). This becomes the primary motivation behind the development of a satellite-based spatial fog detection model. This chapter reviews the existing fog detection methods and emphasise the need for uncertainty-aware models. A Bayesian neural network model is proposed for probabilistic fog detection. The mathematical formulation of the model and its training, testing and comparison with INSAT-3D Fog product are presented.

The satellite fog detection methods can be broadly divided into 2 categories, viz., dual-channel thresholding methods and data-driven methods. The dual-channel methods are the conventional physics-based methods. They usually involve the following three steps – dual channel Brightness Temperature Difference (BTD) calculation, histogram thresholding of BTD, and spatial and temporal tests (filtering) for the removal of pixels corresponding to snow and clouds (Chaurasia & Jenamani, 2017; Han et al., 2020; Ma et al., 2022). Instead of data from a single satellite, some studies have used a combination of satellites for fog detection (Jindal et al., 2023; Pauli et al., 2020; Yoo et al., 2018). Some other studies have applied probabilistic thresholds, instead of deterministic thresholds, to BTD histograms, resulting in probabilistic fog detection (Han et al., 2020; Mahdavi et al., 2021; Yang et al., 2019). Since the physical phenomena behind the formation and dissipation of fog are not well understood yet, these conventional physics-based methods have received limited success in detecting fog (Huang et al., 2022). The data-driven methods attempt to learn patterns in different bands of satellite imagery to detect fog. Most of these methods use artificial neural networks (ANNs; Guo et al., 2021; Huang et al., 2022; Tang et al., 2022; Yi et al., 2023), but other machine learning methods like gradient boosting (Jahani et al., 2023), logistic regression and Gaussian Mixture Model have been used (Shin & Kim, 2018).

A review of the literature on satellite fog detection by data-driven methods reveals that most of the studies have been carried out for the sea fog, while the land fog, which is patchier than the sea fog, has received much less attention (Gultepe et al., 2007). The results of fog detection are used for many critical applications (e.g., flight planning), where uncertainty estimates are required for making informed decisions (Vié et al., 2022). However, most data-driven fog detection methods reported in the literature do not provide uncertainty estimates.

In the context of satellite fog detection, uncertainty refers to the range of probability for the presence of fog at a given time based on satellite data. The uncertainty can be classified as aleatoric or epistemic uncertainty (Hüllermeier & Waegeman, 2021). Aleatoric uncertainty is an irreducible error that cannot be reduced by supplying additional data (Kendall & Gal, 2017). The inherent randomness of data causes this uncertainty due to unknown or uncontrolled reasons, e.g., local variability, limited resolution of satellite data, random errors in measurement of physical quantities and sensor noise. The epistemic uncertainty arises due to the lack of knowledge of model parameters. It corresponds to our limited understanding of the real-world scenario in terms of model parameters and can be reduced with more data, e.g., if extreme fog events in the historical data are rare, their forecasts will have large epistemic uncertainty.

The relevance of uncertainty estimation in hydrological modelling is well-established (Beven, 2012). Studies have also established the importance of resolving uncertainty into aleatoric and epistemic components (Gong et al., 2013); however, only a few studies have done so (Behrouz & Alimohammadi, 2018; Mishra et al., 2019). This may be due to either philosophical disagreement in defining aleatoric and epistemic components of uncertainty in hydrological modelling (Gupta & Govindaraju, 2023; Nearing et al., 2016) or a lack of convenient tools for estimating them (Pappenberger & Beven, 2006). Lately, there has been an increased interest in distinguishing the two components of uncertainty in the context of probabilistic machine learning models (Abdar et al., 2021; Hüllermeier & Waegeman, 2021).

Among probabilistic machine learning models, Bayesian neural networks (BNNs), a Bayesian alternative to deep neural networks, have received significant attention because they provide an elegant mathematical construct to distinguish the two components of uncertainty. They have found applications in hydrological as well. For example, Li et al. (2022) compare the Bayesian model averaging with the Bayesian long short-term memory (BLSTM) model, a variant of BNN, for streamflow prediction at 4 catchments in China. The results show that BLSTM that uses variational inference (details provided in Section 3.3.1) improves streamflow predictions and reduces uncertainty. However, aleatoric and epistemic uncertainties are not calculated separately. Ghobadi and Kang (2022) investigate variational BLSTM model for multi-step (1, 7, and 30 days) ahead forecasting of streamflow time-series at 3 watersheds in the USA and found its performance to be better than other deterministic and probabilistic univariate time-series models. The focus of the study is on forecast accuracy, and the two components of uncertainty are neither reported nor discussed. Sadeghi Tabas and Samadi (2022) use the variational Bayesian dropout method combined with different types of recurrent neural networks (RNNs) for daily streamflow simulations. In this study, with the objective of avoiding overfitting and estimating uncertainty, a proportion of the weights (parameters) of the RNN's are randomly set to zero, and Gaussian noise is added to the remaining weights. The variational Bayesian dropout method, though computationally less expensive, is not Bayesian as the inferences drawn from it are ill-posed (Hron et al., 2017; Li et al., 2022). Additionally, a thorough analysis for finding the probable reasons behind the uncertainty is missing in the study. A few studies have used BNNs without uncertainty estimation (Althoff et al., 2021; Lu et al., 2021). They use BNNs as a tool to improve model performance as compared to other established models rather than as a diagnostic tool to investigate the reason behind the uncertainties. Moreover, the detailed uncertainty analysis, including disentanglement of uncertainties, physical reasons behind the uncertainties, and utility of the identified uncertainties, is largely not addressed in these studies. Further, to the best of my knowledge, uncertainty estimation for satellite-fog detection has never been attempted.

Probabilistic fog detection, along with its uncertainty, will help develop confidence in decision-making. Disentangling the uncertainty into aleatoric and epistemic components will reveal the scenarios where the model is unable to detect fog confidently. In other words, such model will have the ability to know when and why it does not know. The comparison of epistemic and aleatoric uncertainties can indicate future research directions for improving the model in terms of more data collection or adding features to the existing dataset. These factors motivated this study. This study aims to develop a real-time deployable probabilistic satellite-based fog detection method with uncertainty estimation. The specific objectives of the chapter are -

1. To develop a novel satellite-based fog detection method capable of providing the probability of fog along with detection uncertainty.
2. To disentangle fog detection uncertainty into epistemic and aleatoric components and study factors that influence them.

The developed model is applied to INSAT-3D geostationary satellite observations to detect fog over IGP. The efficacy of the model is evaluated by comparing its performance with the INSAT-3D Fog model.

3.2 Study area and datasets

Data from 18 cities spread across the IGP are used in the study. Out of 18 cities, 2 cities (Bareilly and Gorakhpur) are randomly chosen as held-out dataset. The geographical location of the cities is shown in Figure 3.1.

The datasets are divided into two parts: satellite data (i.e., model input) and *in situ* data (i.e., reference data). The *in situ* dataset contains METAR observations. The *in situ* observations with visibility less than 1 km are classified as fog in the reference dataset. The satellite observation dataset obtained from INSAT-3D. INSAT-3D Fog is used as a baseline model in this study. For the proposed BNN model, all the bands are resampled to 4 km resolution.

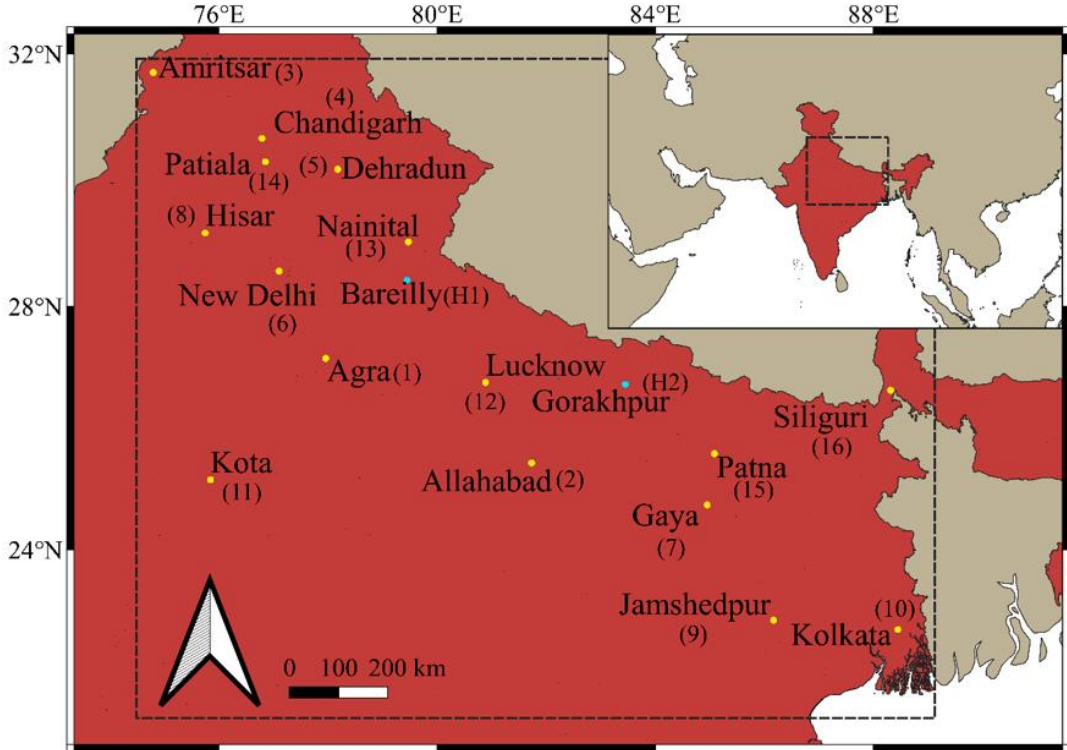


Figure 3.1. Locations of 18 cities in Indo-Gangetic Plains selected for BNN model development. The held-out cities are shown in blue. Keymap in the corner shows the study area (shown by black dashed lines) at a coarser scale. The numbers in the brackets are city codes used in this chapter.

3.3 Methodology

3.3.1 Theoretical background of Bayesian neural networks

In ordinary neural networks (also known as point estimate neural networks), weights (parameters) and networks' output are deterministic quantities, while both weights and outputs of BNNs are random variables characterised by probability distribution functions. Suitable probability distributions are used as prior distribution of weights, which are updated during the model training phase.

Let the training data $D = \{x_i, y_i\}, i = 1, \dots, N$, where x_i and y_i are the features and labels, respectively. The weights (i.e., parameters) of the neural network and their prior distribution are denoted by w and $P(w)$, respectively. To initialise the model, the parameters of the prior distribution of the weights are initialised. The multivariate normal distribution with zero mean and unit standard deviation is used as the prior distribution of weights in this study

(Silvestro & Andermann, 2020). The posterior distribution of weights $P(w|D)$ is learned by applying the Bayes' rule as

$$P(w|D) = \frac{P(D|w)P(w)}{P(D)} \quad (3.1)$$

Since $P(w|D)$ cannot be analytically obtained, it is approximated by a variational distribution of weights with parameters θ denoted by $q(w|\theta)$. The optimum parameter set (θ^*) is derived as,

$$\theta^* = \arg \min_{\theta} KL[q(w|\theta)||P(w|D)] \quad (3.2)$$

Equation 3.2 minimises the Kullback-Leibler (KL) divergence between the variational distribution $q(w|\theta)$ and the true posterior distribution $P(w|D)$. The optimum posterior distribution of weights is learned by minimizing the negative evidence lower bound (ELBO, also known as negative variational free energy), which consists of reconstruction cost (Equation 3.1) and Kullback-Leibler divergence (KLD) cost (Equation 3.2).

$$ELBO = \underbrace{K \times KL[q(w|\theta)||P(w)]}_{\text{KLD cost}} - \underbrace{\mathbb{E}_{q(w|\theta)}[\ln P(D|w)]}_{\text{Reconstruction cost}} \quad (3.3)$$

where, $P(w)$ = Prior distribution of weights,

$P(D|w)$ = Likelihood of the training data for the posterior distribution of weights,

K = weight of KLD in ELBO (termed as KL-weight), and

$\mathbb{E}_{q(w|\theta)}(\cdot)$ = Expectation with respect to variational distribution of weights $q(w|\theta)$.

Unlike the conventional variational inference, the posterior distribution of weights is not tractable in BNNs. Hence, Monte Carlo approximations are used. A back-propagation compatible method, i.e., Bayes by Backprop (Blundell et al., 2015), enables the neural network to learn the posterior distribution.

When the feature \hat{x} from the test dataset is fed to the model, it generates the posterior predictive distribution for \hat{y} as follows,

$$P(\hat{y}|\hat{x}) = \mathbb{E}_{q(w|\theta^*)}[P(\hat{y}|\hat{x}, w)] \quad (3.4)$$

The predictive distribution of the network output is approximated by Monte Carlo simulation in which the weights are randomly sampled from its posterior distribution. The mean of the output samples from the simulations is the prediction (probability of fog) and their standard deviation represents the epistemic uncertainty. The aleatoric uncertainty, unlike the epistemic uncertainty, is obtained by calculating the standard deviation of the neural network output by assuming a suitable distribution. In this study, the aleatoric uncertainty for the binary classification problem is modelled by a Bernoulli distribution (output value varies between 0 to 1 as the probability of fog).

The total predictive uncertainty for the binary classification case is estimated as the sum of aleatoric and epistemic components (Kwon et al., 2020) as,

$$\text{Predictive uncertainty} = \underbrace{\frac{1}{T} \sum_{t=1}^T \sqrt{\hat{y}_t(1-\hat{y}_t)}}_{\text{Aleatoric}} + \underbrace{\sqrt{\frac{1}{T} \sum_{t=1}^T (\hat{y}_t - \bar{y})^2}}_{\text{Epistemic}} \quad (3.5)$$

T is the number of Monte Carlo simulations, \hat{y}_t is the probability (of fog) for simulation number t and

$$\bar{y} = \frac{1}{T} \sum_{t=1}^T \hat{y}_t \quad (3.6)$$

represents the mean prediction. The aleatoric uncertainty is modelled as the standard deviation of the Bernoulli distribution and can have a maximum value of 0.5. The epistemic uncertainty is modelled as the standard deviation of the probability values (i.e., values between 0 to 1), which limits the maximum value of standard deviation to 0.5. Thus, both uncertainties have a maximum limit of 0.5 and the upper limit of total uncertainty is 1.

3.3.2 Reliability of the proposed model

The BNN model generates the probability of fog as an output. Ideally, the model should express less uncertainty for correct fog detections and higher uncertainty for incorrect detections, i.e., the model should not be overconfident for incorrect detections. Such ideal models are known as *calibrated models* in the machine learning literature. A reliability diagram (i.e., calibration curve) tests the calibration of a model. The diagram is prepared by first dividing the prediction interval into M equally spaced bins ($M = 5$ in this study). Then, for each bin, the mean of the prediction probability and the accuracy (defined as the fraction of predictions that are correct) are calculated. A plot between the accuracy and the mean of the prediction probability is the reliability diagram for the model. A model is considered perfectly calibrated if all the points on the reliability diagram fall on a 45° line from the origin. The expected calibration error (ECE) (Guo et al., 2017) is a quantitative metric to assess the calibration of the model.

$$ECE = \sum_{m=1}^M \frac{|B_m|}{n} |acc(B_m) - conf(B_m)| \quad (3.7)$$

Here, B_m is the bin number, n is the number of observations. The acc and $conf$ correspond to the accuracy and mean prediction probability respectively. ECE is the (weighted) deviation of the reliability curve from the 45° line.

ECE gives an idea of how much the probability of a model may deviate from its real value. Reliable models show lesser values of ECE, with ideal value as zero. In this study, the BNN model is also assessed using a reliability diagram to test if the predicted probabilities are reliable.

3.3.3 Feature engineering

The primary inputs for the BNN are 6 bands in the standard product of INSAT-3D (Table 1.1). The band values are converted into radiances using the lookup table provided with the satellite data. The pixels corresponding to the weather station in each city are extracted, resulting in the time-series for each station. BTD, a key feature in the conventional physics-based fog detection

algorithm, is also included in the input features. Thus, 7 features are obtained from the INSAT-3D satellite observations.

In IGP, fog typically exists in early mornings and late evenings, i.e., the fog is not distributed uniformly throughout the day. Hence, the time of the day (in hours) and month become input features. Since, time is a periodic variable, the time of day (hour) is converted to its cosine values and then used as a feature. The transformation also acts as a proxy for the solar zenith angle, which is a feature used in conventional dual-channel fog detection algorithms (Chaurasia & Jenamani, 2017).

Like most meteorological variables, fog also shows temporal persistence. Hence, the past 12 hours of data (24 half-hourly observations) are used to leverage the temporal persistence. Therefore, the input feature size becomes $24 \times 9 = 216$. Apart from diurnal variation and persistence, fog also exhibits spatial variation. Hence, day of season, latitude, longitude, and elevation are also taken as input features, increasing the total number of input features to 220.

The dataset consisting of about 134 thousand observations during the winter months of 2017-22 at 16 cities is split into training-testing at 90-10%. Since the observation period for *in situ* data was not same across cities (due to missing observations), the train-test split was done independently for each city and the data were stacked. 20% of the training dataset is used for validation. These 10% observations (test split) used to evaluate the model results are termed ‘main test dataset’. In addition, the held-out dataset (observations from two cities, namely, Bareilly and Gorakhpur) is used only for testing. Notably, being an infrequent event, fog observations are outnumbered by non-fog observations in the *in situ* dataset, creating a class imbalance. For instance, only 17% of observations in the training dataset belong to the fog class.

3.3.4 Model implementation

The BNN model is implemented in Python using TensorFlow and its probabilistic programming library TensorFlow Probability (TFP; Dillon et al. 2017). The model consists of 4 layers, with input dimension 220. The first two layers consist of n_1 and n_2 neurons, respectively. Both are fully connected (Dense) layers with rectified linear unit (ReLU) activation function. The third layer is a variational inference (TFP DenseVariational) layer added for modelling the epistemic uncertainty. The prior distribution of the weights of this layer is a zero-mean, unit variance multivariate normal distribution. The final output layer consists of Bernoulli distribution that yields the probability of fog and aleatoric uncertainty associated with the output. The negative log likelihood of the Bernoulli distribution is used as the loss function for the network. It should be noted that in a fully Bayesian Neural Networks, all layers are variational layers (TFP DenseVariational). The training of such networks is computationally prohibitive for large datasets. Hence, hybrid Bayesian Neural Networks, consisting of a few deterministic layers followed by one or more variational layers, are popular for practical applications (Chang, 2021).

The model is trained until the convergence of the loss function or for 200 epochs. During the prediction phase, 100 Monte Carlo simulations are carried out, and the mean and the standard deviation of probability outputs are used to assess the results. Figure 3.2 summarises the model implementation (more details about the model are provided in Appendix A3.2). The performance of the model is evaluated using various evaluation metrics reported in the literature (Chaurasia & Jenamani, 2017; Guo et al., 2021; Tang et al., 2022) and are listed in Table 3.2.

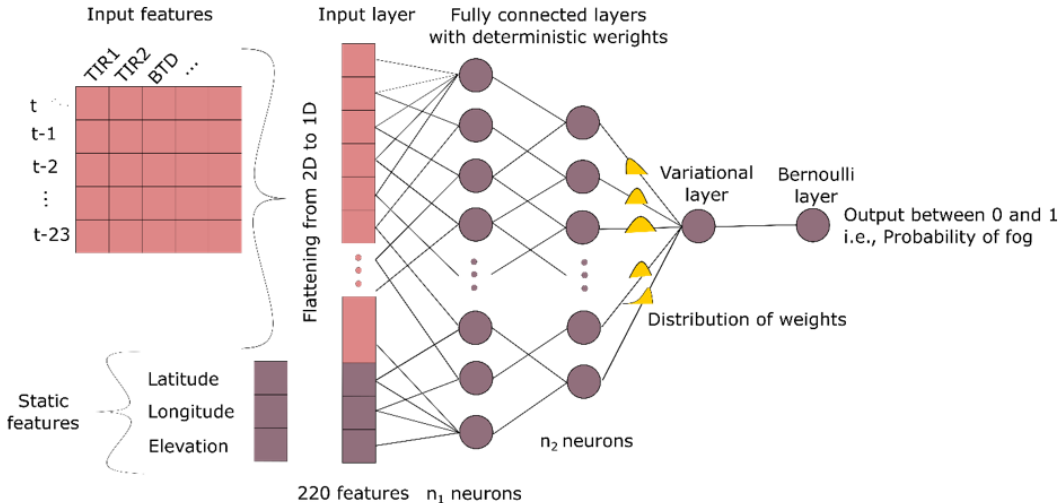


Figure 3.2 Proposed BNN model architecture (n_1 and n_2 are the number of neurons for the fully connected layers with deterministic weights).

3.3.5 Sensitivity analysis for hyperparameters

In the proposed BNN model, several variations in terms of the model architecture and hyperparameters are possible. Variations in model architecture include the number of past observations fed as input, and the number of fully connected and dense-variational layers. The hyperparameters primarily include the parameters for the prior distribution of weights and KL-weight. It also includes the number of neurons, activation function for each layer, number of training epochs, and optimization algorithm. Out of these, the number of past observations, distribution of weights, and KL-weight hyperparameter are deemed to be important for the model performance. Hence, a sensitivity analysis is carried out in which the model performance is evaluated on the validation dataset by changing them, and the results are discussed in Appendix A 3.3, and equivalence of two hyperparameters, viz., KL-weight and standard deviation of prior distribution, is presented in Appendix A 3.4.

3.4 Results

Based on hyperparameter tuning, the number of neurons in the first and second layers of the BNN are set as 120 and 32, respectively, and based on sensitivity analysis, the KL-weight is set as 0.03125 (see Appendices A 3.3 and A 3.4 for details). This section presents the results of

model performance, comparison with the baseline, and uncertainty analysis along with some additional results for specific subsets of the data.

3.4.1 Model results

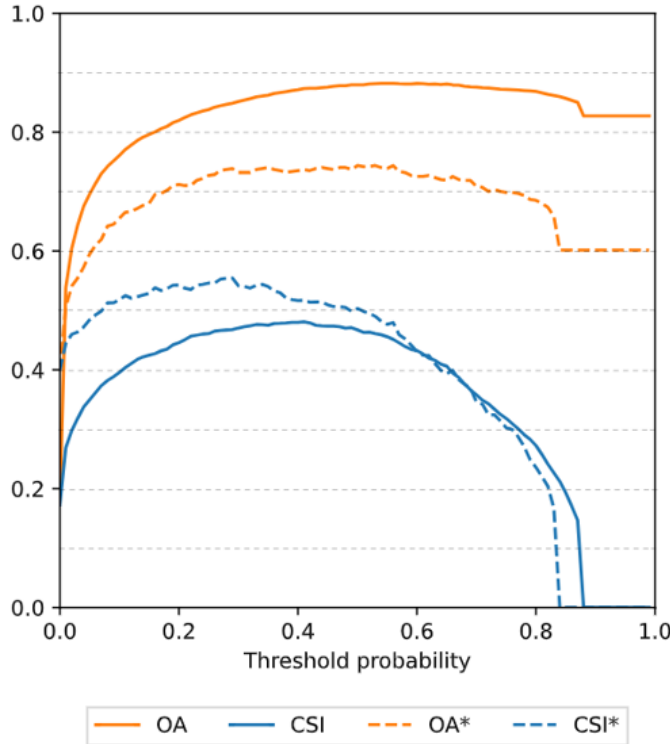


Figure 3.3. Overall accuracy (OA) and critical success index (CSI) for different threshold probabilities for the main test dataset (solid line) and the held-out dataset (dashed line).

Table 3.1. Confusion matrix for the proposed BNN (at threshold probability of 0.4) and the baseline models for main test dataset (values are shown in %). True Positive (TP) and True Negative (TN) denote the observations that the model correctly classifies as fog and no-fog, respectively, while False Positive (FP) and False Negative (FN) denote the observations that the model incorrectly classifies as fog and no-fog, respectively.

		Reference (<i>in situ</i>)	
		Fog	No-fog
Model output	Fog	TP	FP
	No-fog	FN	TN
BNN-based	Fog	11.74	7.14
	No-fog	5.54	75.58
Baseline	Fog	2.22	1.20
	No-fog	14.53	82.05

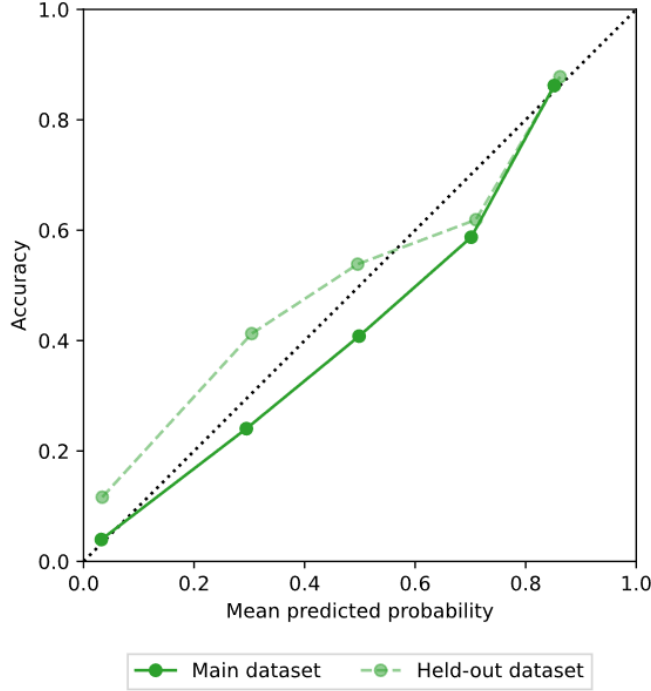


Figure 3.4. Reliability diagram showing the calibration of the proposed BNN-based model for the main test dataset (solid line) and the held-out dataset (dashed line). The dotted line represents the perfectly calibrated classifier.

The model performs probabilistic detection on the test dataset with a Brier score (Wilks, 2006) of 0.09 and an AUROC score (i.e., Area Under Receiver Operating Characteristic curve) of 0.91, indicating that the fog/no-fog classes are well separated. However, converting the probability into fog status (fog/no-fog) needs thresholding. Figure 3.3 shows the variation of overall accuracy (OA) and critical success index (CSI) for different thresholds for both main test and held-out datasets. As the threshold probability increases from 0 to 1, both OA and CSI, first increase and then decrease. This happens because with the increase in threshold probability, precision increases and PoD (recall) decreases (results not shown). However, for the relatively rare events like fog, PoD is more important than OA and precision. The mean CSI over all the thresholds is 0.37. The reliability diagram (Figure 3.4) shows that (qualitatively) the model is reliable as the calibration curves for both main-test and held-out datasets are close to the ideal 45-degree line. The corresponding ECE, is 0.045, which is the expected deviation of predicted probability (and corresponding uncertainty) with the true value.

Table 3.2. Quantitative results of proposed BNN and baseline. TP, TN, FP and FN for main test dataset are defined in Table 3.1. The threshold probability for BNN is 0.4.

	Metric	Formula	BNN	Baseline
PoD	Recall/ Probability of Detection	$\frac{TP}{TP + FN}$	0.679	0.132
CSI	Threat score/ Critical Success Index	$\frac{TP}{TP + FP + FN}$	0.481	0.123
OA	Overall accuracy	$\frac{TP + TN}{TP + TN + FP + FN}$	0.873	0.843
Precision	-	$\frac{TP}{TP + FP}$	0.622	0.648
FNR	False negative rate	$\frac{FN}{TP + FN}$	0.321	0.868
FAR	False alarm rate	$\frac{FP}{FP + TN}$	0.086	0.014
KSS	Hanssen-Kuiper skill score	$PoD \cdot FAR$	0.593	0.118
HSS	Heidke skill score	$\frac{2 \times (TP \times TN - FP \times FN)}{(TP \times FP + FP \times TN) + (TP \times FN + FN \times TN)}$	0.572	0.173
Percent false alarm	-	$\frac{FP \times 100}{TP + FP + FN}$	7.14	1.21
Percent miss	-	$\frac{FN \times 100}{TP + FP + FN}$	5.54	14.53

3.4.2 Comparison with baseline

To compare with the baseline model, the probabilistic outputs of the BNN model are thresholded to binary fog status. The maximum CSI for the training dataset is observed at a probability of 0.4, which is set as the optimum threshold to get the binary fog status output. The confusion matrices of both the proposed and baseline models for main test dataset are shown in Table 3.1, and the evaluation metrics are shown in Table 3.2. (It should be noted that, all the results shown hereafter correspond to main test dataset.) The CSI of the proposed BNN-based model and INSAT-3D Fog are 0.48 and 0.12, respectively. The corresponding PoDs are 0.68 and 0.13, respectively. Hence, the BNN-based model performs significantly better than the baseline. It should be noted that the OAs of both the models are similar (and consistent with the accuracy evaluation described in Appendix A3.1, which is an artefact of the imbalanced dataset). BNN-based model outperforms INSAT-3D Fog in all metrics except percent false alarm, false alarm rate, and precision (with a small margin). This suggests that BNN-based model may sometimes give false alarms. However, in the context of fog detection, false alarms are usually less harmful than missed detections.

Table 3.3. Various statistics related to uncertainty analysis. TP, TN, FP and FN are defined in Table 3.1 and CV denotes coefficient of variation.

	Aleatoric				Epistemic			
	TP	FP	TN	FN	TP	FP	TN	FN
Mean	0.417	0.463	0.155	0.352	0.031	0.040	0.012	0.033
Median	0.428	0.487	0.102	0.396	0.029	0.038	0.004	0.033
CV	0.160	0.102	0.938	0.355	0.386	0.393	1.360	0.573
Mean			0.219				0.017	
Median			0.179				0.011	
CV			0.798				1.079	

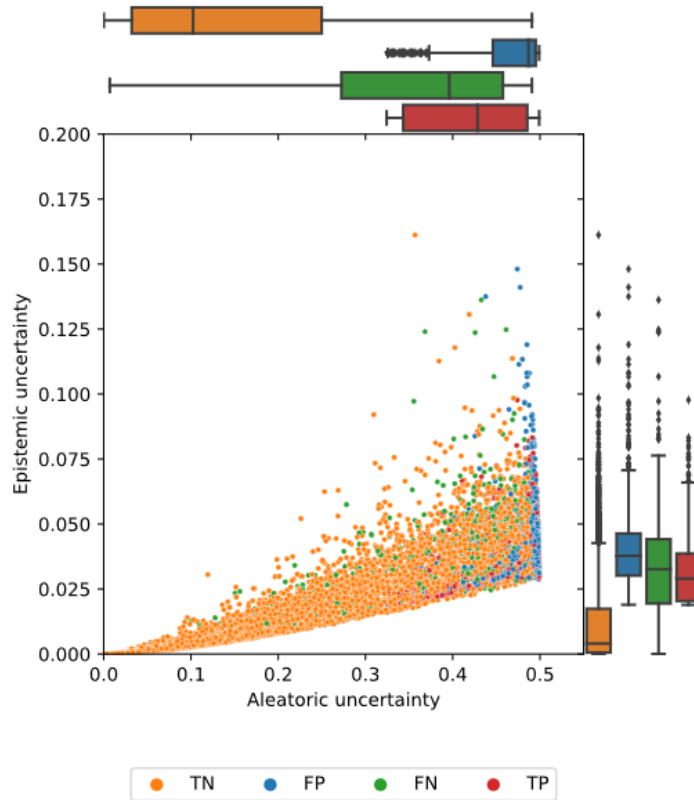


Figure 3.5. Scatterplot showing the relation between aleatoric and epistemic uncertainty. The boxplots for aleatoric and epistemic uncertainty are shown on the top and right, respectively.

Table 3.4. Model performance by limiting total uncertainty. The critical success index (CSI) and probability of detection (PoD) are defined in Table 3.2.

Total uncertainty	CSI	PoD
<0.4	0.576	0.631
<0.5	0.532	0.640
<0.6	0.481	0.679
≥ 0.6	0.480	0.679

3.4.3 Uncertainty analysis

Figure 3.5 presents the distribution of two components of uncertainties and their scatterplot. The corresponding statistics are presented in Table 3.3. The comparison of both uncertainties shows that the aleatoric uncertainty is generally higher (mean of 0.219 in main test dataset) than the epistemic uncertainty (mean of 0.017). The variation of aleatoric uncertainty in terms of maximum and minimum values is also higher than the epistemic uncertainty. However, the coefficient of variation (CV) of the aleatoric uncertainty is lesser (0.8) than the epistemic uncertainty (1.1). The scatterplot in Figure 3.5 shows that the epistemic uncertainty is usually high for predictions having higher aleatoric uncertainty. The colours (corresponding to correct and incorrect detections) shown in the scatterplot depend on the threshold probability (chosen as 0.4). However, the values of aleatoric and epistemic uncertainties are independent of the threshold.

Table 3.3 and the boxplots in Figure 3.5 show that both uncertainties are comparatively low for no-fog observations as compared to fog observations. In general, both uncertainties are lower for correct detections (TNs and TPs) than incorrect detections (FNs and FPs), i.e., the model is more confident about correct detections. Moreover, FPs have the highest uncertainties as compared to others. For observations with higher aleatoric uncertainty, the epistemic uncertainty is high for fog observations compared to no-fog observations due to class imbalance in the training dataset. In both types of uncertainties, the mean value is more than the median caused due the presence of some observations having large uncertainty. However, for both types of uncertainties in the case of TP, FP, and FN, the mean is close to the median. On the other hand, TNs have a very large mean as compared to the median caused by some observations with large uncertainty. The ratio of aleatoric uncertainty to epistemic uncertainty for all four classes varies from 10 to 14 (average is 12.8 over all classes). In other words, on average, the aleatoric uncertainty for any class is ~13 times the epistemic uncertainty. For both uncertainties, the CV is lower for positives (TPs and FPs) than negatives (TNs and FNs). This again can be attributed to data imbalance as there are less fog observations than no-fog observations. The relatively

smaller values of the epistemic uncertainty (in terms of mean and median) suggest that the model has sufficient training data. On the other hand, efforts should be taken to reduce the aleatoric uncertainty.

The model performance is also evaluated for the observations within the given total uncertainty range (Table 3.4). It is evident that the model performance is better for the observations corresponding to lesser uncertainty. In other words, the model gives higher uncertainty to observations that are difficult to predict. For practical applications, such observations may be classified by human experts rather than just relying on the model. The examples of fog detection and uncertainty maps generated by the model are shown in Appendix A3.5.

3.4.4 Classification results for different subsets

The results in the previous section are calculated for the entire test dataset. However, it is important to understand the model performance for subsets of the test dataset, e.g., different fog categories, hours of day, and cities. These results are presented in the following subsections.

3.4.4.1 Model performance for different visibility based fog-categories

The model performance is better for lower visibility ranges as well as for no-fog category (Table 3.5). In other words, the model identifies dense and very dense fog observations (and no-fog observations) better than lighter fog observations. The proposed model performs better than the baseline for different fog categories also (results not shown). It is found that the median value of visibility for FN is 0.96 km, which is very close to 1 km as compared to TP (median value 0.64 km). Similarly, the FP (median value 1.77 km) are closer to 1 km threshold as compared to TN (median value 2.49 km). This shows that the fog is typically misclassified by a smaller margin of visibility. Despite the higher performance for the Shallow fog observations, the shallow fog observations are higher in number (60% of the fog observations) and hence affect the overall performance. As the visibility range increases till 1000 m, the median values of aleatoric and epistemic uncertainty generally increases. This indicates that the model is more

Table 3.5. Model performance for different visibility-based fog-categories.

Visibility range (m)	Fog category	Proportion (%)	PoD	Median aleatoric uncertainty	Median epistemic uncertainty
0-50	Very dense	2.18	0.931	0.337	0.020
50-200	Dense	1.52	0.855	0.400	0.027
200-500	Medium	3.07	0.762	0.416	0.030
500-900	Shallow	4.36	0.665	0.442	0.032
900-1000	Shallow	6.16	0.515	0.431	0.032
1000 and above	No-fog	82.72	0.914	0.123	0.005

Footnote to Table 3.5- The proportion is calculated w.r.t. total observations in main test dataset. Since the values of critical success index (CSI) are calculated for a particular visibility range, they are same as overall accuracy and probability of detection defined in Table 3.2.

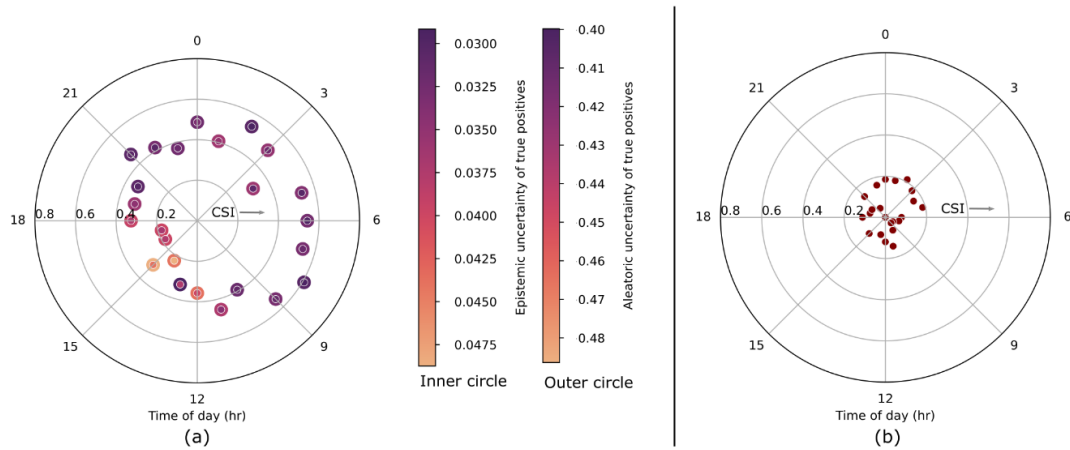


Figure 3.6. Model and baseline performance for different hours of the day. Critical success index (CSI) is denoted in radial direction. (a) The aleatoric and epistemic uncertainties of correct fog detections (TPs) are represented by colour shades of outer and inner circles respectively. (b) The CSI values for the different hours for the baseline are shown. The time of day is shown in local time (GMT+5:30 hours).

uncertain in identifying lighter fog observations. Fog no-fog observations, both the uncertainties are significantly lower, indicating an ample amount of training data and features to identify no-fog observations. One of the probable reasons for the misclassification of lighter fog observations can be the presence of hygroscopic aerosols altering the visibility without the formation of fog-droplets (Deying et al., 2021).

3.4.4.2 Diurnal variation of CSI

Conventional BTD threshold-based methods have different fog detection methods for day, night, and dawn-dusk. Moreover, it is reported that the fog detection accuracy reduces at dawn-

dusk (Chaurasia & Jenamani, 2017; Ma et al., 2023). Hence, for the proposed model, the variation of the model and baseline performances for different hours of the day are also calculated and shown in Figure 3.6. The model performance in terms of CSI is generally better till noon, compared to afternoon hours. Afternoon hours are the period with the least fog probability, which may have caused a suboptimal performance. The highest CSI is observed around 9 am. It is also observed that the morning hours have the highest proportion of fog observations, and the highest model performance is for these hours. In other words, model performance is better for the foggiest hours. Moreover, for these hours, aleatoric and epistemic uncertainty (Figure 3.6 a) for TPs are also relatively low.

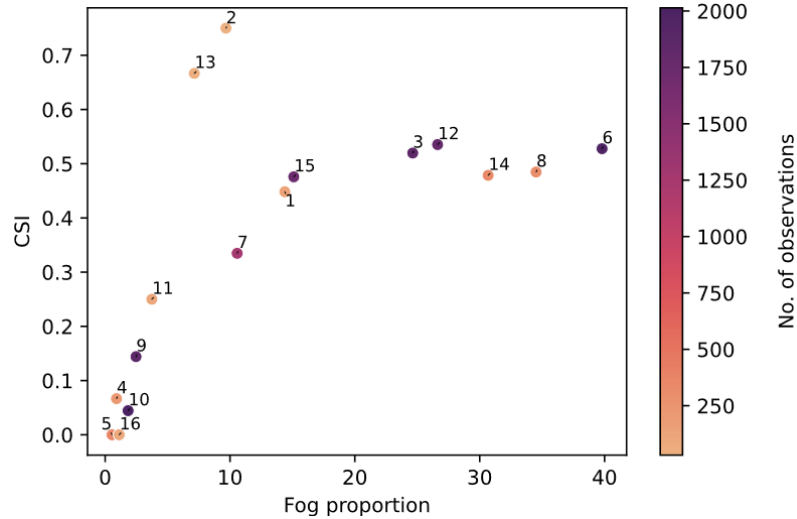


Figure 3.7. Variation of CSI for different cities against the fog proportion (in %). The colour shade represents the count of observations in the main test dataset for the given city. The cities corresponding to the numbers on the plot are shown in Fig. 3.1.

3.4.4.3 City-wise variation of CSI

Figure 3.7 shows that the model performance varies significantly among the cities. This may be due to factors including local topography, land cover, presence of moisture and aerosol sources. The cities with a higher proportion of fog observations generally show higher CSI. The cities shown by darker points denote a higher number of total observations in the main test dataset and hence provide more assured results. The cities showing CSI less than 0.1 are Chandigarh, Dehradun, Kolkata, and Siliguri. The only coastal city in the study area, Kolkata, has different fog characteristics compared to the other cities of IGP in terms of shorter duration of fog events

with predominantly light fog and early dissipation (discussed in previous chapter), which may be a reason for the suboptimal performance for this city. The remaining cities, Dehradun, Siliguri, and Chandigarh are surrounded by hilly areas with high topographical variability. The 4 km resolution satellite data may be too coarse to appropriately represent the *in situ* observations in these cities, resulting in relatively lower values of CSI. It should be noted that except Kolkata, these cities have less than 250 observations in main test dataset, out of which less than 5% are fog observations. Such small number of fog observations limits the reliability of the model performance for these cities as compared to other cities with larger number of fog observations.

3.5 Discussion

The BNN-model provides an estimate of fog probability. A decision maker, depending upon the application, can decide a threshold probability to declare the presence of fog. A conservative approach would be to select a smaller threshold. The variation of CSI for different thresholds (Figure 3.3) shows that the CSI first increases with the threshold, reaches a zone of high value where the variations are relatively small, and then decreases. It becomes zero after the threshold value of 0.85, i.e., no true positives are detected at such a high probability. Since fog is an infrequent event, the BNN is always unsure about the fog and thus does not generate high probabilities for fog. Due to this bias, the CSI value at 0.4 threshold (0.481) is slightly higher than that at 0.5 threshold (0.467). Nevertheless, the BNN model significantly outperforms the baseline model even at that threshold.

Figure 3.3 shows that for the held-out dataset, the CSI values are generally higher, but slightly jittery, as compared to the main test dataset. The jittery nature may be an artefact of the comparatively lesser number of observations present in the held-out dataset. The main test dataset came from the same 16 cities that were used for training and validating the BNN model. Hence, the better performance of the model on the held-out dataset, which was not at all used during model development, may appear counter-intuitive. This may be because the main test dataset results represent combined performance over 16 cities, in which the results vary

significantly (see Figure 3.3), compared to just 2 cities in the held-out dataset. Nevertheless, the results of the held-out dataset signify that the BNN model has good generalization performance can be deployed for fog detection over the entire study area (IGP).

A few studies have reported that the BNNs can outperform ordinary neural networks (Ghobadi & Kang, 2022), whereas a few other studies have reported that this is not always the case (Nolde & Lasowski, 2021). Our analysis found that the BNN and an equivalent (based on model architecture) ordinary neural network have similar performance in terms of CSI and accuracy. Moreover, ordinary neural networks may get overconfident and miscalibrated (non-reliable) model. The weakly informed prior distribution for BNN weights and sufficiently large training data may be the reasons for the similar performance of the two neural networks. However, the BNN has advantages over the ordinary neural network as it provides prediction uncertainty along with its aleatoric and epistemic components.

The limitations of the proposed model include limitations related to the variational inference algorithm, model implementation, and input data. The mean field variational inference algorithm implemented in this study approximates the posterior distribution of model parameters (weights) as a product of independent distributions over each parameter. The proposed model is developed for the purpose of real-time implementation (producing half-hourly updates), and hence, the size of the neural network has practical limitations in terms of time of execution (refer Appendix A3.2). The model has been deployed for real-time fog detection over IGP using INSAT-3D satellite observations.

In the present study, the satellite observations (with a spatial resolution 4×4 km) are compared with *in situ* observations. There can be situations where most of the pixel area is covered with fog; however, there is no-fog in the proximity of the sensor (and vice-versa). Such scenarios are more likely in hilly terrains having high topographical variability. Sometimes, the visibility can be lowered due to non-fog events, e.g., smoke, dust storms, and heavy rainfall. On other occasions, fog can be present beneath a cloud, and its detection by satellites may be

difficult. Observations corresponding to such situations lead to a higher aleatoric uncertainty. This situation can also be thought of as the ‘nugget’ in geostatistical terms. This uncertainty is irreducible in the present dataset. However, it can be reduced with finer-resolution satellite products. Low-cost visibility sensors and crowdsourcing by citizen scientists can also assist in monitoring fog by developing a dense network of *in situ* fog (visibility) observation stations. Additionally, *in situ* observations (visibility, relative humidity) and gridded covariables (e.g., land cover, NDVI) with finer resolution may also reduce uncertainty (Deshpande et al., 2019). The problem of uncertainty disentanglement, its communication to decision-makers, and the use of innovative technologies for hydrologic measurement are outlined as one of the 23 unsolved problems in hydrology (Blöschl et al., 2019). The first two points are mainly discussed in this study, whereas the third point is considered as a future scope.

3.6 Chapter summary

In the present study, satellite-based fog detection is carried out by Bayesian Neural Network (BNN) using INSAT-3D satellite observations. The half-hourly *in situ* airport weather (METAR) observations are used as the ground reference dataset. Observations from 2017 to 2022 for 16 cities are used for model training and testing. Data from 2 cities are kept as held-out dataset and used only for testing. The model inputs are selected in such a way that the model can be implemented in real-time. The model estimates the probability of fog and its associated uncertainty along with aleatoric and epistemic components of uncertainty. The following conclusions are drawn from the chapter:

- (i) The proposed BNN-based algorithm is better at detecting fog than the conventional dual-channel method in terms of the critical success index (0.48 against 0.12), and probability of detection (0.68 against 0.13) for a probability threshold of 0.4.
- (ii) The BNN-based algorithm enables the provision of both, aleatoric and epistemic uncertainties associated with each model output and allows the user to choose a suitable threshold to detect fog status.

(iii) In general, aleatoric uncertainty is higher than epistemic uncertainty for fog detection. Hence efforts should be made to reduce the aleatoric uncertainty for more confident model outputs, by exploring additional suitable features and reducing the spatial and temporal resolution of the input data, e.g., pollution data, high-resolution satellite imagery.

This chapter is a modified version of two publications cited below:

Deshpande, P., Tripathi, S., & Bhattacharya, A. (2024). Bayesian Neural Networks for Satellite Fog Detection: Quantifying Epistemic and Aleatoric Uncertainties. *Remote Sensing in Earth Systems Sciences*. <https://doi.org/10.1007/s41976-024-00155-7>

Deshpande, P., Tripathi, S., & Bhattacharya, A. (2022). Comparison of in-situ fog observations with INSAT-3D satellite fog product for North Indian cities. *IGARSS 2022 - 2022 IEEE International Geoscience and Remote Sensing Symposium*, 6460–6463. <https://doi.org/10.1109/IGARSS46834.2022.9883759>

4 MEDIUM-RANGE FOG FORECASTING

4.1 Introduction

Fog forecasting is a major step in mitigating fog-related hazards. Thus, numerous research efforts are aimed at improving fog forecasting, making it a broad field of research. Forecasting methods can be categorised in several ways: by lead time/forecast horizons (nowcasting, medium-range forecasting, and long-range/seasonal forecasting) and by classification type (binary and multi-class). Binary forecasts are fog or no-fog, whereas multi-class forecasts are classes associated with different visibility ranges. Unlike classification, some forecasts provide the visibility value directly (i.e., regression). Lastly, fog forecasting approaches are divided into two categories based on methodology: statistical methods and physics-based methods.

Statistical (also known as data-driven) methods use past meteorological observations to identify patterns in fog occurrence. These methods range from classical time-series models (e.g., ARIMA; Srivastava et al., 2017) to advanced machine learning techniques like deep learning (e.g., LSTMs; Miao et al., 2020). Statistical approaches are typically location-specific, relying on hydro-meteorological time-series data from specific sites, and their ability to generalise to larger regions is limited. Despite their limitations, statistical methods are widely used due to their computational efficiency and simplicity (Arun et al., 2022; Colabone et al., 2015; Sharma et al., 2024). Recent advancements in fog forecasting include the use of satellite-based observations in data-driven models (Bari et al., 2023; Kim et al., 2023). However, since these methods do not model the associated meteorological variables, they are useful for only nowcasting (short-range forecasting with a lead-time of up to 6 hours).

Physics-based methods rely on numerical weather prediction (NWP) models, which simulate primary atmospheric variables like temperature, wind speed, and specific humidity using the fundamental laws of physics (Gultepe et al., 2007). These primary variables are then converted into visibility using parameterization schemes (Tang et al., 2009; Velde et al., 2010; Zhou et al., 2007). One popular example is the Weather Research and Forecasting (WRF) model

using VIS-RH parameterization scheme that estimates visibility using relative humidity (Lee et al., 2021; Payra & Mohan, 2014; Pithani et al., 2019; Pu et al., 2016; Wagh et al., 2023). Since the physics of fog formation is not well understood, no universally accepted parameterization scheme exists (Long et al., 2021). The parameterization schemes are often calibrated using *in situ* hydro-meteorological measurements and have poor generalization performance. A review of the past NWP-based fog forecasting methods is provided in Appendix A4.1. It reveals that most studies have focused on threshold visibility of 500 m or less rather than the WMO-specified threshold of 1 km. As the lead time increases, the error component and corresponding computational cost also increase in NWPs (Singh et al., 2025). Thus, medium-range fog forecasts for up to 5 days or longer are not yet widely studied.

Machine learning weather prediction models (MLWPs), such as GraphCast, developed by Google DeepMind (Lam et al., 2023), mark a significant advancement in weather forecasting by leveraging machine learning techniques. GraphCast employs graph neural networks (GNNs) to represent the Earth's atmosphere as a graph, with nodes and edges capturing spatial relationships. This approach enables the model to efficiently learn complex, non-linear interactions in atmospheric data, offering improved accuracy and computational efficiency compared to traditional NWP models. GraphCast uses recent weather states from reanalysis datasets (e.g. ERA5; Rasp et al. 2024) as inputs and forecasts future weather states, maintaining the same spatial-temporal resolution and variable set as the input data.

GraphCast's innovation lies in its ability to provide accurate forecasts of meteorological variables, such as temperature, pressure, and wind speed, over a 10-day horizon at six-hour intervals. Studies, such as the WeatherBench2 (Rasp et al., 2024), demonstrate that GraphCast outperforms traditional forecasting systems, including the widely used IFS (Integrated Forecasting System, Rasp et al. 2024). GraphCast is designed for downstream applications, however there aren't many such studies (Feldmann et al., 2024; Flora & Potvin, 2024; Suri et al., 2024; Yan et al., 2024). While GraphCast is not explicitly designed for fog forecasting, its precise forecasts of fog-covariates make it a valuable tool for fog forecasting. Integrating data-

driven models like GraphCast with post-processing techniques opens opportunities for developing fog forecasting models. However, such models are not yet explored.

A hybrid model that combines the strengths of physics-based and statistical methods could address the limitations of existing fog forecasting models. In this chapter a model is evolved, named FogCast, by integrating GraphCast and Bayesian Neural Networks (BNNs).

FogCast is evaluated on the fog-prone region of IGP, which has been a testbed for developing fog forecasting models for forecasting research (Pithani et al., 2020; Smith et al., 2023) and operational (Arun et al., 2022; NCMWRF, 2025; Sharma et al., 2024) applications. However, most fog forecasts available at airports in IGP are typically for 3 days lead time (Jayakumar et al., 2021). Medium-range forecast models (with a lead time of 5 days) recently proposed by Bajaj et al. (2024) do not forecast fog directly but provide fog index, a combined measure of fog duration and intensity. Further, these forecast models are site-specific. Thus, fog forecasts with a lead time of 10 days are not yet available for the entire IGP.

The specific objectives of this chapter are as follows:

1. To develop FogCast, a medium-range (10 days lead time) fog forecasting model based on GraphCast.
2. To evaluate the model performance for different lead times and visibility-based fog types.
3. To disentangle the aleatoric and epistemic components of uncertainty in the fog forecasts.

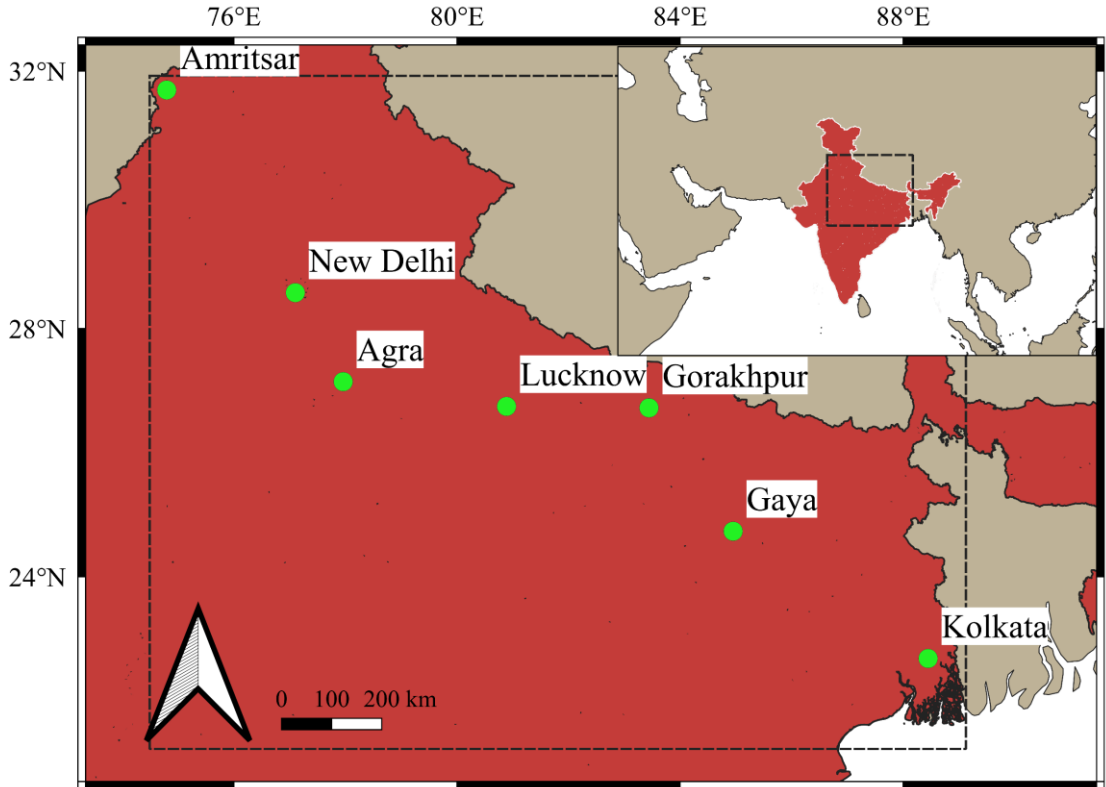


Figure 4.1. Locations of 7 cities (green circles) in Indo-Gangetic Plains used for model training and testing. The keymap shows the study area (shown by black dashed lines) at a coarser scale.

This study distinguishes itself by evaluating FogCast on multiple winter seasons and across geographically diverse sites in the IGP, ensuring robustness and scalability. FogCast is trained and tested for various lead times ranging from 6 hours to 10 days.

4.2 Datasets and study area

The datasets used in this chapter are categorised into two types: *in situ* observational (METAR) data (used as labels or reference data or ground truth) and weather forecast data (used as input features, i.e., input data). Observations with visibility below 1 km are classified as fog events in the reference dataset.

The weather forecast dataset is derived from GraphCast, which includes surface-level variables and variables at different pressure levels. Surface-level variables include temperature at 2 m above ground, U and V components of wind at 10 m, and total precipitation over the last six hours. For this study, we use variables corresponding to the 1000 hPa pressure level, as it closely represents near-surface conditions where fog forms. The variables at 1000 hPa include

temperature, specific humidity, and U, V , and W components of wind. Historical GraphCast forecasts (Lam et al., 2023; Rasp et al., 2024) are utilised for training and evaluating FogCast. For real-time fog forecasting, operational GraphCast forecasts by NOAA are used (NOAA, 2025).

The study focuses on the winter season (November to February) from 2017 to 2023 for training and evaluating the model. GraphCast weather forecast data are extracted for grid points corresponding to seven cities (airports): Agra, Amritsar, Delhi, Gaya, Gorakhpur, Kolkata and Lucknow (Figure 4.1). These cities are selected because they have at least 25 fog observations (visibility < 1 km) in the METAR dataset during the study period. Thus, the dataset comprises ~13000 observations, out of which ~ 20% are fog observations.

Fog, like many hydro-meteorological variables, exhibits temporal autocorrelation. Therefore, lagged GraphCast forecasts up to the past 24 hours (4 time-steps) are used as input features to capture diurnal variations and temporal dependencies in fog. In addition, the input features included the day of the corresponding winter season (DOS) and the hour of the day (Hour). To preserve the cyclic nature of DOS and Hour, both variables are converted to cosine values. The resulting time-series of the input features, along with their lagged counterparts and corresponding binary labels (fog/no-fog), are fed into the FogCast for training and testing.

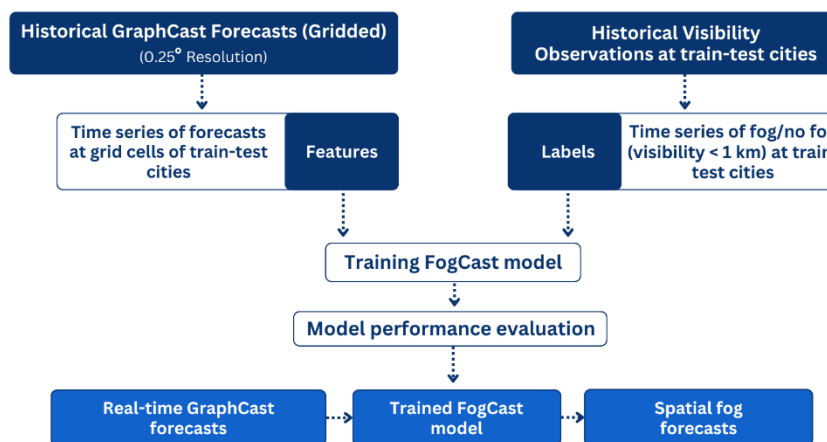


Figure 4.2 Flowchart showing the methodology of FogCast: GraphCast-based fog forecasting model.

4.3 Methodology

An overview of the methodology is provided in Figure 4.2 and its details are elaborated in this section.

4.3.1 Model architecture

The theoretical background of BNNs is already discussed in Section 3.3.1. The BNN model architecture developed in a Python environment using the TensorFlow Probability (TFP) library is as follows: The first layer of the BNN model is a fully connected (TFP dense) layer with 120 neurons and uses the ReLU activation function. This pattern is repeated with a subsequent dense layer of 32 neurons. The third layer, a variational inference (TFP DenseVariational) layer, is added to model epistemic uncertainty. The prior distribution of the weights in this layer is defined as a zero-mean, unit variance multivariate normal distribution. The final output layer employs a Bernoulli distribution to produce the probability of fog and the associated aleatoric uncertainty. The network uses the negative log-likelihood of the Bernoulli distribution as its loss function which is optimised using a stochastic gradient descent algorithm. Since fog observations in the METAR dataset are four times more than the no-fog observations, a class imbalance exists. To compensate for the class imbalance, a weighted loss function is used that penalises the misclassification of fog observations 4 times more than the misclassification of no-fog observations. The model is trained until the loss function converges or for a maximum of 200 epochs. For the trained model, 20 Monte Carlo simulations are performed, and the mean and standard deviation of the probability of fog forecasts are calculated to evaluate the results. The probability values thus obtained are converted into fog/no-fog based on a threshold of 0.5.

Figure 4.3 provides an overview of model architecture.

4.3.2 Training and testing

FogCast aims to forecast fog at locations where *in situ* visibility observations may not be available. To mimic this situation, leave-one-out cross-validation (LOOCV) is used. In each iteration, data from a single city is excluded from the training set and used as the test set, while

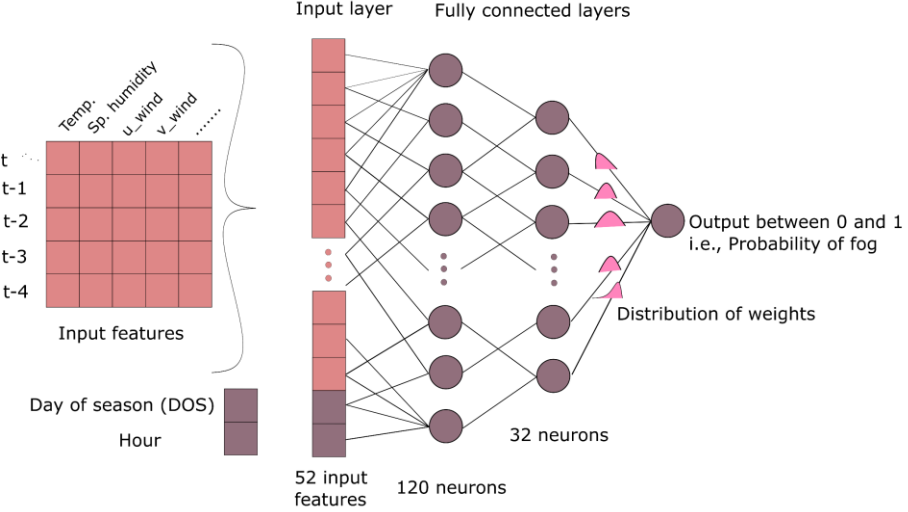


Figure 4.3. Bayesian neural network used in the FogCast.

data from the remaining cities form the training set. This process is repeated until every city has been used as the test set exactly once. The results are calculated as a weighted sum (based on the number of fog observations) over all iterations.

4.3.3 Feature importance analysis

To understand the impact of each input feature on the FogCast forecasts, an ablation study is also carried out using SHAP (SHapley Additive exPlanations) values (Lundberg & Lee, 2017). SHAP values provide a unified measure of feature importance by attributing the impact of each input feature on fog forecast. For each feature, the SHAP value calculation considers all possible subsets of features, excluding the one being evaluated. The FogCast forecast is computed for each subset. A SHAP summary plot is obtained across all lead times and all test cities together to get an overall idea of the importance of features.

4.4 Results and discussion

4.4.1 Model evaluation

FogCast forecasts fog at every six hours up to 10 days. However, for model evaluation, lead times of 6, 12 hours and 1, 2, 5, and 10 days are selected, and the performance for the shortest and the longest lead times is presented in Table 4.1 and Figure 4.4. As expected, the model performance is generally better for shorter lead times. However, the most striking result is that the model's performance (in terms of CSI) at 10 days lead time is within 20% of the

performance at 6-hour lead time. Thus, the model is capable of forecasting fog for longer lead times without significant deterioration in performance is likely a consequence of GraphCast's ability to forecast meteorological variables at longer lead times (Lam et al., 2023). FogCast performance is compared with both statistical (Kim et al., 2024; Sharma et al., 2024) and NWP-based fog forecasting studies in IGP (Parde et al., 2022; Payra & Mohan, 2014; Singh et al., 2018). The CSI values of the existing studies vary from 0.27 to 0.65, whereas the PoD and FAR values vary from 0.60 to 0.95 and 0.04 to 0.43, respectively (detailed results are provided in Table A4.1). However, all past models have different visibility thresholds, spatiotemporal resolutions, and testing locations, with the longest lead-time of up to 2 days (except one study with 5 days lead-time), making one-to-one comparison difficult. Nevertheless, FogCast shows comparable performance (in terms of CSI, PoD, and FAR) to these past studies, even with a lead time that is more than twice as long as theirs.

Figure 4.4 shows that both aleatoric and epistemic uncertainty (median values) increase as the lead time increases. Thus, as expected, the model is relatively more confident in forecasting a shorter lead time, and it becomes more and more uncertain as the lead time increases. A detailed discussion of uncertainty analysis is provided in a later subsection.

Table 4.1. Model performance for fog forecasting averaged over all lead times

Metric	Range	Ideal value	Formula	Lead time	
				6 hours	10 days
Critical Success Index (CSI)	[0,1]	1	$\frac{TP}{TP + FP + FN}$	0.440	0.362
Overall Accuracy (OA)	[0,1]	1	$\frac{TP + TN}{TP + FP + FN + TN}$	0.776	0.684
Probability of Detection (Recall)	[0,1]	1	$\frac{TP}{TP + FN}$	0.766	0.712
Precision	[0,1]	1	$\frac{TP}{TP + FP}$	0.517	0.444
False Alarm Rate	[0,1]	0	$\frac{FP}{TN + FP}$	0.228	0.328

TP: correctly forecasted fog observation (hit), TN: correctly forecasted no-fog (correct negative), FP: incorrectly forecasted no-fog (false alarm), FN: incorrectly forecasted fog (miss).

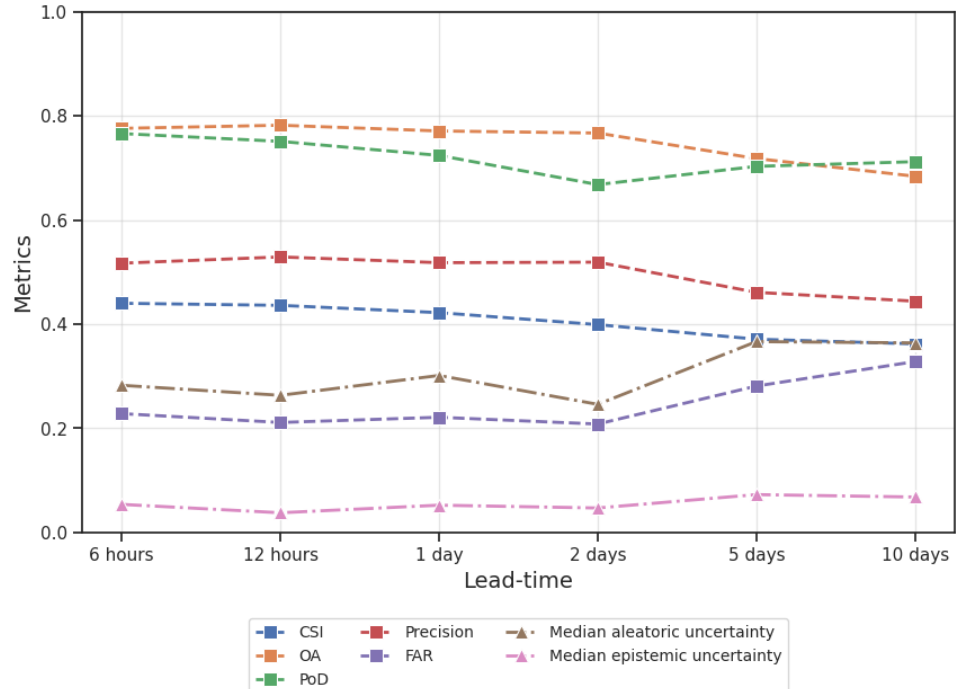


Figure 4.4. FogCast performance for different lead times across all seven cities during testing. The formulae for the metrics used are provided in Table 4.1.

Table 4.2. Model performance for different visibility-based fog categories for 6-hour and 10-day lead times and all seven cities during testing.

Visibility range (m)	Fog category	Fog (%)	PoD		Median aleatoric uncertainty		Median epistemic uncertainty	
			6-hour	10-day	6-hour	10-day	6-hour	10-day
Lead times								
0-50	Very dense	2.52	0.95	0.93	0.28	0.33	0.06	0.06
50-200	Dense	1.62	0.92	0.86	0.28	0.37	0.05	0.06
200-500	Medium	3.15	0.83	0.76	0.30	0.39	0.06	0.06
500-1000	Shallow	10.52	0.68	0.62	0.35	0.39	0.07	0.07
Above 1000	No-fog	82.19	0.83	0.68	0.20	0.35	0.04	0.06

4.4.2 Model evaluation for visibility-based fog categories

In the previous subsection, the model results are provided for the entire visibility range; however, it is important to understand the model performance for different visibility-based fog categories since they have different impacts. The results for different fog categories are presented in Table 4.2. The model shows higher performance for dense and very dense fog categories. However, since the proportion of shallow fog is higher as compared to dense and very dense fog, the model's overall performance is dominated by its performance in shallow fog category. Lastly, both uncertainties (especially aleatoric uncertainty) are generally lower for no-fog and dense and very dense fog, indicating that the FogCast confidently forecasts these fog categories as compared to shallow fog. A possible reason for the misclassification of shallow fog observations could be the presence of hygroscopic aerosols, as discussed in the previous chapter.

4.4.3 Uncertainty analysis

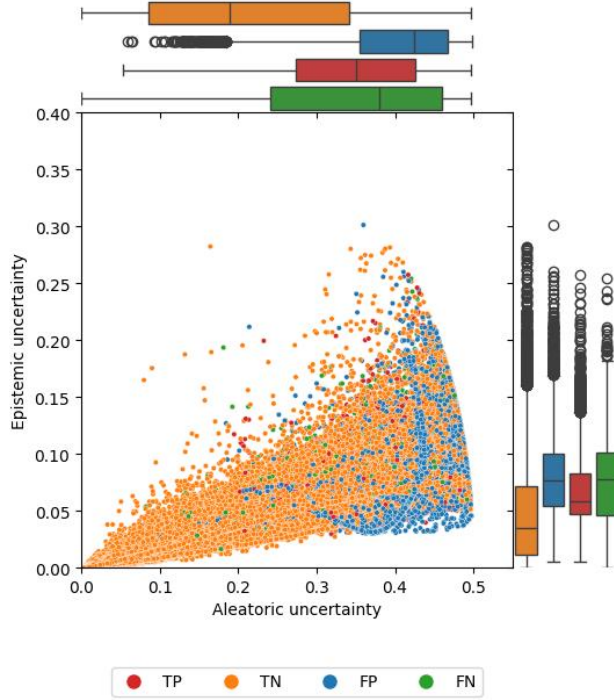


Figure 4.5. Scatterplot for aleatoric and epistemic uncertainty. The boxplots for aleatoric and epistemic uncertainties are shown on the top and right, respectively

Table 4.3. Various statistics related to uncertainty analysis. CV denotes the coefficient of variation.

	Aleatoric				Epistemic			
	TP	FP	TN	FN	TP	FP	TN	FN
Mean	0.34	0.40	0.22	0.34	0.07	0.08	0.05	0.07
Median	0.35	0.42	0.19	0.38	0.06	0.08	0.04	0.08
CV	0.28	0.20	0.69	0.40	0.45	0.41	0.87	0.53
Mean	0.27				0.06			
Median	0.28				0.05			
CV	0.56				0.67			

Figure 4.5 displays the distribution of aleatoric and epistemic uncertainties along with their scatterplot, and Table 4.3 presents the corresponding statistics. The analysis reveals that aleatoric uncertainty is generally higher than epistemic uncertainty, with mean values of 0.27 and 0.06, respectively, suggesting sufficient training data but insufficient features to separate fog/no-fog classes. The coefficient of variation for aleatoric uncertainty (0.56) is lower than epistemic uncertainty (0.67) indicating that though the aleatoric uncertainty may take higher values, epistemic uncertainty has larger variation. The scatterplot suggests that forecasts with

higher aleatoric uncertainty often have higher epistemic uncertainty. Table 4.3 and boxplots of Figure 4.5 highlight that correct forecasts (true positives, TPs, and true negatives, TNs) have lower median aleatoric and epistemic uncertainties than incorrect forecasts (false positives, FPs, and false negatives, FNs). Thus, FogCast is more confident in correct forecasts than incorrect forecasts.

4.4.4 Feature importance

The feature importance estimated in terms of SHAP values is plotted in Figure 4.6 (a). The position on the x-axis shows the SHAP values and the y-axis shows the input features such as temperature, humidity, or wind speed. The top features have a higher average impact on the forecast. The temperature 2 m above ground is found to be the most influential feature, followed by the specific humidity at 1000 hPa. These two variables control the relative humidity that plays a crucial role in fog formation. The plot also shows that the temperature at 2 m above ground has higher importance than the temperature at 1000 hPa, indicating that the fog formation is more influenced by the features at the surface level. Wind components, along with mean sea level pressure, are identified as the most influencing factor after temperature and specific humidity.

The Hour variable representing the time of day is also found to be important, i.e., the time of the day also affects the chances of fog. This inference is aligned with fog climatology in IGP that suggests a strong diurnal pattern in fog occurrence with most fog observed during dawn, dusk, and night-time (as discussed in Chapter 2). The rest of the input features have low SHAP values, indicating an insignificant contribution to fog forecasting. Latitude, longitude, and elevation of cities were initially included as input features. However, they had very small SHAP values, and their inclusion did not show improved performance; therefore, they are not used in the final FogCast model. Though widespread fog episodes may show spatial continuity, the limited number of cities under study limits learning of these spatial connections.

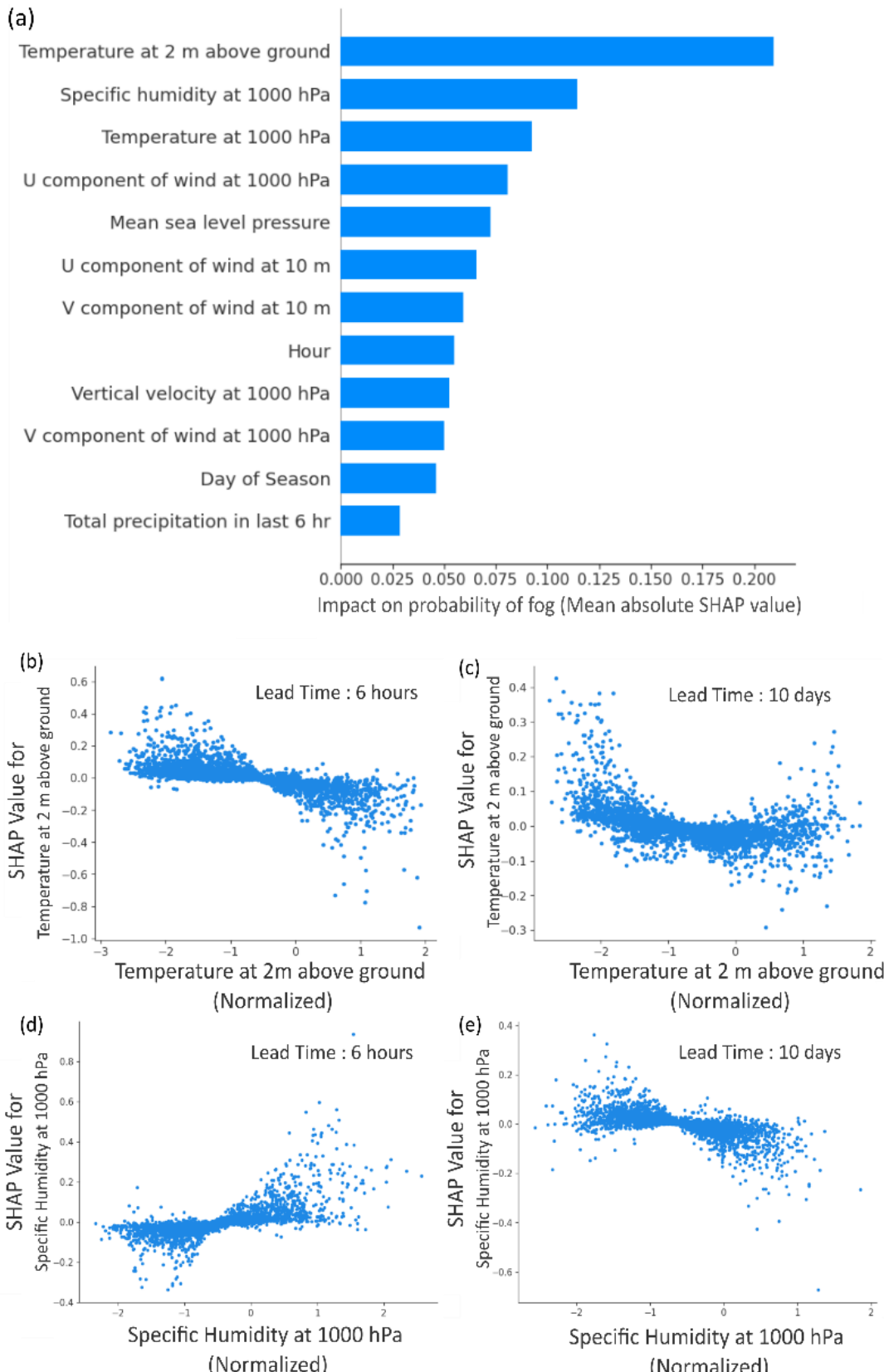


Figure 4.6. (a) Feature importance plot showing the input features in descending order of feature importance. (b,c,d,e) Scatterplots for normalised feature value and corresponding SHAP value. The positive SHAP value (shown on Y axis) represents higher fog probability and vice versa.

To study the effect of temperature at 2 m above the ground and specific humidity at 1000 hPa. on fog forecasting for individual observations at different lead times, scatterplots are drawn between SHAP values and these features (Figure 4.6 b to e). For lower values of temperature and higher values of specific humidity, the SHAP values are positive, suggesting a higher probability of fog. This pattern is clearly visible in lead time of 6 hours (Figure 4.6 b and d) but not with a lead time of 10 days (Figure 4.6 c and e) suggesting that the relationship between fog and temperature/humidity obtained from GraphCast weakens with lead time.

Lastly, the importance of features depends primarily not only on physical relationships but also on topography. For example, IGP is heavily dominated by radiation fog (and not precipitation fog); thus, the SHAP analysis has not identified precipitation as an important feature. In other regions, precipitation may be identified as an important feature. In the regions of advection fog, wind may appear as an important feature. Thus, different features may be identified as important at different locations, improving our understanding of the fog formation process.

Table 4.4. Model performance for a severe fog event in Delhi (India) on 14th January 2022. (Times shown are in Indian Standard Time, i.e., IST).

Date of forecast	Lead time	14-Jan-22		
		0:30	6:30	12:30
13-Jan-22	6 hours	✓	✓	✓
13-Jan-22	12 hours	✓	✓	✓
13-Jan-22	1 day	✓	✓	✓
12-Jan-22	2 days	✓	✓	X
9-Jan-22	5 days	✓	✓	X
4-Jan-22	10 days	✓	✓	✓
Correct forecasts out of 6		6	6	4

✓ = correct forecast, X= incorrect forecast

4.4.5 Realism of FogCast forecasts

The results shown in the previous section provide the quantitative performance of the model. However, a popular way to assess the weather forecast model performance is to study its performance for an extreme weather event (Price et al., 2024). This chapter presents FogCast performance for 2 fog events with longer duration and thicker fog appearance, one over New Delhi on 14th January 2022 and another over many parts of IGP on 4th January 2025.

Western disturbances are one of the major causes of widespread dense fog events in IGPs by providing large amounts of moisture content. One such western disturbance was observed near Delhi on 13th January 2022 (Hunt et al., 2025) followed by a fog event in Delhi. In this study, the model performance is studied for a severe fog event that happened in Delhi on 14th January 2022. It was the longest reported fog event, with visibility of less than 300 m for most of the event. This fog event caused severe disruptions in transportation services, including flight delays (TIE, 2022; TOI, 2022). The FogCast could identify this fog event with even 10 days lead time (Table 4.4). For lead-times of 6 hours to 10 days, the corresponding mean aleatoric uncertainty values vary from 0.34 to 0.41, whereas median epistemic uncertainty values vary from 0.04 to 0.06. This shows that the model is more confident about the forecasts with shorter lead time.

To study the performance of the model for real-time spatial forecasting a recent fog event that occurred on 4th January 2025 is selected. Figure 4.7 shows 1-day lead-time forecast for 4 January 2025 at 5:30 am IST by FogCast, while Figure 4.8 displays the corresponding fog detected by INSAT-3D Fog. The cells corresponding to a probability of more than 0.5 can be considered as fog. The area under the fog appears largely similar in both images, suggesting that the fog forecasted by FogCast agrees with the fog detected by INSAT-3D Fog. Table 4.5 compares the FogCast forecast with INSAT-3D Fog and observations at METAR sites for this fog event. The FogCast forecasts closely align with METAR observations, particularly in Amritsar, Delhi, and Lucknow, where all three sources agree on fog occurrence. Similarly, in Kolkata, there is an agreement on no-fog occurrence. In Agra (and Gorakhpur), both FogCast and INSAT-3D Fog show agreement on fog (and no-fog), however, METAR observations are

unavailable for these two cities. In New Delhi, both METAR and FogCast report its presence, but INSAT-3D Fog reports no-fog. Lastly, in Gaya, FogCast and INSAT-3D Fog show conflicting results. Since the corresponding METAR observation is missing, it is unclear which one is more accurate. Nevertheless, FogCast performs comparably to METAR observations and INSAT-3D Fog, both qualitatively and quantitatively.

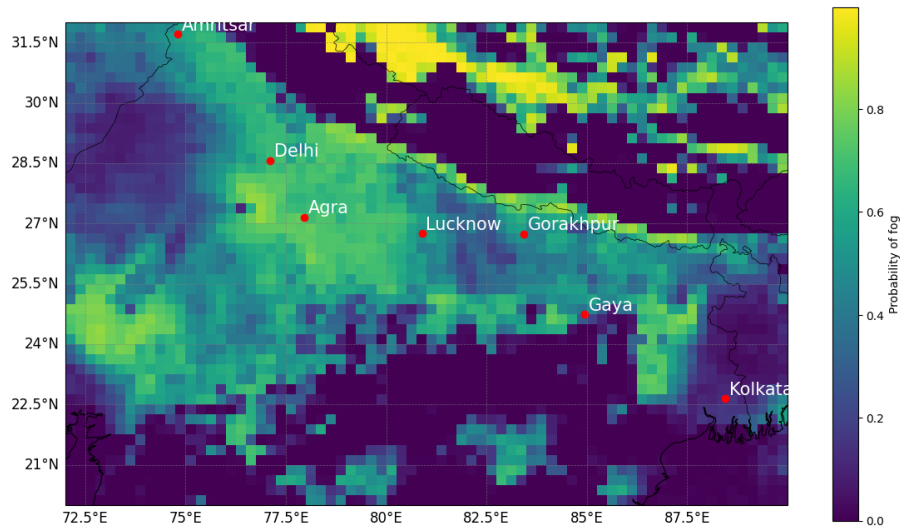


Figure 4.7 Probability of fog for 4 January 2025 at 5:30 am IST, forecasted by FogCast with 1-day lead-time.

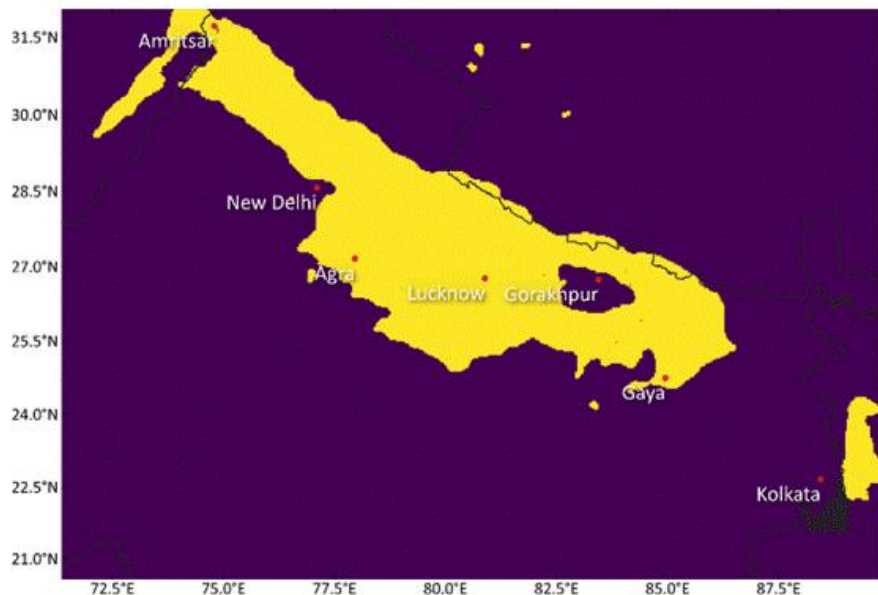


Figure 4.8 INSAT-3D Fog map for 4 January 2025 at 5:30 am IST. Yellow colour represents fog and purple no-fog.

Table 4.5. Comparison of fog forecast from FogCast, fog detection from INSAT-3D Fog, and fog observations from METAR on January 4, 2025, at 5:30 AM IST, based on Figures 4.7 and 4.8.

City	METAR	FogCast	INSAT-3D Fog
Amritsar	Fog	Fog	Fog
New Delhi	Fog	Fog	No fog
Agra	No data	Fog	Fog
Lucknow	Fog	Fog	Fog
Gorakhpur	No data	No fog	No fog
Gaya	No data	No fog	Fog
Kolkata	No data	No fog	No fog

4.4.6 Further discussion

To understand the contribution of the lagged features towards the model performance, the FogCast is trained and tested without the lagged features. The comparison of model performance with and without lagged features shows a modest decrease in CSI (and in PoD) but an increase in uncertainties (especially aleatoric uncertainty). Thus, the temporal autocorrelation contributes to the model performance, though its importance decreases with the lead time (Table A4.2 in Appendix).

The details of the model performance for each city in the LOOCV method reveal that the CSI values vary significantly. In the case of Kolkata and Gaya, the model performance is inferior compared to the remaining cities (Table A4.3 in Appendix). The nature of fog in Kolkata is different from other cities in IGP due to its proximity to the coast (as discussed in Chapter 2) posing a limitation on the model performance. In the case of Gaya, the dataset contains only 29 fog observations (~3% of all observed data in Gaya) with no dense and very dense fog observations. Since FogCast performance for medium and shallow fog is relatively lower compared to dense and very dense fog (Table 4.2), it is reflected in lower values of CSI and PoD but a higher value of OA for Gaya.

In the FogCast model, the default probability threshold is kept at 0.5, and the binary fog forecasts are used in the performance evaluation. However, the users may directly use the probability of fog rather than the binary fog forecasts. To compare the forecast probabilities and

actual probabilities, a reliability diagram (discussed in Section 3.3.2). The calibration curve (Figure A4.1 in Appendix) for FogCast shows some deviation from the ideal curve around a probability of 0.5 indicating an underprediction. Since dense, very dense fog and no-fog are better forecasted by the model, very high and very low probability values are better calibrated (showing lesser deviation) than the probability values around 0.5, which typically represent shallow and medium fog.

4.4.7 Limitation and future scope

Though FogCast forecasts fog with reasonable accuracy, there are cases of incorrect forecasts (i.e., misclassification) arising from multiple sources – (a) reanalysis dataset used as input in GraphCast: the reanalysis datasets, while comprehensive, have inherent limitations in their agreement with ground-based hydro-meteorological observations; (b) forecasts from GraphCast used as inputs in FogCast: GraphCast may have errors in reproducing reanalysis data on which it is trained; (c) imperfect relationship between FogCast input features and fog; (d) mismatch between the spatial resolution of the input features and *in situ* observations: input features obtained from GraphCast have a spatial resolution of 0.25 degree, while *in situ* visibility observations are point measurements resulting in discrepancy. For example, fog may exist near the location of the point measurement but be absent in the rest of the GraphCast grid cell or vice versa.

The FogCast forecasts fog in a binary classification only. However, multi-class classification (and regression) forecasts are more informative, but challenging due to severe class imbalances as compared to the binary fog forecasts and can be considered for future development. In this study, the input features at surface-level and 1000 hPa pressure level is used because fog is a near-surface phenomenon. GraphCast provides forecasts at 37 pressure levels, which can be explored in future; however, it will lead to higher storage and computational costs. It is also noticed that though GraphCast claims to be computationally more efficient than NWP models, running it on a desktop computer remains challenging. For

example, preprocessing the input data for GraphCast needs a substantial amount of random-access memory (>128 GB).

FogCast provides forecasts at 6-hour intervals because input features from GraphCast are available at that interval. However, a model can be developed to forecast fog at hourly intervals even when the input features are at 6-hour intervals. Such a model can be useful for forecasting the onset and dissipation of fog events.

During the development of FogCast, several machine learning models (e.g., Random Forest and XGBoost) and deep learning models specialised in time-series forecasting (e.g., LSTMs and Transformers) were evaluated. However, their performance did not show any significant improvement compared to BNNs. The limited number of features present in the dataset may be the cause; however, recent advances in foundation models for time-series forecasting (Rasul et al., 2023) can be explored. Further, spatial-information-aware deep learning models, including diffusion models (Shi et al., 2024), can also be explored for capturing spatial relationships in the data. Although FogCast uses GraphCast forecasts, the methodology can be adapted for other MLWPs, e.g., GenCast (Price et al., 2024), FuXi (Chen et al., 2023), FourCastNet (Kurth et al., 2023). This flexibility allows FogCast to be integrated with the best available weather forecasts (or their combinations) for any region.

4.5 Chapter summary

FogCast, a Bayesian neural network-based probabilistic fog forecasting model, is developed utilizing GraphCast weather forecasting system. FogCast is tested for multiple winter seasons (2017–2023) across seven cities in IGP. The model forecasts fog at 6-hour intervals with lead times ranging from 6 hours to 10 days. The critical success index (CSI) of the model varies from 0.44 for 6 hours lead time to 0.36 for 10 days lead time. These results are comparable to other studies, although they have shorter lead times. The higher CSI values, even at longer lead times, underscores the model's robustness in maintaining reliable forecasts, making it particularly valuable for operational medium-range forecasts.

The model shows strong performance in detecting very dense fog (visibility < 50 m), achieving a probability of detection exceeding 90%. The feature importance analysis identified temperature at 2 m above ground and specific humidity at 1000 hPa as the most important features for fog forecasting. The aleatoric uncertainty in fog forecasts is generally higher than the epistemic uncertainty, suggesting that more informative features are required to improve the model performance. Lastly, the realism of FogCast is tested on two severe fog events in the study area.

This chapter is a modified version of an article (under review) with the following details:

Deshpande, P., Agarwal, S., Bansal, K., Bhattacharya, A., & Tripathi, S. (2025). FogCast: Probabilistic Medium Range Fog Forecasting using Global Machine Learning Weather Prediction Model, *Quarterly Journal of the Royal Meteorological Society*.

5 SUMMARY AND CONCLUSIONS

5.1 Summary and conclusions

This thesis studied fog phenomenon over the Indo-Gangetic Plains (IGP), with a focus on developing a methodology for regional fog detection and forecasting. Fog significantly disrupts transportation, agriculture, and public health, particularly in IGP, which experiences dense fog during winter months. The thesis presented the climatology and typology of fog in the IGP and developed a probabilistic satellite-based fog detection product and a spatial medium-range fog forecasting model.

The study employed a range of datasets, including METAR *in situ* observations, INSAT-3D geostationary satellite observations, and GraphCast weather forecasts. The *in situ* observations provided visibility and meteorological data that served as reference datasets (i.e., labels) for fog detection and forecasting models. On the other hand, INSAT-3D observations and GraphCast forecasts served as the input data (i.e., features) for the fog detection and forecasting model, respectively. Since fog observations are rare as compared to no-fog observations, critical success index (CSI) and probability of detection (PoD) were used for evaluating the model performance.

First, the climatology and typology of the fog in IGP was studied. This was an essential step for developing fog detection and forecasting models. The climatology and typology study revealed that radiation fog is predominantly observed in the region. A comparison with fog studies in other regions of the world showed that fog events in IGP are relatively thicker (very low visibility) and longer.

Next, a Bayesian neural network (BNN) model was proposed that uses INSAT-3D satellite observations for probabilistic fog detection. The BNN can quantify both aleatoric and epistemic uncertainties. This makes the model more robust and reliable, particularly when data imbalance or noisy inputs pose challenges. The study also evaluated the contribution of temporal persistence by incorporating lagged features into the model, significantly enhancing accuracy of the models. The proposed model outperformed baseline methods, such as the

INSAT-3D Fog product, in detecting fog. Metrics like CSI and PoD indicated that the BNN-based model is better at identifying fog events, especially for thicker fog conditions.

Finally, a BNN-based probabilistic fog forecasting model named FogCast was developed. FogCast utilises the GraphCast weather forecasts. FogCast was tested for multiple winter seasons (2017–2023) across seven cities in IGP. The model forecasts fog at 6-hour intervals with lead times ranging from 6 hours to 10 days. FogCast's CSI varied from 0.44 for 6 hours lead-time to 0.36 for 10 days lead-time. These metrics were similar to other fog forecasting studies but with shorter lead times. Even at longer lead times, the higher CSI values underscored the model's robustness in maintaining reliable forecasts, making it particularly valuable for operational medium-range forecasts. The model excelled in detecting dense fog (visibility < 50 m) with a probability of detection over 90%. The ablation study showed temperature at 2 m above ground and specific humidity at 1000 hPa to be the most important features for fog forecasting. Higher aleatoric uncertainty in the forecasts suggested the need for more informative features to enhance performance.

The real-time results generated by the models developed in the thesis are disseminated freely and publicly at <https://fog.iitk.ac.in/>.

5.2 Future directions

The BNN model developed for satellite-based fog detection can also be applied to obtain satellite fog climatology. Unlike fog-climatology based on limited *in situ* observations, satellite-fog-climatology can investigate both spatial and temporal fog patterns leading to better understanding of fog (Pauli et al., 2022). Further, satellite-based fog detection can be integrated with fog forecasting models like FogCast to improve their spatial and temporal resolutions. This may help in forecasting fog onset and dissipation. Moreover, additional data-sources related to fog (e.g., real-time air quality, soil moisture) can also be used as input features of FogCast. Since these input features may have different spatio-temporal resolutions generative ML models capable of handling multimodal can be explored.

5.2.1 Development of low-cost sensors and citizen science

The geographically sparse network of conventional visibility sensors in IGP highlights a need for developing alternate methods for fog monitoring. Low-cost visibility sensors and citizen science initiatives can further enhance fog monitoring by establishing a comprehensive network of *in situ* fog (visibility) observation stations. The development of low-cost camera-based sensors for fog monitoring is already going on at IITK Fog Observatory. These sensors can be used in citizen science projects to create spatially dense fog datasets. Moreover, federated learning and edge computing techniques can be used to maintain the privacy of individual users and allow them to monitor fog even without internet access. These datasets, after ensuring their reliability, can improve our understanding of fog formation and can open new avenues for research in this area.

5.2.2 Relationship between fog and agriculture

Fog may affect agriculture by acting as a source of water for irrigation and on the other hand, irrigation may affect the formation of fog. Additionally, agricultural practices like crop residue burning may affect the fog lifecycle by altering the aerosol concentration in the atmosphere. However, these relationships between fog and agriculture are largely unexplored for IGP.

5.2.3 Improved dissemination of fog forecasts

Currently, in the IITK fog portal fog forecasts are available for sites where *in situ* visibility observations are available. Users have to manually select a site of their interest. The future scope includes location-based automated fog alerts for the users. Moreover, transportation delays can be estimated beforehand by integrating fog forecasting and travel planning tools. The medium-term fog forecasts may also help to improve agricultural advisories related to irrigation, fertilisers and pesticides.

Presently fog is not listed as a natural hazard by National Disaster Management Authority of India. However, fog can significantly disrupt transportation, increase accident rates (Khodadadi-Hassankiadeh et al., 2020; Singh, 2017), and impact health and agriculture leading

to disastrous situations. Considering fog as a hazard is important because it would prompt better preparation and response strategies, such as improved forecasting, hazard mitigation planning, and policy changes. Recognizing fog as a hazard could lead to greater resource allocation for mitigating its impacts on public safety and economic activities, especially in fog-prone regions like IGP.

This chapter is a modified version of an article (under review) with the following details:

Deshpande, P., Bhattacharya, A., & Tripathi, S. (2025). Data-Driven Fog Forecasting for North India, *Current Science*.

REFERENCES

- Abdar, M., Pourpanah, F., Hussain, S., Rezazadegan, D., Liu, L., Ghavamzadeh, M., Fieguth, P., Cao, X., Khosravi, A., Acharya, U. R., Makarenkov, V., & Nahavandi, S. (2021). A review of uncertainty quantification in deep learning: Techniques, applications and challenges. *Information Fusion*, 76, 243–297. <https://doi.org/10.1016/j.inffus.2021.05.008>
- Aditi, A., Ashrit, R., 2021. Assessment of Forecast Skill of High- and Coarse-Resolution Numerical Weather Prediction Models in Predicting Visibility/ Fog Over Delhi, India. *Curr Sci*, 120, 676. <https://doi.org/10.18520/cs/v120/i4/676-683>
- Adler, R. F., Huffman, G. J., Chang, A., Ferraro, R., Xie, P.-P., Janowiak, J., Rudolf, B., Schneider, U., Curtis, S., Bolvin, D., Gruber, A., Susskind, J., Arkin, P., & Nelkin, E. (2003). The Version-2 Global Precipitation Climatology Project (GPCP) Monthly Precipitation Analysis (1979–Present). *Journal of Hydrometeorology*, 4(6), 1147–1167. [https://doi.org/10.1175/1525-7541\(2003\)004<1147:TVGPCP>2.0.CO;2](https://doi.org/10.1175/1525-7541(2003)004<1147:TVGPCP>2.0.CO;2)
- Akimoto, Y., & Kusaka, H. (2015). A climatological study of fog in Japan based on event data. *Atmospheric Research*, 151, 200–211. <https://doi.org/10.1016/j.atmosres.2014.04.003>
- Althoff, D., Rodrigues, L. N., & Bazame, H. C. (2021). Uncertainty quantification for hydrological models based on neural networks: the dropout ensemble. *Stochastic Environmental Research and Risk Assessment*, 35(5), 1051–1067. <https://doi.org/10.1007/s00477-021-01980-8>
- Arun, S. H., Singh, C., John, S., Diwakar, S. K., Sankhala, D. K., Nigam, N., Tomar, C. S., & Kumar, G. (2022). A study to improve the fog/visibility forecast at IGI Airport, New Delhi during the winter season 2020–2021. *Journal of Earth System Science*, 131(2), 124. <https://doi.org/10.1007/S12040-022-01874-5>
- Babu, S. S., Manoj, M. R., Moorthy, K. K., Gogoi, M. M., Nair, V. S., Kompalli, S. K., Satheesh, S. K., Niranjan, K., Ramagopal, K., Bhuyan, P. K., & Singh, D. (2013). Trends in aerosol optical depth over Indian region: Potential causes and impact indicators. *Journal of Geophysical Research: Atmospheres*, 118(20), 11,794-11,806. <https://doi.org/10.1002/2013JD020507>
- Bajaj, K., Mannam U., Deshpande, P. J., Patil Y., Bhattacharya A., and Tripathi S.: Forecasting of Fog Index and Prediction Interval using Bayesian Methods (2024). Proceedings of the 7th Joint International Conference on Data Science & Management of Data (11th ACM IKDD CODS and 29th COMAD), December 18-21, 2024, Jodhpur, India.
- Bari, D., Lasri, N., Souri, R., & Lguensat, R. (2023). Machine Learning for Fog-and-Low-Stratus Nowcasting from Meteosat SEVIRI Satellite Images. *Atmosphere*, 14(6). <https://doi.org/10.3390/atmos14060953>
- Barton, Y., Sideris, I. V., Germann, U., & Martius, O. (2020). A method for real-time temporal disaggregation of blended radar–rain gauge precipitation fields. *Meteorological Applications*, 27(1), e1843. <https://doi.org/10.1002/met.1843>

- Behrouz, M., & Alimohammadi, S. (2018). Uncertainty analysis of flood control measures including epistemic and aleatory uncertainties: Probability theory and evidence theory. *Journal of Hydrologic Engineering*, 23(8). [https://doi.org/10.1061/\(ASCE\)HE.1943-5584.0001675](https://doi.org/10.1061/(ASCE)HE.1943-5584.0001675)
- Belorid, M., Lee, C. B., Kim, J. C., & Cheon, T. H. (2015). Distribution and long-term trends in various fog types over South Korea. *Theoretical and Applied Climatology*, 122(3–4), 699–710. <https://doi.org/10.1007/s00704-014-1321-x>
- Beven, K. (2012). *Rainfall-Runoff Modelling*. Wiley. <https://doi.org/10.1002/9781119951001>
- Blöschl, G., Bierkens, M. F. P., Chambel, A., Cudennec, C., Destouni, G., Fiori, A., Kirchner, J. W., McDonnell, J. J., Savenije, H. H. G., Sivapalan, M., Stumpf, C., Toth, E., Volpi, E., Carr, G., Lupton, C., Salinas, J., Széles, B., Viglione, A., Aksoy, H., ... Zhang, Y. (2019). Twenty-three unsolved problems in hydrology (UPH) – a community perspective. *Hydrological Sciences Journal*, 64(10), 1141–1158. <https://doi.org/10.1080/02626667.2019.1620507>
- Blundell, C., Cornebise, J., Kavukcuoglu, K., & Wierstra, D. (2015). Weight uncertainty in neural networks. *32nd International Conference on Machine Learning, ICML 2015*, 2, 1613–1622. <https://doi.org/1505.05424>
- Boutle, I.A., Finnenkoetter, A., Lock, A.P., Wells, H., 2016. The London Model: Forecasting fog at 333 m resolution. *Quarterly Journal of the Royal Meteorological Society*, 142, 360–371. <https://doi.org/10.1002/qj.2656>
- Chang, D. T. (2021). Hybrid Bayesian Neural Networks with Functional Probabilistic Layers. *arXiv preprint arXiv:2107.07014*. <https://doi.org/10.48550/arXiv.2107.07014>
- Chaurasia, S., & Jenamani, R. K. (2017). Detection of fog using temporally consistent algorithm with INSAT-3D imager data over India. *IEEE Journal of Selected Topics in Applied Earth Observations and Remote Sensing*, 10(12), 5307–5313. <https://doi.org/10.1109/JSTARS.2017.2759197>
- Chen, L., Zhong, X., Zhang, F., Cheng, Y., Xu, Y., Qi, Y., & Li, H. (2023). FuXi: a cascade machine learning forecasting system for 15-day global weather forecast. *Npj Climate and Atmospheric Science*, 6(1). <https://doi.org/10.1038/s41612-023-00512-1>
- Colabone, R. D. O., Ferrari, A. L., Tech, A. R. B., & Vecchia, F. A. da S. (2015). Application of Artificial Neural Networks for Fog Forecast. *Journal of Aerospace Technology and Management*, 7(2), 240–246. <https://doi.org/10.5028/jatm.v7i2.446>
- Croft, P.J., Pfost, R.L., Medlin, J.M., Johnson, G.A., 1997. Fog Forecasting for the Southern Region: A Conceptual Model Approach. *Weather Forecast*, 12, 545–556. [https://doi.org/10.1175/1520-0434\(1997\)012<0545:FFTSR>2.0.CO;2](https://doi.org/10.1175/1520-0434(1997)012<0545:FFTSR>2.0.CO;2)
- Cséplő, A., Sarkadi, N., Horváth, Á., Schmeller, G., & Lemler, T. (2019). Fog climatology in Hungary. *Quarterly Journal of the Hungarian Meteorological Service (Időjárás)*, 123(2), 241–264. <https://doi.org/10.28974/idojaras.2019.2.7>

- Deshpande, P. J., Sure, A., Dikshit, O., & Tripathi, S. (2019). A framework for estimating representative area of a ground sample using remote sensing. *The International Archives of the Photogrammetry, Remote Sensing and Spatial Information Sciences, XLII-2/W13(2/W13)*, 687–692. <https://doi.org/10.5194/isprs-archives-XLII-2-W13-687-2019>
- Dey, S., Tripathi, S. N., Singh, R. P., & Holben, B. N. (2004). Influence of dust storms on the aerosol optical properties over the Indo-Gangetic basin. *Journal of Geophysical Research: Atmospheres, 109(D20)*, D20211. <https://doi.org/10.1029/2004JD004924>
- Deying, W., Jizhi, W., Yuanqin, Y., Liangke, L., Junting, Z., & Yaqiang, W. (2021). Formation mechanism of heavy haze-fog associated with the interactions between different scales of atmospheric processes in China. *Atmospheric Pollution Research, 12(6)*, 101085. <https://doi.org/10.1016/j.apr.2021.101085>
- Dillon, J. V., Langmore, I., Tran, D., Brevdo, E., Vasudevan, S., Moore, D., Patton, B., Alemi, A., Hoffman, M., & Saurous, R. A. (2017). *TensorFlow Distributions*. <https://arxiv.org/abs/1711.10604v1>
- Dimri, A. P., Niyogi, D., Barros, A. P., Ridley, J., Mohanty, U. C., Yasunari, T., & Sikka, D. R. (2015). Western Disturbances: a review. *Reviews of Geophysics, 53(2)*, 225–246. <https://doi.org/10.1002/2014RG000460>
- Ding, Y. H., & Liu, Y. J. (2014). Analysis of long-term variations of fog and haze in China in recent 50 years and their relations with atmospheric humidity. *Science China Earth Sciences, 57(1)*, 36–46. <https://doi.org/10.1007/s11430-013-4792-1>
- Dimitrova, R., Sharma, A., Fernando, H.J.S., Gultepe, I., Danchovski, V., Wagh, S., Bardoe, S.L., Wang, S., 2021. Simulations of Coastal Fog in the Canadian Atlantic with the Weather Research and Forecasting Model. *Boundary Layer Meteorol, 181*, 443–472. <https://doi.org/10.1007/s10546-021-00662-w>
- Feldmann, M., Beucler, T., Gomez, M., & Martius, O. (2024). *Lightning-Fast Convective Outlooks: Predicting Severe Convective Environments with Global AI-based Weather Models*. <https://doi.org/10.48550/arXiv.2406.09474>
- Feng, R., Balling, N., Grana, D., Dramsch, J. S., & Hansen, T. M. (2021). Bayesian convolutional neural networks for seismic facies classification. *IEEE Transactions on Geoscience and Remote Sensing, 59(10)*, 8933–8940. <https://doi.org/10.1109/TGRS.2020.3049012>
- Flora, M. L., & Potvin, C. (2024). WoFSCast: A machine learning model for predicting thunderstorms at watch-to-warning scales. *Authorea Preprints*. <https://doi.org/10.22541/essoar.172574503.30734251/v1>
- Ghobadi, F., & Kang, D. (2022). Multi-step ahead probabilistic forecasting of daily streamflow using Bayesian deep learning: A multiple case study. *Water, 14(22)*, 3672. <https://doi.org/10.3390/w14223672>
- Ghude, S. D., Bhat, G. S., Prabhakaran, T., Jenamani, R. K., Chate, D. M., Safai, P. D., Karipot, A. K., Konwar, M., Pithani, P., Sinha, V., Rao, P. S. P., Dixit, S. A., Tiwari, S., Todekar, K., Varpe, S., Srivastava, A. K., Bisht, D. S., Murugavel, P., Ali, K., ... Rajeevan, M.

- (2017). Winter Fog Experiment Over the Indo-Gangetic Plains of India. *Current Science*, 112(04), 767. <https://doi.org/10.18520/cs/v112/i04/767-784>
- Gong, W., Gupta, H. V., Yang, D., Sricharan, K., & Hero, A. O. (2013). Estimating epistemic and aleatory uncertainties during hydrologic modeling: An information theoretic approach. *Water Resources Research*, 49(4), 2253–2273. <https://doi.org/10.1002/wrcr.20161>
- Gorelick, N., Hancher, M., Dixon, M., Ilyushchenko, S., Thau, D., & Moore, R. (2017). Google Earth Engine: Planetary-scale geospatial analysis for everyone. *Remote Sensing of Environment*, 202, 18–27. <https://doi.org/10.1016/j.rse.2017.06.031>
- Gultepe, I., Tardif, R., Michaelides, S. C., Cermak, J., Bott, A., Bendix, J., Müller, M. D., Pagowski, M., Hansen, B., Ellrod, G., Jacobs, W., Toth, G., & Cober, S. G. (2007). Fog research: A review of past achievements and future perspectives. *Pure and Applied Geophysics*, 164(6–7), 1121–1159. <https://doi.org/10.1007/s00024-007-0211-x>
- Guo, B., Wang, Y., Zhang, X., Che, H., Zhong, J., Chu, Y., & Cheng, L. (2020). Temporal and spatial variations of haze and fog and the characteristics of PM2.5 during heavy pollution episodes in China from 2013 to 2018. *Atmospheric Pollution Research*, 11(10), 1847–1856. <https://doi.org/10.1016/j.apr.2020.07.019>
- Guo, C., Pleiss, G., Sun, Y., & Weinberger, K. Q. (2017). On calibration of modern neural networks. *34th International Conference on Machine Learning, ICML 2017*, 3, 2130–2143. <http://arxiv.org/abs/1706.04599>
- Guo, X., Wan, J., Liu, S., Xu, M., Sheng, H., & Yasir, M. (2021). A scSE-LinkNet deep learning model for daytime sea fog detection. *Remote Sensing*, 13(24), 5163. <https://doi.org/10.3390/rs13245163>
- Gupta, A., & Govindaraju, R. S. (2023). Uncertainty quantification in watershed hydrology: Which method to use? *Journal of Hydrology*, 616, 128749. <https://doi.org/10.1016/j.jhydrol.2022.128749>
- Han, J. H., Suh, M. S., Yu, H. Y., & Roh, N. Y. (2020). Development of fog detection algorithm using GK2A/AMI and ground data. *Remote Sensing*, 12(19), 3181. <https://doi.org/10.3390/rs12193181>
- Hingmire, D., Vellore, R. K., Krishnan, R., Ashtikar, N. V., Singh, B. B., Sabade, S., & Madhura, R. K. (2019). Widespread fog over the Indo-Gangetic Plains and possible links to boreal winter teleconnections. *Climate Dynamics*, 52, 5477–5506. <https://doi.org/10.1007/s00382-018-4458-y>
- Hofmann, H., Wickham, H., & Kafadar, K. (2017). Letter-value plots: Boxplots for large data. *Journal of Computational and Graphical Statistics*, 26(3), 469–477. <https://doi.org/10.1080/10618600.2017.1305277>
- Hollmann, R., Merchant, C. J., Saunders, R., Downy, C., Buchwitz, M., Cazenave, A., Chuvieco, E., Defourny, P., de Leeuw, G., Forsberg, R., Holzer-Popp, T., Paul, F., Sandven, S., Sathyendranath, S., van Roozendael, M., & Wagner, W. (2013). The ESA climate change initiative: Satellite data records for essential climate variables. *Bulletin of the American Meteorological Society*, 94(10), 1541–1552.

<https://doi.org/10.1175/BAMS-D-11-00254.1>

- Hron, J., Matthews, A. G. de G., & Ghahramani, Z. (2017). Variational Gaussian dropout is not Bayesian. *arXiv preprint arXiv:1711.02989*. <https://doi.org/10.48550/arXiv.1711.02989>
- Huang, Y., Wu, M., Guo, J., Zhang, C., & Xu, M. (2022). A correlation context-driven method for sea fog detection in meteorological satellite imagery. *IEEE Geoscience and Remote Sensing Letters*, 19, 1–5. <https://doi.org/10.1109/LGRS.2021.3095731>
- Huffman, G. J., Adler, R. F., Bolvin, D. T., Gu, G., Nelkin, E. J., Bowman, K. P., Hong, Y., Stocker, E. F., & Wolff, D. B. (2007). The TRMM multisatellite precipitation analysis (TMPA): Quasi-global, multiyear, combined-sensor precipitation estimates at fine scales. *Journal of Hydrometeorology*, 8(1), 38–55. <https://doi.org/10.1175/JHM560.1>
- Hüllermeier, E., & Waegeman, W. (2021). Aleatoric and epistemic uncertainty in machine learning: an introduction to concepts and methods. *Machine Learning*, 110(3), 457–506. <https://doi.org/10.1007/s10994-021-05946-3>
- Hůnová, I., Brabec, M., Malý, M., & Valeriánová, A. (2020). Long-term trends in fog occurrence in the Czech Republic, Central Europe. *Science of the Total Environment*, 711. <https://doi.org/10.1016/j.scitotenv.2019.135018>
- Hunt, G. E. (1973). Radiative properties of terrestrial clouds at visible and infra-red thermal window wavelengths. *Quarterly Journal of the Royal Meteorological Society*, 99(420), 346–369. <https://doi.org/10.1002/qj.49709942013>
- Hunt, K.M.R., Baudouin, J.-P., Turner, A.G., Dimri, A.P., Jeelani, G., Chattopadhyay, R., Cannon, F., Arulalan, T., Shekhar, M.S., Sabin, T.P., Palazzi, E., 2025. Western disturbances and climate variability: a review of recent developments. *Weather and Climate Dynamics*, 6, 43–112. <https://doi.org/10.5194/wcd-6-43-2025>
- IEM. (2021). *Iowa Mesonet: Iowa Environmental Mesonet (IEM) ASOS AWOS-METAR Data*, Iowa State University. <https://mesonet.agron.iastate.edu/request/download.phtml> (accessed 2025-01-17).
- ISRO. (2015). *INSAT-3D Algorithm Theoretical Basis Definition (ATBD) document* (Issue May). https://mosdac.gov.in/data/doc/INSAT_3D_ATBD_MAY_2015.pdf (accessed 2021-01-28).
- Izett, J. G., van de Wiel, B. J. H., Baas, P., van Hooft, J. A., & Schulte, R. B. (2019). Dutch fog: On the observed spatio-temporal variability of fog in the Netherlands. *Quarterly Journal of the Royal Meteorological Society*, 145(723), 2817–2834. <https://doi.org/10.1002/qj.3597>
- Jahani, B., Karalus, S., Zech, T., Fuchs, J., Cermak, J., & Zara, M. (2023). Machine-learning algorithm for 24h detection of fog and low stratus over Europe based on MSG-SEVIRI infrared bands. *EGU General Assembly 2023*. <https://doi.org/https://doi.org/10.5194/egusphere-egu23-13515>
- Jayakumar, A., Gordon, H., Francis, T., Hill, A. A., Mohandas, S., Sandeepan, B. S., Mitra, A. K., & Beig, G. (2021). Delhi Model with chemistry and aerosol framework (DM-Chem)

- for high-resolution fog forecasting. *Quarterly Journal of the Royal Meteorological Society*, 147(741), 3957–3978. <https://doi.org/10.1002/qj.4163>
- Jenamani, R. K. (2012). Micro-climatic study and trend analysis of fog characteristics at IGI airport New Delhi using hourly data (1981–2005). *MAUSAM*, 63(2), 203–218. <https://doi.org/10.54302/mausam.v63i2.1391>
- Jindal, P., Shukla, M. V., Mitra, D., & Hari, M. (2023). A New Methodology for Detection of Fog over the Indian Region using INSAT-3D Data. *Journal of the Indian Society of Remote Sensing*, 51(1), 1–7. <https://doi.org/10.1007/s12524-022-01587-8>
- Kaseke, K. F., & Wang, L. (2018). Fog and Dew as Potable Water Resources: Maximizing Harvesting Potential and Water Quality Concerns. *GeoHealth*, 2(10), 327–332. <https://doi.org/10.1029/2018GH000171>
- Kendall, A., & Gal, Y. (2017). What uncertainties do we need in Bayesian deep learning for computer vision? *31st Conference on Neural Information Processing Systems (NIPS 2017)*, 30. <https://doi.org/10.48550/arxiv.1703.04977>
- Khodadadi-Hassankiadeh, N., Rad, E. H., Koohestani, H. S., & Kouchakinejad-Eramsadati, L. (2020). The Pattern of Road Accidents in Fog and the Related Factors in North of Iran in 2014–2018. *Research Square preprint* <https://doi.org/10.21203/rs.3.rs-73501/v1>
- Kim, B. Y., Cha, J. W., Chang, K. H., & Lee, C. (2021). Visibility prediction over South Korea based on random forest. *Atmosphere*, 12(5), 552. <https://doi.org/10.3390/atmos12050552>
- Kim, J., Cha, J., Kim, T., Lee, H., Yu, H. Y., & Suh, M. S. (2024). VisNet: Spatiotemporal self-attention-based U-Net with multitask learning for joint visibility and fog occurrence forecasting. *Engineering Applications of Artificial Intelligence*, 136. <https://doi.org/10.1016/j.engappai.2024.108967>
- Kim, Y., Ryu, H.-S., & Hong, S. (2023). Data-to-data translation-based nowcasting of specific sea fog using geostationary weather satellite observation. *Atmospheric Research*, 290, 106792. <https://doi.org/10.1016/j.atmosres.2023.106792>
- Klemm, O., Schemenauer, R. S., Lummerich, A., Cereceda, P., Marzol, V., Corell, D., Van Heerden, J., Reinhard, D., Gherezghiher, T., Olivier, J., Osses, P., Sarsour, J., Frost, E., Estrela, M. J., Valiente, J. A., & Fessehaye, G. M. (2012). Fog as a fresh-water resource: Overview and perspectives. *Ambio*, 41(3), 221–234. <https://doi.org/10.1007/s13280-012-0247-8>
- Kneis, D., Chatterjee, C., & Singh, R. (2014). Evaluation of TRMM rainfall estimates over a large Indian river basin (Mahanadi). *Hydrology and Earth System Sciences*, 18(7), 2493–2502. <https://doi.org/10.5194/hess-18-2493-2014>
- Krzysztof, S., Andrey, K., Matthias, & Hadrien, B. (2019). *Suntime- Simple sunset and sunrise time calculation Python library*. <https://pypi.org/project/suntime/> (accessed 2025-01-17).
- Kulkarni, R., Jenamani, R. K., Pithani, P., Konwar, M., Nigam, N., & Ghude, S. D. (2019). Loss to Aviation Economy Due to Winter Fog in New Delhi during the Winter of 2011–2016. *Atmosphere*, 10(4), 198. <https://doi.org/10.3390/atmos10040198>

- Kumari, S., Verma, N., Lakhani, A., & Kumari, K. M. (2021). Severe haze events in the Indo-Gangetic Plain during post-monsoon: Synergetic effect of synoptic meteorology and crop residue burning emission. *Science of the Total Environment*, 768, 145479. <https://doi.org/10.1016/j.scitotenv.2021.145479>
- Kurth, T., Subramanian, S., Harrington, P., Pathak, J., Mardani, M., Hall, D., Miele, A., Kashinath, K., & Anandkumar, A. (2023). FourCastNet: Accelerating Global High-Resolution Weather Forecasting Using Adaptive Fourier Neural Operators. *Proceedings of the Platform for Advanced Scientific Computing Conference*, 1–11. <https://doi.org/10.1145/3592979.3593412>
- Kutty, S. G., Agnihotri, G., Dimri, A. P., & Gultepe, I. (2019). Fog occurrence and associated meteorological factors over Kempegowda International Airport, India. *Pure and Applied Geophysics*, 176(5), 2179–2190. <https://doi.org/10.1007/s00024-018-1882-1>
- Kutty, S. G., Dimri, A. P., & Gultepe, I. (2020). Climatic trends in fog occurrence over the Indo-Gangetic plains. *International Journal of Climatology*, 40(4), 2048–2061. <https://doi.org/10.1002/joc.6317>
- Kwon, Y., Won, J. H., Kim, B. J., & Paik, M. C. (2020). Uncertainty quantification using Bayesian neural networks in classification: Application to biomedical image segmentation. *Computational Statistics & Data Analysis*, 142, 106816. <https://doi.org/10.1016/j.csda.2019.106816>
- Lakra, K., & Avishek, K. (2022). A review on factors influencing fog formation, classification, forecasting, detection and impacts. *Rendiconti Lincei. Scienze Fisiche e Naturali*, 33(2), 319–353. <https://doi.org/10.1007/s12210-022-01060-1>
- Lam, R., Sanchez-Gonzalez, A., Willson, M., Wirnsberger, P., Fortunato, M., Alet, F., Ravuri, S., Ewalds, T., Eaton-Rosen, Z., Hu, W., Merose, A., Hoyer, S., Holland, G., Vinyals, O., Stott, J., Pritzel, A., Mohamed, S., & Battaglia, P. (2023). Learning skillful medium-range global weather forecasting. *Science*, 382(6677), 1416–1421. <https://doi.org/10.1126/science.adl2336>
- Lee, E., Kim, J.-H., Heo, K.-Y., & Cho, Y.-K. (2021). Advection Fog over the Eastern Yellow Sea: WRF Simulation and Its Verification by Satellite and In Situ Observations. *Remote Sensing*, 13(8), 1480. <https://doi.org/10.3390/rs13081480>
- Li, B., Wang, L., Kaseke, K. F., Vogt, R., Li, L., & K. Seely, M. (2018). The impact of fog on soil moisture dynamics in the Namib Desert. *Advances in Water Resources*, 113, 23–29. <https://doi.org/10.1016/j.advwatres.2018.01.004>
- Li, D., Marshall, L., Liang, Z., & Sharma, A. (2022). Hydrologic multi-model ensemble predictions using variational Bayesian deep learning. *Journal of Hydrology*, 604(June 2021), 127221. <https://doi.org/10.1016/j.jhydrol.2021.127221>
- Long, Q., Wu, B., Mi, X., Liu, S., Fei, X., & Ju, T. (2021). Review on Parameterization Schemes of Visibility in Fog and Brief Discussion of Applications Performance. *Atmosphere*, 12(12), 1666. <https://doi.org/10.3390/atmos12121666>

- Lu, D., Konapala, G., Painter, S. L., Kao, S. C., & Gangrade, S. (2021). Streamflow simulation in data-scarce basins using Bayesian and physics-informed machine learning models. *Journal of Hydrometeorology*, 22(6), 1421–1438. <https://doi.org/10.1175/JHM-D-20-0082.1>
- Lundberg, S., & Lee, S.-I. (2017). A Unified Approach to Interpreting Model Predictions. *arXiv preprint arXiv:1705.07874*. <http://arxiv.org/abs/1705.07874>
- Ma, H., Li, Y., Wu, X., Feng, H., Ran, Y., Jiang, B., & Wang, W. (2022). A large-region fog detection algorithm at dawn and dusk for high-frequency Himawari-8 satellite data. *International Journal of Remote Sensing*, 43(7), 2620–2637. <https://doi.org/10.1080/01431161.2022.2065895>
- Ma, H., Liu, Z., Jiang, K., Jiang, B., Feng, H., & Hu, S. (2023). A novel ST-ViBe algorithm for satellite fog detection at dawn and dusk. *Remote Sensing*, 15(9), 2331. <https://doi.org/10.3390/rs15092331>
- Ma, N., Zhao, C. S., Chen, J., Xu, W. Y., Yan, P., & Zhou, X. J. (2014). A novel method for distinguishing fog and haze based on PM2.5, visibility, and relative humidity. *Science China Earth Sciences*, 57(9), 2156–2164. <https://doi.org/10.1007/s11430-014-4885-5>
- Mahdavi, S., Amani, M., Bullock, T., & Beale, S. (2021). A probability-based daytime algorithm for sea fog detection using GOES-16 imagery. *IEEE Journal of Selected Topics in Applied Earth Observations and Remote Sensing*, 14, 1363–1373. <https://doi.org/10.1109/JSTARS.2020.3036815>
- Meisner, D. (2014). *Understanding letter value plot and boxenplot*. Towards Data Science. <https://towardsdatascience.com/letter-value-plot-the-easy-to-understand-boxplot-for-large-datasets-12d6c1279c97> (accessed 2025-01-17).
- Menut, L., Mailler, S., Dupont, J.-C., Haeffelin, M., & Elias, T. (2014). Predictability of the Meteorological Conditions Favourable to Radiative Fog Formation During the 2011 ParisFog Campaign. *Boundary-Layer Meteorology*, 150(2), 277–297. <https://doi.org/10.1007/s10546-013-9875-1>
- Miao, K., Han, T., Yao, Y., Lu, H., Chen, P., Wang, B., & Zhang, J. (2020). Application of LSTM for short term fog forecasting based on meteorological elements. *Neurocomputing*, 408, 285–291. <https://doi.org/10.1016/j.neucom.2019.12.129>
- Mishra, A., Ahmadisharaf, E., Benham, B. L., Gallagher, D. L., Reckhow, K. H., & Smith, E. P. (2019). Two-Phase Monte Carlo simulation for partitioning the effects of epistemic and aleatory uncertainty in TMDL modeling. *Journal of Hydrologic Engineering*, 24(1), 1–14. [https://doi.org/10.1061/\(asce\)he.1943-5584.0001731](https://doi.org/10.1061/(asce)he.1943-5584.0001731)
- Mohan, K. N., Shinde, U., Bhatnagar, M. K., Paligan, A. A., Sivakumar, G., Krishnamurthy, R., Shubha, V., & Mali, R. R. (2015). Performance study of Drishti transmissometer at CAT III B airport. *MAUSAM*, 66(4), 713–718. <https://doi.org/10.54302/mausam.v66i4.578>
- Mohan, T. S., Temimi, M., Ajayamohan, R. S., Nelli, N. R., Fonseca, R., Weston, M., & Valappil, V. (2020). On the investigation of the typology of fog events in an arid

- environment and the link with climate patterns. *Monthly Weather Review*, 148(8), 3181–3202. <https://doi.org/10.1175/MWR-D-20-0073.1>
- NCMWF. (2025). *National Centre for Medium Range Weather Forecasting, Ministry of Earth Sciences, Government of India*. National Centre for Medium Range Weather Forecasting Ministry of Earth Sciences Government of India. <https://www.ncmrfc.gov.in/> (accessed 2025-01-17).
- NOAA, 2025. NOAA GraphCast Global Forecast System (GFS) (EXPERIMENTAL) [WWW Document]. URL <https://noaa-nws-graphcastgfs-pds.s3.amazonaws.com/index.html> (accessed 1.13.25).
- Nearing, G. S., Tian, Y., Gupta, H. V., Clark, M. P., Harrison, K. W., & Weijs, S. V. (2016). A philosophical basis for hydrological uncertainty. *Hydrological Sciences Journal*, 61(9), 1666–1678. <https://doi.org/10.1080/02626667.2016.1183009>
- Nolde, J., & Lasowski, R. (2021). Comparing a deterministic and a Bayesian classification neural network for chest diseases in radiological images. In H. Kaiserslautern (Ed.), *The Upper-Rhine Artificial Intelligence Symposium* (Issue October, pp. 53–60). University of Applied Sciences. <https://doi.org/10.48550/arXiv.2112.05657>
- Pahlavan, R., Moradi, M., Tajbakhsh, S., Azadi, M., Rahnama, M., 2021. Fog probabilistic forecasting using an ensemble prediction system at six airports in Iran for 10 fog events. *Meteorological Applications*, 28. <https://doi.org/10.1002/met.2033>
- Pappenberger, F., & Beven, K. J. (2006). Ignorance is bliss: Or seven reasons not to use uncertainty analysis. *Water Resources Research*, 42(5). <https://doi.org/10.1029/2005WR004820>
- Parde, A. N., Ghude, S. D., Dhangar, N. G., Lonkar, P., Wagh, S., Govardhan, G., Biswas, M., & Jenamani, R. K. (2022). Operational Probabilistic Fog Prediction Based on Ensemble Forecast System: A Decision Support System for Fog. *Atmosphere*, 13(10). <https://doi.org/10.3390/atmos13101608>
- Pauli, E., Andersen, H., Bendix, J., Cermak, J., & Egli, S. (2020). Determinants of fog and low stratus occurrence in continental central Europe – a quantitative satellite-based evaluation. *Journal of Hydrology*, 591, 125451. <https://doi.org/10.1016/J.JHYDROL.2020.125451>
- Pauli, E., Cermak, J., & Andersen, H. (2022). A satellite-based climatology of fog and low stratus formation and dissipation times in central Europe. *Quarterly Journal of the Royal Meteorological Society*, 148(744), 1439–1454. <https://doi.org/10.1002/qj.4272>
- Payra, S., & Mohan, M. (2014). Multirule based diagnostic approach for the fog predictions using WRF modelling tool. *Advances in Meteorology*, 2014. <https://doi.org/10.1155/2014/456065>
- Pithani, P., Ghude, S. D., Jenamani, R. K., Biswas, M., Naidu, C. V., Debnath, S., Kulkarni, R., Dhangar, N. G., Jena, C., Hazra, A., Phani, R., Mukhopadhyay, P., Prabhakaran, T., Nanjundiah, R. S., & Rajeevan, M. (2020). Real-Time forecast of dense fog events over Delhi: The performance of the WRF model during the WiFEX field campaign. *Weather and Forecasting*, 35(2), 739–756. <https://doi.org/10.1175/WAF-D-19-0104.1>

- Pithani, P., Ghude, S. D., Prabhakaran, T., Karipot, A., Hazra, A., Kulkarni, R., Chowdhuri, S., Resmi, E. A., Konwar, M., Murugavel, P., Safai, P. D., Chate, D. M., Tiwari, Y., Jenamani, R. K., & Rajeevan, M. (2019). WRF model sensitivity to choice of PBL and microphysics parameterization for an advection fog event at Barkachha, rural site in the Indo-Gangetic basin, India. *Theoretical and Applied Climatology*, 136(3–4), 1099–1113. <https://doi.org/10.1007/s00704-018-2530-5>
- Price, I., Sanchez-Gonzalez, A., Alet, F., Andersson, T. R., El-Kadi, A., Masters, D., Ewalds, T., Stott, J., Mohamed, S., Battaglia, P., Lam, R., & Willson, M. (2024). Probabilistic weather forecasting with machine learning. *Nature*. <https://doi.org/10.1038/s41586-024-08252-9>
- Pu, Z., Chachere, C. N., Hoch, S. W., Pardyjak, E., & Gultepe, I. (2016). Numerical Prediction of Cold Season Fog Events over Complex Terrain: the Performance of the WRF Model During MATERHORN-Fog and Early Evaluation. *Pure and Applied Geophysics*, 173(9), 3165–3186. <https://doi.org/10.1007/s00024-016-1375-z>
- Qiao, N., Wang, L., Marais, E., & Li, F. (2022). Fog Detection and Estimation Using CALIPSO Lidar Observations. *Geophysical Research Letters*, 49(24). <https://doi.org/10.1029/2022GL101375>
- Qiao, N., Zhang, L., Huang, C., Jiao, W., Maggs-Kölling, G., Marais, E., & Wang, L. (2020). Satellite Observed Positive Impacts of Fog on Vegetation. *Geophysical Research Letters*, 47(12), 1–8. <https://doi.org/10.1029/2020GL088428>
- Quan, J., Zhang, Q., He, H., Liu, J., Huang, M., & Jin, H. (2011). Analysis of the formation of fog and haze in North China Plain (NCP). *Atmospheric Chemistry and Physics*, 11(15), 8205–8214. <https://doi.org/10.5194/acp-11-8205-2011>
- Ram, K., Sarin, M. M., Sudheer, A. K., & Rengarajan, R. (2012). Carbonaceous and secondary inorganic aerosols during wintertime fog and haze over urban sites in the Indo-Gangetic plain. *Aerosol and Air Quality Research*, 12(3), 355–366. <https://doi.org/10.4209/aaqr.2011.07.0105>
- Rasp, S., Hoyer, S., Merose, A., Langmore, I., Battaglia, P., Russell, T., Sanchez-Gonzalez, A., Yang, V., Carver, R., Agrawal, S., Chantry, M., Ben Bouallegue, Z., Dueben, P., Bromberg, C., Sisk, J., Barrington, L., Bell, A., & Sha, F. (2024). WeatherBench 2: A Benchmark for the Next Generation of Data-Driven Global Weather Models. *Journal of Advances in Modeling Earth Systems*, 16(6). <https://doi.org/10.1029/2023MS004019>
- Rasul, K., Ashok, A., Williams, A. R., Ghonia, H., Bhagwatkar, R., Khorasani, A., Bayazi, M. J. D., Adamopoulos, G., Riachi, R., Hassen, N., Biloš, M., Garg, S., Schneider, A., Chapados, N., Drouin, A., Zantedeschi, V., Nevmyvaka, Y., & Rish, I. (2023). *Lag-Llama: Towards Foundation Models for Probabilistic Time Series Forecasting*. <http://arxiv.org/abs/2310.08278>
- Román-Cascón, C., Steeneveld, G.J., Yagüe, C., Sastre, M., Arrillaga, J.A., Maqueda, G., 2016. Forecasting radiation fog at climatologically contrasting sites: evaluation of statistical methods and WRF. *Quarterly Journal of the Royal Meteorological Society*, 142, 1048–1063. <https://doi.org/10.1002/qj.2708>

- Roux, B., Potts, R., Siems, S., & Manton, M. (2021). Towards a better understanding of fog at Perth Airport. *Journal of Hydrology*, 600, 126516.
<https://doi.org/10.1016/j.jhydrol.2021.126516>
- Sadeghi Tabas, S., & Samadi, S. (2022). Variational Bayesian dropout with a Gaussian prior for recurrent neural networks application in rainfall-runoff modeling. *Environmental Research Letters*, 17(6). <https://doi.org/10.1088/1748-9326/ac7247>
- Sawaisarge, G. K., Khare, P., Shirke, C. Y., Deepakumar, S., & Narkhde, N. M. (2014). Study of winter fog over Indian subcontinent : Climatological perspectives. *MAUSAM*, 65(1), 19–28. <https://doi.org/10.54302/mausam.v65i1.858>
- Sharma, S., Bajaj, K., Deshpande, P., Bhattacharya, A., & Tripathi, S. (2024). Short-Term Fog Forecasting using Meteorological Observations at Airports in North India. *Proceedings of the 7th Joint International Conference on Data Science & Management of Data (11th ACM IKDD CODS and 29th COMAD)*, 307–315.
<https://doi.org/10.1145/3632410.3632449>
- Shi, J., Jin, B., Han, J., & Narasimhan, G. (2024). *CoDiCast: Conditional Diffusion Model for Weather Prediction with Uncertainty Quantification*. <http://arxiv.org/abs/2409.05975>
- Shin, D., & Kim, J. H. (2018). A new application of unsupervised learning to nighttime sea fog detection. *Asia-Pacific Journal of Atmospheric Sciences*, 54(4), 527–544.
<https://doi.org/10.1007/S13143-018-0050-Y>
- Shrestha, S., Moore, G. A., & Peel, M. C. (2018). Trends in winter fog events in the Terai region of Nepal. *Agricultural and Forest Meteorology*, 259, 118–130.
<https://doi.org/10.1016/j.agrformet.2018.04.018>
- Shukla, A., Ojha, C., Singh, R., Pal, L., & Fu, D. (2019). Evaluation of TRMM precipitation dataset over Himalayan catchment: The Upper Ganga Basin, India. *Water*, 11(3), 613.
<https://doi.org/10.3390/w11030613>
- Silvestro, D., & Andermann, T. (2020). Prior choice affects ability of Bayesian neural networks to identify unknowns. *arXiv preprint arXiv:2005.04987*.
<https://doi.org/https://doi.org/10.48550/arXiv.2005.04987>
- Singh, A., George, J. P., & Iyengar, G. R. (2018). Prediction of fog/visibility over India using NWP Model. *Journal of Earth System Science*, 127(2), 26.
<https://doi.org/10.1007/s12040-018-0927-2>
- Singh, A., Maheskumar, R.S., Iyengar, G.R., (2022). A Diagnostic Method for Fog Forecasting Using Numerical Weather Prediction (NWP) Model Outputs. *Journal of Atmospheric Science Research*, 5, 10–19. <https://doi.org/10.30564/jasr.v5i4.5068>
- Singh, P., Kumar, S., Ashrit, R., & Rai, S. (2025). Wind speed and power forecasting: Evaluating NCUM-G model performance. *Journal of Earth System Science*, 134(1), 20.
<https://doi.org/10.1007/s12040-024-02485-y>
- Singh, S. K. (2017). Road Traffic Accidents in India: Issues and Challenges. *Transportation Research Procedia*, 25, 4708–4719. <https://doi.org/10.1016/j.trpro.2017.05.484>

- Smith, D. K. E., Dorling, S. R., Renfrew, I. A., Ross, A. N., & Poku, C. (2023). Fog trends in India: Relationships to fog type and western disturbances. *International Journal of Climatology*, 43(2), 818–836. <https://doi.org/10.1002/joc.7832>
- Smith, D. K. E., Reka, S., Dorling, S. R., Ross, A. N., Renfrew, I. A., Jayakumar, A., Anurose, T. J., Parde, A. N., Ghude, S. D., & Rumbold, H. (2024). Forecasts of fog events in northern India dramatically improve when weather prediction models include irrigation effects. *Communications Earth & Environment*, 5(1), 141. <https://doi.org/10.1038/s43247-024-01314-w>
- Srivastava, S. K., Sharma, A. R., & Sachdeva, K. (2016). A ground observation based climatology of winter fog: Study over the Indo-Gangetic Plains, India. *International Journal of Environmental and Ecological Engineering*, 10(7), 742–753. <https://doi.org/doi.org/10.5281/zenodo.1125465>
- Srivastava, S. K., Sharma, A. R., & Sachdeva, K. (2017). An observation-based climatology and forecasts of winter fog in Ghaziabad, India. *Weather*, 72(1), 16–22. <https://doi.org/10.1002/wea.2743>
- Stevens, S. E. (2019). Trends in instrument flight rules (IFR) conditions at major airports in the United States. *Journal of Applied Meteorology and Climatology*, 58(3), 615–620. <https://doi.org/10.1175/JAMC-D-18-0301.1>
- Steeneveld, G.J., Ronda, R.J., Holtslag, A.A.M., 2015. The challenge of forecasting the onset and development of radiation fog using mesoscale atmospheric models. *Boundary Layer Meteorol* 154, 265–289. <https://doi.org/10.1007/s10546-014-9973-8>
- Suri, D., Dutta, P., Xue, F., Azevedo, I., & Jain, R. (2024). Operational Wind Speed Forecasts for Chile's Electric Power Sector Using a Hybrid ML Model. *arXiv preprint arXiv:2409.09263*. <http://arxiv.org/abs/2409.09263>
- Syed, F. S., Körnich, H., & Tjernström, M. (2012). On the fog variability over south Asia. *Climate Dynamics*, 39(12), 2993–3005. <https://doi.org/10.1007/s00382-012-1414-0>
- Tang, Y. M., Capon, R., Forbes, R., & Clark, P. (2009). Fog prediction using a very high resolution numerical weather prediction model forced with a single profile. *Meteorological Applications*, 16(2), 129–141. <https://doi.org/10.1002/met.88>
- Tang, Y., Yang, P., Zhou, Z., & Zhao, X. (2022). Daytime sea fog detection based on a two-stage neural network. *Remote Sensing*, 14(21), 5570. <https://doi.org/10.3390/rs14215570>
- Tardif, R., & Rasmussen, R. M. (2007). Event-based climatology and typology of fog in the New York City region. *Journal of Applied Meteorology and Climatology*, 46(8), 1141–1168. <https://doi.org/10.1175/JAM2516.1>
- Terry, J. P., Jia, G., Boldi, R., & Khan, S. (2018). The Delhi ‘gas chamber’: smog, air pollution and the health emergency of November 2017. *Weather*, 73(11), 348–352. <https://doi.org/10.1002/wea.3242>
- TIE. (2022, January 14). *Dense fog envelops Delhi, likely for next two days*. The Indian Express. <https://www.newindianexpress.com/cities/delhi/2022/Jan/14/dense-fog-envelops-delhi-likely-for-next-two-days-2406733.html> (accessed 2025-01-17).

- TOI. (2022, January 15). *Delhi: Dense fog delays 50 flights at IGI*. The Times of India. <https://timesofindia.indiatimes.com/city/delhi/dense-fog-delays-50-flights-at-igi-but-none-diverted/articleshow/88905685.cms> (accessed 2025-01-17).
- Veljović, K., & Vujović, D. (2019). Climatology of fog occurrence over a wide flat area in Serbia based on visibility observations. *International Journal of Climatology*, 39(3), 1331–1344. <https://doi.org/10.1002/joc.5883>
- Velde, I. R. Van Der, Steeneveld, G. J., Schreur, B. G. J. W., & Holtslag, A. A. M. (2010). Modeling and forecasting the onset and duration of severe radiation fog under frost conditions. *Monthly Weather Review*, 138(11), 4237–4253. <https://doi.org/10.1175/2010MWR3427.1>
- Vié, M.-S., Zufferey, N., & Leus, R. (2022). Aircraft landing planning under uncertain conditions. *Journal of Scheduling*, 25(2), 203–228. <https://doi.org/10.1007/s10951-022-00730-0>
- Vogel, D. (2023). *European Guidance Material on All Weather Operations at Aerodromes, Sixth Edition*. <https://www.icao.int/EURNAT/EUR%20and%20NAT%20Documents/EUR%20Documents/EUR%20Documents/013%20-%20EUR%20Guidance%20Material%20on%20AWO%20at%20Aerodromes/EUR%20Document%200013,%206th%20Edition,%20November%202023.pdf?form=MG0AV3> (accessed 2025-01-17).
- Wagh, S., Kulkarni, R., Lonkar, P., Parde, A. N., Dhangar, N. G., Govardhan, G., Sajjan, V., Debnath, S., Gultepe, I., Rajeevan, M., & Ghude, S. D. (2023). Development of visibility equation based on fog microphysical observations and its verification using the WRF model. *Modeling Earth Systems and Environment*, 9(1), 195–211. <https://doi.org/10.1007/s40808-022-01492-6>
- Wang, L., Kaseke, K. F., Ravi, S., Jiao, W., Mushi, R., Shuuya, T., & Maggs-Kölling, G. (2019). Convergent vegetation fog and dew water use in the Namib Desert. *Ecohydrology*, 12(7). <https://doi.org/10.1002/eco.2130>
- Waskom, M. (2021). Seaborn: Statistical data visualization. *Journal of Open Source Software*, 6(60), 3021. <https://doi.org/10.21105/joss.03021>
- Weisstein, Eric W (2010). "Markov Chain." From MathWorld--A Wolfram Web Resource. <https://mathworld.wolfram.com/MarkovChain.html> (accessed 2025-01-17).
- Weston, M. J., Piketh, S. J., Burnet, F., Broccardo, S., Denjean, C., Bourrianne, T., & Formenti, P. (2022). Sensitivity analysis of an aerosol-aware microphysics scheme in Weather Research and Forecasting (WRF) during case studies of fog in Namibia. *Atmospheric Chemistry and Physics*, 22(15), 10221–10245. <https://doi.org/10.5194/acp-22-10221-2022>
- Wilks, D. S. *Statistical Methods in the Atmospheric Sciences*. Vol. 100. Amsterdam: Elsevier Science, 2006.

- Wilson, A. G., & Izmailov, P. (2020). Bayesian deep learning and a probabilistic perspective of generalization. *Proceedings of the 34th International Conference on Neural Information Processing Systems*. <https://doi.org/10.48550/arXiv.2002.08791>
- WMO. (2011). *Manual on codes, international codes. Technical Report, World Meteorological Organization, Geneva Switzerland.*
- WMO. (2017). Guidelines on the calculation of climate normals. *WMO-No. 1203, 1203*, 18.
- Yan, Z., Lu, X., Wu, L., Liu, F., Qiu, R., Cui, Y., & Ma, X. (2024). Evaluation of precipitation forecasting base on GraphCast over mainland China. *Research Square preprint*. <https://doi.org/10.21203/rs.3.rs-4645037/v1>
- Yang, J.-H., Yoo, J.-M., Choi, Y.-S., Wu, D., & Jeong, J.-H. (2019). Probability index of low stratus and fog at dawn using dual geostationary satellite observations from COMS and FY-2D near the Korean peninsula. *Remote Sensing*, 11(11), 1283. <https://doi.org/10.3390/rs11111283>
- Yang, Y., Ge, B., Chen, X., Yang, W., Wang, Z., Chen, H., Xu, D., Wang, J., Tan, Q., & Wang, Z. (2021). Impact of water vapor content on visibility: Fog-haze conversion and its implications to pollution control. *Atmospheric Research*, 256, 105565. <https://doi.org/10.1016/j.atmosres.2021.105565>
- Yi, L., Li, M., Liu, S., Shi, X., Li, K. F., & Bendix, J. (2023). Detection of dawn sea fog/low stratus using geostationary satellite imagery. *Remote Sensing of Environment*, 294, 113622. <https://doi.org/10.1016/J.RSE.2023.113622>
- Yoo, J. M., Choo, G. H., Lee, K. H., Wu, D. L., Yang, J. H., Park, J. D., Choi, Y. S., Shin, D. Bin, Jeong, J. H., & Yoo, J. M. (2018). Improved detection of low stratus and fog at dawn from dual geostationary (COMS and FY-2D) satellites. *Remote Sensing of Environment*, 211, 292–306. <https://doi.org/10.1016/j.rse.2018.04.019>
- Zheng, Z., Chen, L., Sun, N., Jin, Y., & Wang, Y. (2024). Pollution, hazards, and health inequalities: a longitudinal exploration of the impact of PM2.5 on depression among rural older adults with different incomes in China. *Humanities and Social Sciences Communications*, 11(1). <https://doi.org/10.1057/s41599-024-04233-5>
- Zhou, B., Du, J., Ferrier, B. S., Mcqueen, J. T., Ferrier, B., Mcqueen, J., & Dimego, G. (2007). Numerical forecast of fog-Central solutions. In Preprints, *18th Conf. on Numerical Weather Prediction, Park City, UT, American Meteorological Society A* (Vol. 8). <https://www.researchgate.net/publication/228652122>
- Zou, J., Sun, J., Li, T., Han, X., Xiang, Z., & Sha, J. (2021). Observed interactions among haze, fog and atmospheric boundary layer during a haze-fog episode in the Yangtze River Delta region, Eastern China. *Aerosol and Air Quality Research*, 21(4), 200354. <https://doi.org/10.4209/aaqr.2020.06.0354>

APPENDIX

A 1 Appendix 1

Visibility-based fog classification as per Indian Railways is provided in Table A1.1, whereas Table A1.2 presents minimum visibility requirements as per International Civil Aviation Organization (ICAO) (Vogel, 2023).

Table A1.1 Visibility-based fog classification as per Indian Railways.

Type of fog	Visibility range (m)
Mild	100 to 300
Dense	5 to 100
Extreme	0 to 5

Table A1.2 Minimum visibility requirements for different airport categories as per ICAO.

Type of airport	Minimum visibility requirement (m)
CAT I	550
CAT II	350
CAT IIIa	200
CAT IIIb	50
CAT IIIc	0

A 2 Appendix 2

A 2.1 Data availability and interpolation

The datasets used in Chapter 2 are summarised in Table A2.1. Winter seasons having a minimum of 85% data availability at an hourly scale are selected. However, the available data may not be the same for all hours of the day. Hence, it is necessary to analyse the distribution of missing data. The histogram showing the distribution of data is shown in Figure A2.1. The distribution of gaps in the available data shows that gaps corresponding to 30 min and 1.5 hours have the highest frequency, followed by a 2.5-hour gap. Significant variation in visibility is not expected for small gaps like 30 mins or 1.5 hours.

Meteorological observations usually have a diurnal cycle, and this natural behaviour may be lost if bigger gaps are imputed. On the other hand, if only small gaps are imputed, then the discontinuous time-series of meteorological observations will be obtained, which will not be suitable for identifying fog events. Hence, there is a trade-off in imputation. Figure A2.1 enables us to choose an appropriate window size for imputation.

The missing values of short gaps (< 3 hours) are imputed using linear interpolation. A sensitivity analysis is carried out to check the applicability of linear interpolation. In this sensitivity analysis, firstly, artificial missing values of various durations were created, and then these were filled with linear interpolation. RMSE is calculated based on original and imputed values. Table A2.1 shows that the RMSE is less than 300 m in all the cases suggesting that while linear interpolation may affect visibility-based classification up to some extent, it is unlikely to affect fog event identification. A comparison of the interpolated and non-interpolated visibility data shows that the number of fog events eligible for calculating fog statistics reduces by 73% if carried out without interpolation.

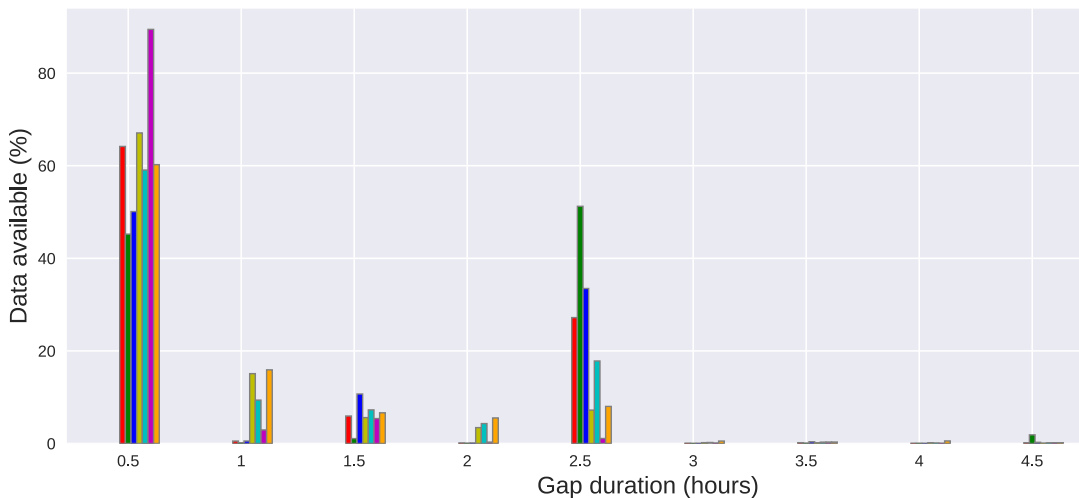


Figure A2.1 Distribution of missing values in METAR dataset

Table A2.1 Summary of the datasets used in the characterization of fog in IGP.

Dataset	Purpose	Temporal resolution	Spatial resolution	Duration
METAR	<i>In situ</i> meteorological observations	Up to half-hour	-	1991-2020
TRMM-TMPA	Rainfall estimation	3 hours	0.25°	1998-2020
ESA-CCI	Land-cover map	-	350 m	2013

A 2.2 Sensitivity of M-of-N events

After interpolation, the relatively complete observation time-series is ready to extract the isolated fog events using the M-of-N algorithm. The fog characterisation is entirely based on event analysis, and fog events are identified using the M-of-N algorithm. This subjectivity in the M-of-N algorithm may lead to a different number of identified fog events. To study the effect of different choices of M and N values on the number of identified events, a sensitivity analysis is carried out by trying different values of M and N over a range and corresponding changes in the number of identified events. Suppose the change in the number of events is insignificant. In that case, the current fog event identification is said to be robust, and any value of M and N in the given range can be used to extract the fog events for further analysis. On the other hand, if there is a drastic change in the number of identified events because of changes in the count of events

identifies by the M-of-N algorithm, the values of M and N need to be decided carefully considering the target fog event size.

The sensitivity analysis is carried out with a range from 1 to 4 and N from 1 to 9. The results for Delhi city are shown in as an example. A decrease in the identified fog events is found with an increase in M and N values. The larger M and N values tend to identify the larger events as well as merge small events, and hence they are less in number. Table A2.2 shows the maximum and the minimum number of events identified and percentage variation with respect to the target event in the case of Delhi. The variation in the number of identified events is within 7.5%, which is a small quantity that shows the robust behaviour of the M-of-N algorithm. Further analysis is carried out with M = 3 and N = 5.

Table A2.2. Sensitivity of the number of events identified by the M-of-N algorithm.
(Design event is the smallest event to be identified in the characterisation study)

M	N	No. of events	% change
1	3	511	+0.59
3	5	508	Design event
4	8	470	-7.48

A 2.3 Boxen-plots and violin-plots

A 2.3.1 Boxen-plots

Boxen-plots (letter valued plots), i.e., advancement of box-plots, overcomes the problems associated with the traditional box-plots, viz., visualisation of samples beyond quartiles, inaccurate visualisation of outliers. The linear relationship between sample size and the number of outliers may not show the distribution of samples in the tail region. Boxen-plots do not stop after the quartiles, the remaining data spaces are divided further, and more boxes are added to the plot. They are recursively defined order statistics with specific depths using Equation A 2.1 and Equation A 2.2.

$$d_1 = \frac{(1 + n)}{2} \quad (A 2.1)$$

$$d_i = \frac{(1 + \text{floor}(d_{i-1}))}{2} \quad (A2.2)$$

d_1 divides the data into two halves; hence it is nothing but the median of all samples. Each subsequent step divides the remaining samples into halves (Table A2.3). This recursive process can be stopped using the stopping criteria based on confidence interval or limiting the number of boxes. The concept of boxen-plots is intuitive and easily understandable Fig. A2.2. It shows the distribution of data in a better way; hence, it is used in this chapter. The example and figure elaborated here are taken from a blog by Meisner, (2014).

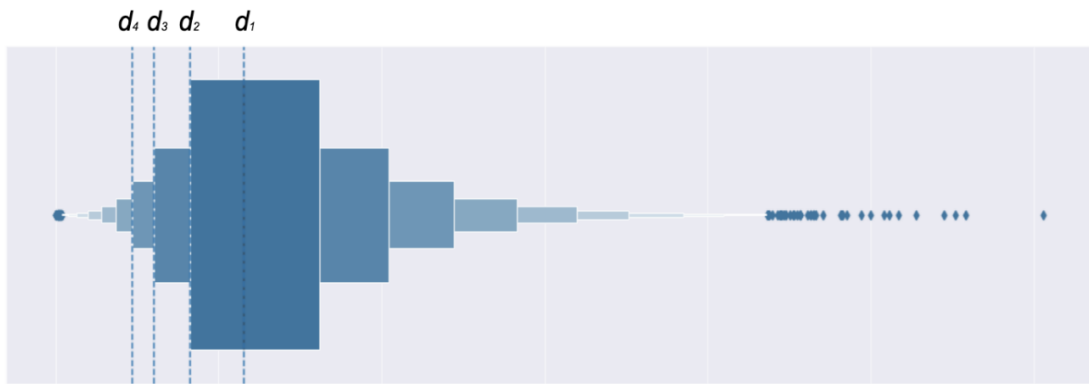


Fig. A2.2. Boxen-plot using quantiles (d_1, d_2, d_3, d_4) as per Table A 2.4 and and Eq. A 2.2.

Table A2.3 Boxen-plot quantiles as per Equation A2.1 and Equation A2.2

d_i	Number of samples	$d_i/n \%$
$d_0 = n$	10000	100%
d_1	5000.5	50%
d_2	2500.5	25%
d_3	1250.5	12.5%
d_4	625.5	6.25%

A 2.3.2 Violin-plots

Violin plots are a combination of box-plots and kernel density plots. Along with the usual features of box-plots (viz., median, interquartile range), violin-plots also show the entire distribution of data. Such plots are excellent for showing multimodal data. In this chapter, a variation of the standard violin-plot is utilized from the Python library Seaborn (Waskom, 2021). The different components of a violin-plot are shown in Fig. A2.3.

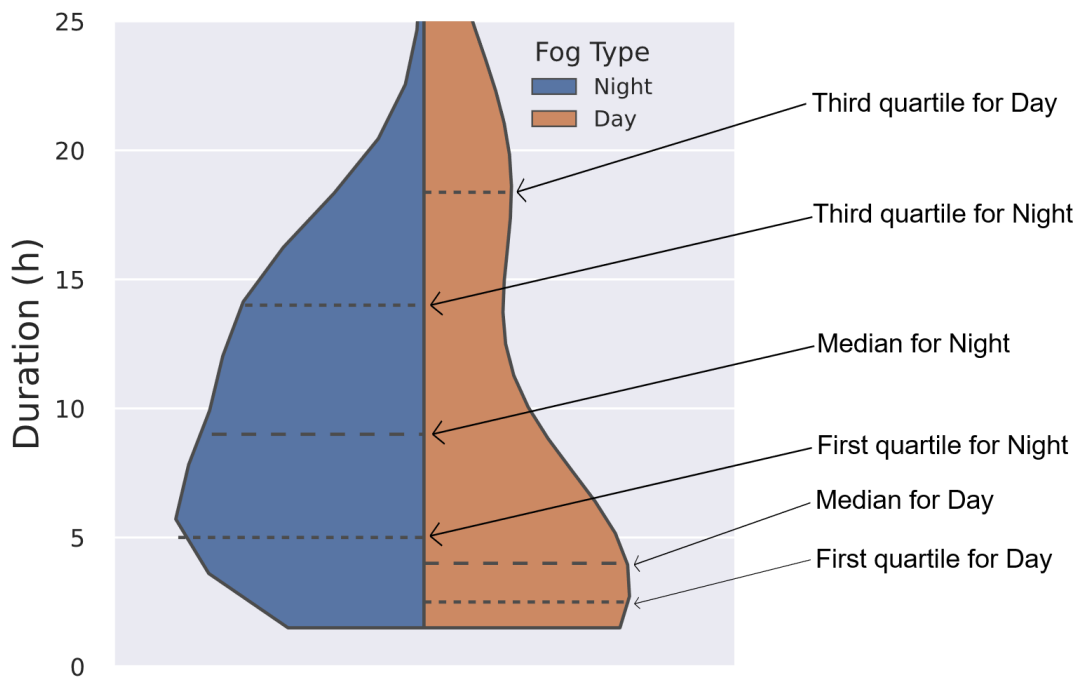


Fig. A2.3. Components violin-plot used in this study

A 2.4 Correlations of inter-seasonal distribution of fog events

Table A2.4. Correlation among seasonal values of fog characteristics at different cities. Bold font corresponds to statistically significant positive correlations at 95% confidence interval; statistically significant negative correlations are shown in bold italic. The time-series used for calculating correlations are shown in Fig. 2.11.

	Kolkata	Gaya	Patna	Lucknow	Jaipur	Delhi	Amritsar	Mean
Number of fog events	Kolkata	1.00						
	Gaya	-0.02	1.00					
	Patna	0.00	0.79	1.00				
	Lucknow	0.17	0.60	0.30	1.00			
	Jaipur	0.12	0.57	0.51	0.39	1.00		
	Delhi	-0.09	0.17	-0.01	0.41	0.20	1.00	
	Amritsar	-0.19	0.51	0.15	0.44	0.17	0.32	1.00
	Mean	0.50	0.81	0.51	0.85	0.54	0.51	0.53
								1.00

	Kolkata	Gaya	Patna	Lucknow	Jaipur	Delhi	Amritsar	Mean
Average duration of fog events	Kolkata	1.00						
	Gaya	-0.25	1.00					
	Patna	0.18	0.28	1.00				
	Lucknow	-0.06	0.52	-0.11	1.00			
	Jaipur	-0.36	0.27	-0.25	0.25	1.00		
	Delhi	-0.04	0.53	-0.10	0.84	0.61	1.00	
	Amritsar	0.07	0.64	-0.14	0.79	0.65	0.91	1.00
	Mean	0.29	0.73	0.35	0.79	0.47	0.89	0.88
								1.00

	Kolkata	Gaya	Patna	Lucknow	Jaipur	Delhi	Amritsar	Mean
Seasonal fog hours	Kolkata	1.00						
	Gaya	0.01	1.00					
	Patna	0.14	0.28	1.00				
	Lucknow	-0.15	0.70	0.44	1.00			
	Jaipur	0.01	0.55	0.36	0.42	1.00		
	Delhi	-0.53	0.58	0.19	0.55	0.57	1.00	
	Amritsar	-0.49	0.67	0.39	0.77	0.52	0.57	1.00
	Mean	0.26	0.87	0.61	0.89	0.62	0.69	0.74
								1.00

A 3 Appendix 3

A 3.1 Comparison of INSAT-3D Fog with *in situ* visibility observations

The objective of this Appendix section is to assess the agreement between in situ (METAR) visibility observations with the INSAT-3D Fog product. The same seven cities used in Chapter 2 are used for this evaluation. Data from 2013 to 2021 during the winter season are used.

For each INSAT-3D Fog image, the binary pixel values (denoting fog/no-fog) are extracted for the 7 cities. Thus, a binary time-series of satellite fog observations is obtained for each city. Additionally, a time-series of visibility observations for each city is obtained from in situ observations. A threshold on visibility observation is applied to convert the *in situ* visibility observations into fog observations- "fog" if visibility is less than the threshold, else "no-fog". A threshold that maximizes the agreement between these two datasets becomes the optimum threshold and is termed as equivalent visibility.

Once the time-series of fog is generated from in situ observations, a comparison can be made between *in situ* and satellite fog observations. Then the equivalence between these two fog observations for a particular threshold value is evaluated using different performance evaluation metrics viz., Critical Success Index (CSI), Cohen's Kappa Coefficient (κ). The same procedure is repeated for different thresholds to find the optimum threshold value maximizing the κ , a metric that is robust to chance agreement. The observations of all the cities together are also evaluated to find the combined equivalence of in situ and remote sensing satellite fog observations. The results are provided in Table A3.1.

Table A3.1 Comparison of *in situ* (METAR) fog observations with INSAT-3D Fog.

City	No. of Obs. (in 1000s)	Fog in INSAT-3D Fog (%)	Maximum Overall Accuracy (OA)	Maximum Cohen's Kappa (κ)	Optimum Threshold (m)	Overall Accuracy for 1 km Threshold	Cohen's Kappa (κ) for 1 km Threshold
Kolkata	19	1.4	0.99	0.15	998	0.97	0.15
Gaya	13	2.9	0.97	0.28	322	0.89	0.19
Patna	15	4.4	0.96	0.30	901	0.88	0.26
Lucknow	17	5.3	0.95	0.38	161	0.77	0.18
Jaipur	16	0.48	0.99	0.17	402	0.98	0.07
Delhi	19	4.0	0.96	0.27	161	0.63	0.087
Amritsar	18	5.4	0.93	0.31	322	0.80	0.21
Combine	120	3.4	0.96	0.30	316	0.84	0.18

The combined threshold thus identified across all cities is 306 m and corresponding κ of 0.3 and CSI of 0.19. However, the threshold varies from 161 m to 998 m across different cities. The relatively low values of the performance metrics and high variability in optimum threshold suggest a scope for development of an improved satellite fog detection method.

A 3.2 Additional details of the Bayesian neural network

The details of BNN model (in TensorFlow terminology) are provided in Table A3..

Table A3.2. Implementation details of the BNN model (in TensorFlow terminology)

Layer type	Output dimensions	Number of parameters (weights)	Description
Input layer	512×220	0	Input to Dense layer 1
Dense layer 1	512×120	26520	Fully connected layer 1 with deterministic weights
Dense layer 2	512×32	3872	Fully connected layer 2 with deterministic weights
Dense variational layer	512×1	594	Fully connected layer with weights modelled as normal distribution
Independent Bernoulli Layer	512×1	0	Calculates negative log likelihood loss with Bernoulli distribution

The model development is carried out in Google Colaboratory interface. Real-time implementation of the code is carried out in Intel Xeon E7 v4 (with 64 GB RAM) computer. For a trained model, the time taken to generate a fog detection image (with uncertainties) is less than 10 minutes.

A 3.3 Effect of hyperparameters on model performance

Deciding on model architecture and setting the hyperparameters depends on 3 metrics, viz. – high mean CSI, lesser ECE, and variation in uncertainty scatterplot (e.g., Figure 3.3). By changing the hyperparameters, one or more metrics may change. In the next sub-sections, optimum hyperparameters are decided for maximizing the model performance on validation dataset. It should be noted that these hyperparameters are data dependent, and hence, they may change for fog detection using a different satellite, study area or duration of the study. Currently, data from 6 winter seasons and 16 cities are used for model training. The results of sensitivity analysis of some selected parameters are given in the following subsections.

A 3.3.1 Number of past observations as input

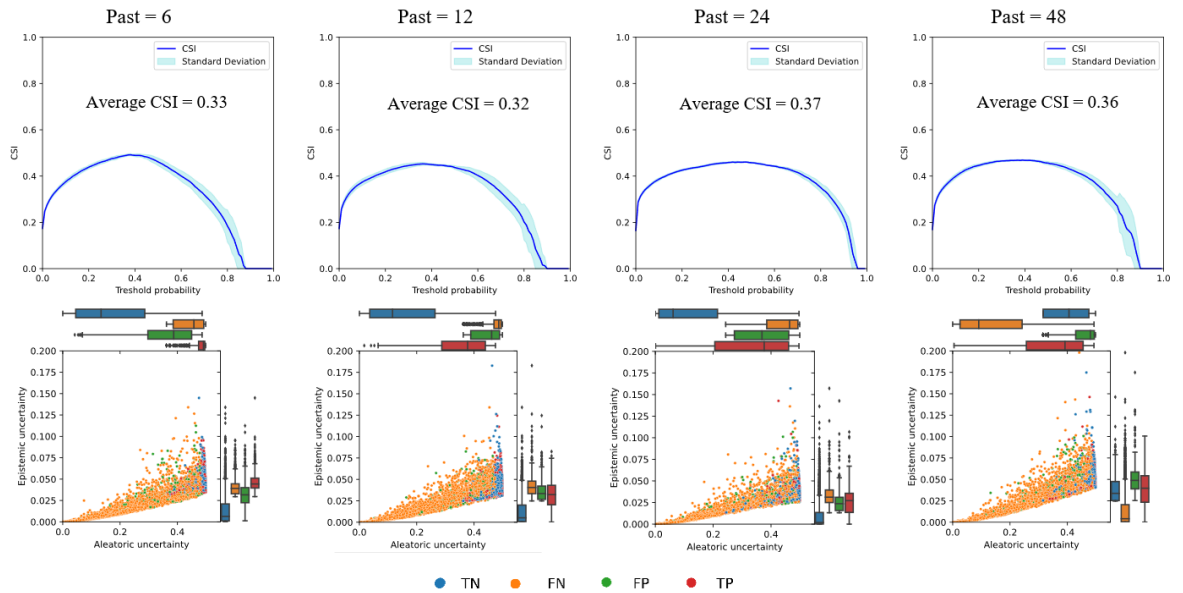


Figure. A3.1. Effect of the number of past observations as input to model on CSI (top row) and uncertainties (bottom row).

As the number of past observations decreases, the shape of CSI curve varies Figure. A3.1. The maximum value of CSI does not show a huge difference. However, maximum CSI may not be

the best metric of performance as it belongs to a particular threshold probability. The mean CSI over all thresholds (area under CSI curve) generally increases as the number of past observations increases. Additionally, the maximum probability produced by the model increases (the CSI curve becomes 0 after a particular threshold probability in Figure. A3.1) with the number of past observations. Whenever the model is not able to generate fog with higher probability, the corresponding aleatoric uncertainty also increases as aleatoric uncertainty is based on the probability value generated by the model. The model with $\text{past} = 24$ is finalized as it gives the best results.

A 3.3.2 Effect of KL-weight

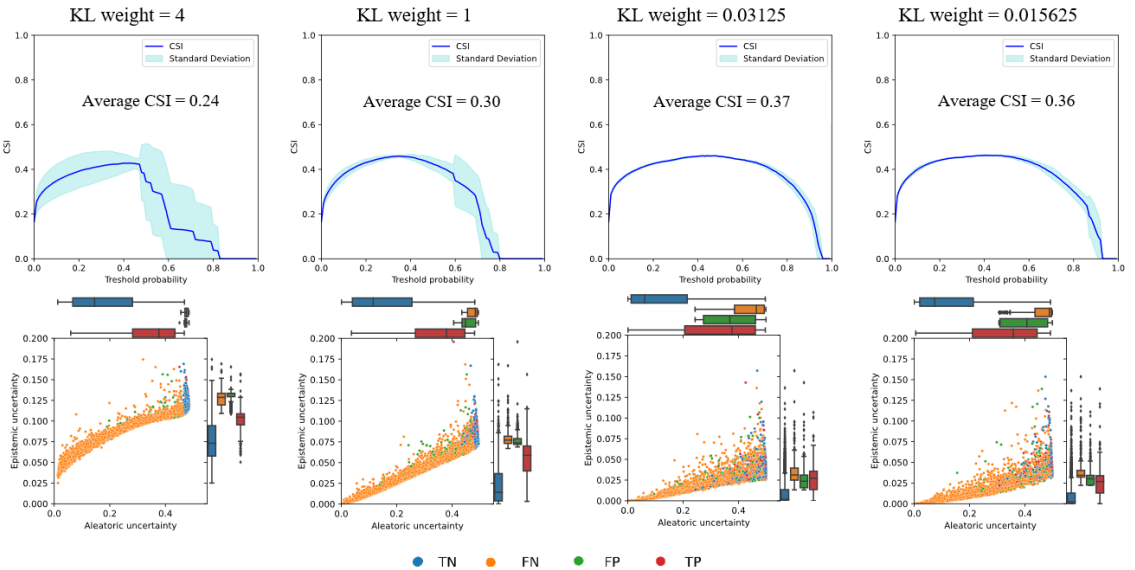


Fig. A3.2. Effect of KL-weight hyperparameter on CSI (top row) and uncertainties (bottom row).

Fig. A3.2 shows that the maximum CSI for the various KL-weights is nearly the same. However, by decreasing the KL-weight hyperparameter, the average CSI over all thresholds increases, which indicates that model performance increases. Higher KL-weight generates outputs closely aligned to the prior distribution, whereas lower values of KL-weight focus more on the accurate reconstruction of the training data. As the KL-weight parameter decreases, the contribution of KLD in the ELBO decreases, and the contribution of the likelihood part increases. Since the likelihood is data dependent, it indicates that while learning the posterior distribution of weights, more emphasis is given to learning the patterns of the input data as

compared to the prior distribution. Moreover, importantly the epistemic uncertainty band narrows down as KL-weight decreases, which shows that the model is more confident about the detections. Meanwhile, with a decrease in KL-weight, the mean epistemic uncertainty decreases but the spread of uncertainty increases (Fig. A3.2). In other words, the higher value of KL-weight generates similar values of epistemic uncertainty irrespective of the input data. However, epistemic uncertainty is intended to show higher values for out-of-distribution input data. This is also another reason to choose the lower value of KL-weight. For the proposed model, the KL-weight is set as 0.03125.

A 3.3.3 Effect of prior distribution

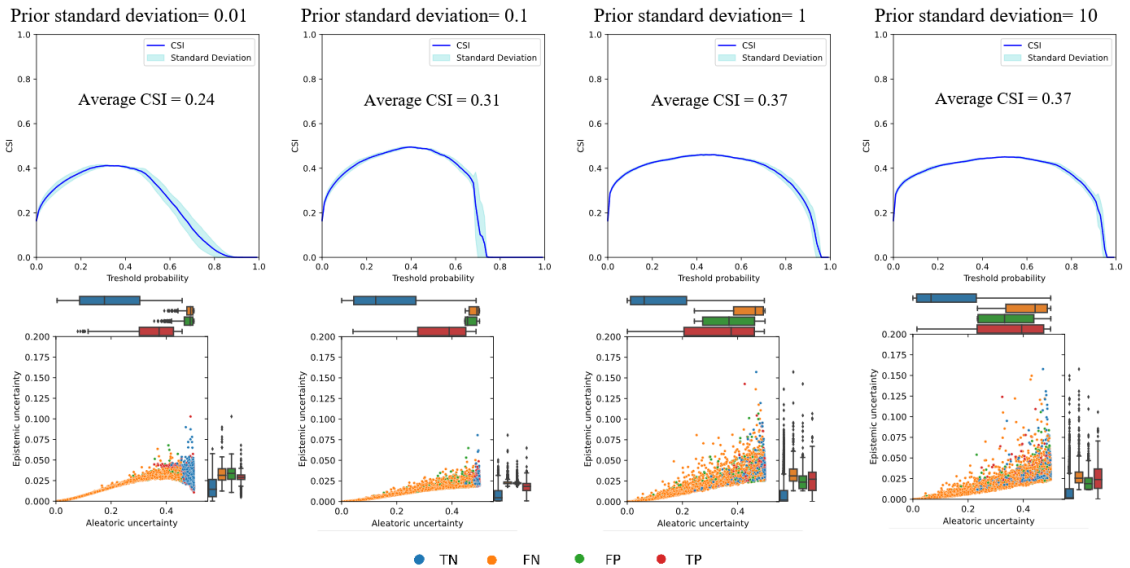


Fig. A3.3. Effect of standard deviation of prior distribution on CSI (top row) and uncertainties (bottom row).

Here, the model is trained and tested for different values of standard deviation of prior distribution with zero mean. The rest of the hyperparameters are kept constant. The behaviour observed for the different values of the standard deviation of the prior distribution (Fig. A3.3) is opposite to the behaviour of varying KL-weight (Fig. A3.2). As the standard deviation of the prior distribution increases, the performance of the model first increases and then becomes nearly constant. These results are consistent with applications of BNNs in other domains (Feng et al., 2021; Wilson & Izmailov, 2020). The priors with higher standard deviations, also known as weakly informed priors, do not over-regularize the weights, and hence the model is able to

learn the weights from input data. On the other hand, strongly informed priors that heavily regularize the data are used in data-scarce problems, and there is already some knowledge about the expected values of weights (e.g., pre-trained neural networks). In the case of fog detection, being a novel application, such prior idea about the weights is not available currently, hence it is better to use weekly informed prior. The effect of decreasing the KL-weights on model performance can be achieved by increasing the standard deviation of the prior distribution. For the extremely high values of KL-weight and extremely low values of the standard deviation of the prior distribution, the model is not able to converge, and hence the model is unable to generate any results.

A 3.3.4 Effect of training proportion

Apart from the above hyperparameters, the effect of size of training dataset is also demonstrated in Fig. A3.4. The subsets of the training dataset by taking some percentage (e.g., 25%, 50%) of the training dataset. The maximum CSI and mean CSI increases with increasing the training dataset along with the maximum generated probability. Moreover, both uncertainties decrease with increasing the training dataset size.

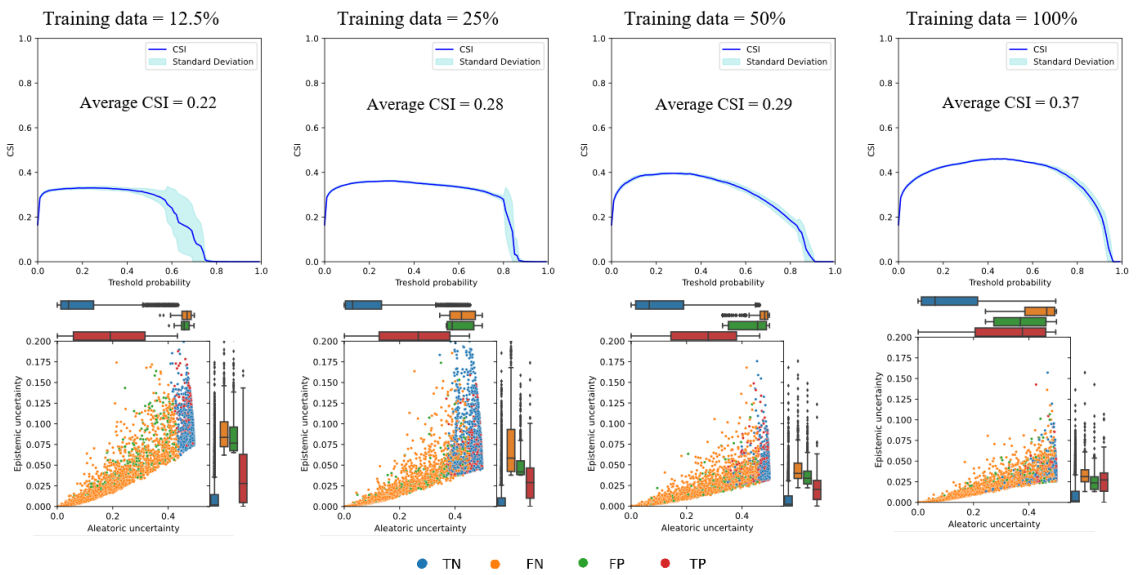


Fig. A3.4. Effect of size of training dataset (as a percentage of original training dataset) on CSI (top row) and uncertainties (bottom row).

A 3.4 Combined effect of prior distribution and KL-weight hyperparameter

In Appendix A 3.3.3, it is mentioned that the effects of changing KL-weight can be observed by changing the standard deviation of the prior distribution. This statement is demonstrated as follows: One-dimensional data (reference data) is generated with normal distribution with some known mean and standard deviation. Now, a variational inference model is developed to model the mean of the reference data. Here, the learned mean and ELBO are noted down for the corresponding standard deviation of the prior distribution (the mean of the prior is always kept at 0), and KL-weight parameter. This procedure is repeated with different combinations of prior standard deviation and KL-weight parameter values. The contour plot is generated, showing ELBO values for different prior standard deviation and KL-weight parameter values (Fig. A3.5). The same contour colour shows that the same ELBO is obtained for different combinations of prior standard deviation and KL-weight. In the neural network, the weights are trained based on the ELBO value only. Hence, out of these 2 hyperparameters, only one can be optimized, keeping the other parameter constant. In this chapter, the standard deviation of the prior distribution is kept at 1, while KL-weight is optimized.

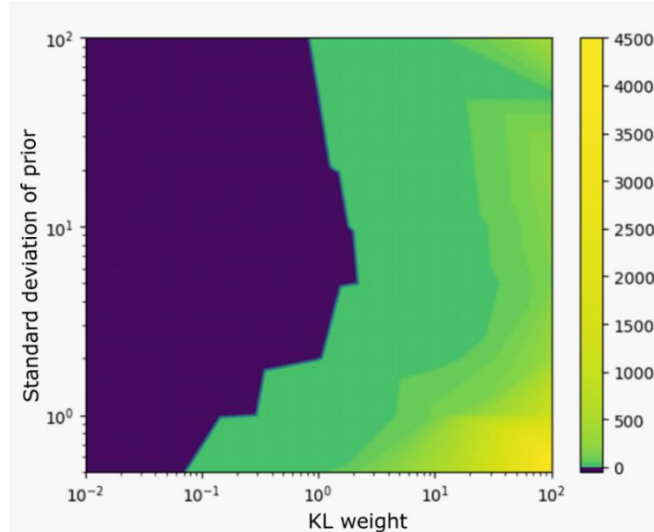


Fig. A3.5. Contour plot showing the ELBO values as colour for different KL-weights and different standard deviations of the prior distributions.

A 3.5 Fog detection images generated by proposed model

The sample results for the fog detection and corresponding uncertainty evaluation are presented below Figures Fig. A3.6 and Fig. A3.7. The whole INSAT-3D imagery is given as input to provide the fog detection map.

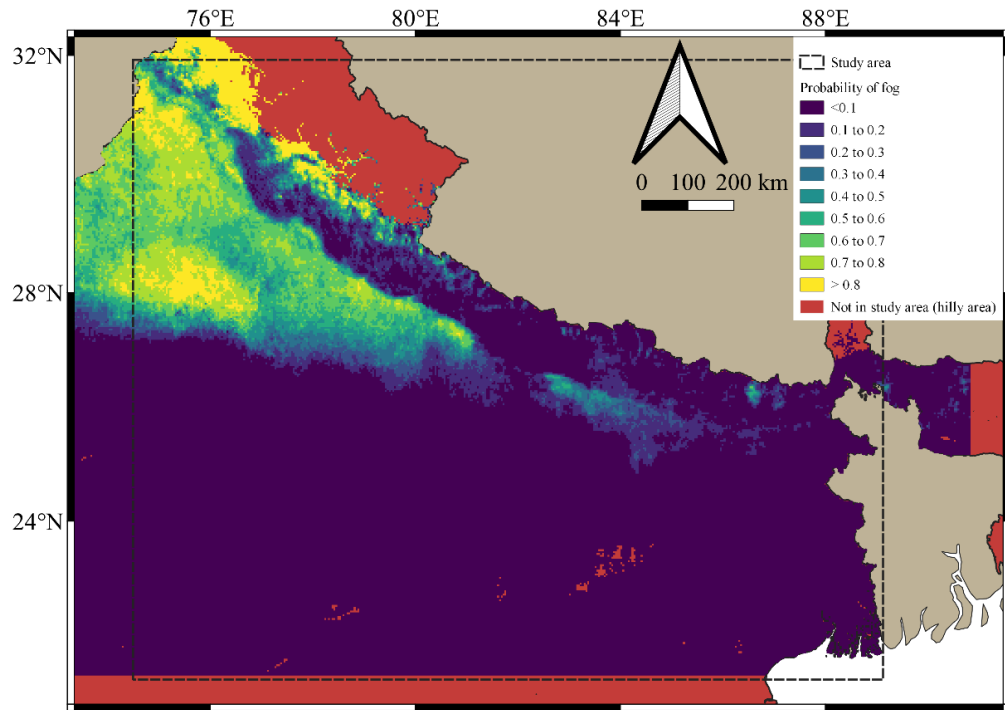


Fig. A3.6. Image showing the probability of fog detected by the proposed BNN model for 26th December 2019 at 02:00 am (IST).

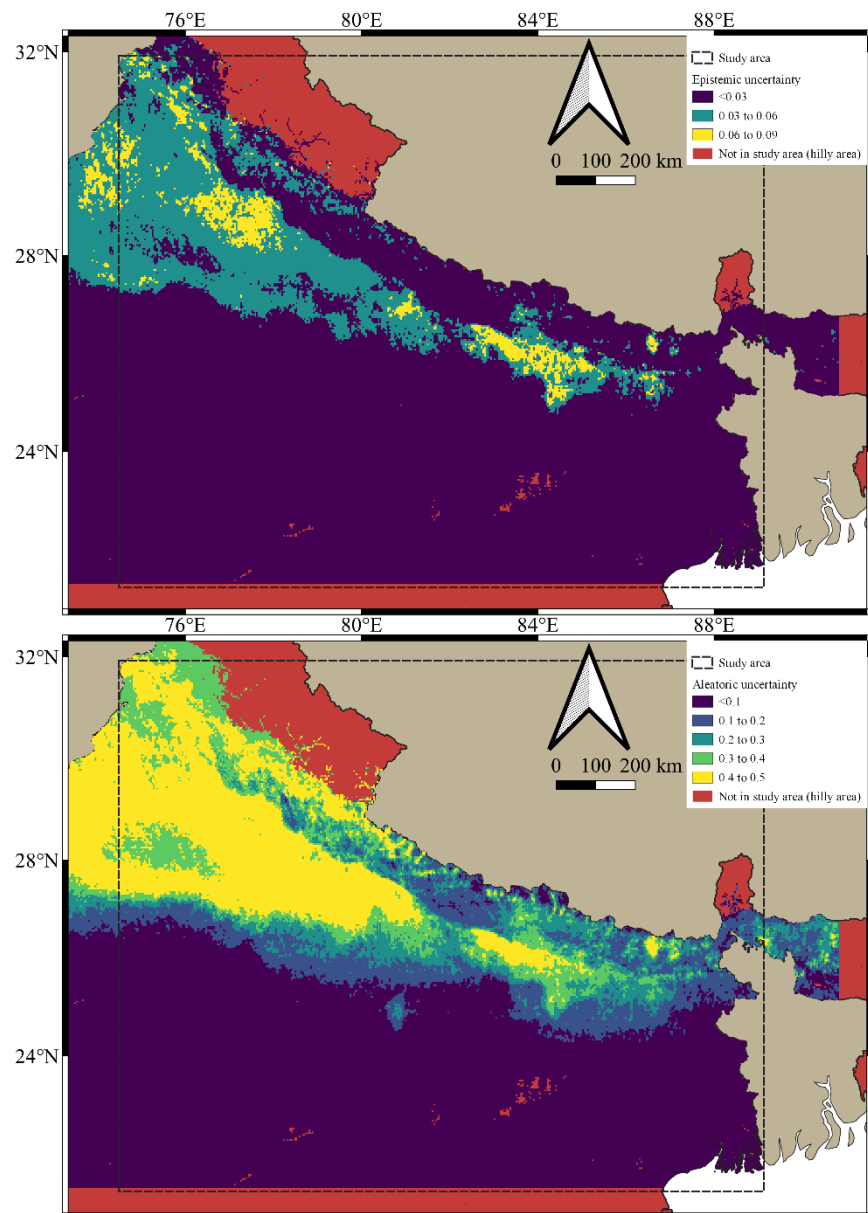


Fig. A3.7. Epistemic (top) and aleatoric (bottom) uncertainties for fog detection by the proposed BNN model for 26th December 2019 at 02:00 am.

A 4 Appendix 4

A 4.1 Past studies related to fog forecasting

Table A4.1. Comparison of past fog forecasting studies (The majority studies are spatial fog forecasting with few examples of point forecasts)

Sharma et al. (2024)	Kim et al. (2024)	Authors
IGP (Lucknow), India (2000-2021)	South Korea (72 sites) (2017-2019)	Region (city) and Study Period
Various AI-ML models (point scale)	Random forest models (point scale)	Model (spatial resolution in km)
3 h	12 h	Lead Time
30 minutes	1 h	Frequency
Binary and regression (1000 m)	Binary and regression (1000 m)	Type of forecast (thresholds)
PoD: 0.82, FAR: 0.24, CSI: 0.65, OA: 0.89	PoD: 0.76, FAR: 0.27, CSI: 0.27, OA: 0.99	Performance metrics
<i>In-situ</i> obs.	<i>In-situ</i> obs.	Validated By
Site-specific, statistical model. Thus, cannot be used for spatial fog forecasting	Site-specific, statistical model. Thus, cannot be used for spatial fog forecasting	Remarks

Weston et al. (2022)	Singh et al. (2022)	Parde et al. (2022)
Namibia (September 2017)	IGP (Amritsar, Delhi, and Lucknow) (Dec - Feb 2016-2019)	IGP (Delhi), India (2020-2022)
WRF- Aerosol-Aware Microphysics) (3)	National Centre for Medium Range Weather Forecasting Unified Model -. NCUMD) (17)	WRF- Ensemble Forecast System (4)
48 h	18–30 h	24 h
10 m	6 h	1 h
Binary (visibility < 1km)	Multiclass (fog: 200 m – 1 km and dense fog: \leq 200 m.)	Probabilistic binary (visibility <500 m)
Comparison of actual and forecasted fog properties (viz., droplet number concentration, liquid water content (LWC).	OA: 0.54, POD: 0.60, CSI:0.58, FAR 0.04 for Delhi	PoD: 0.95, FAR: 0.43, CSI: 0.55
Observations from fog monitor, radiosondes, and SEVIRI satellite	<i>In-situ</i> obs.	<i>In-situ</i> obs., INSAT-3DR satellite fog
Dynamic aerosol-aware microphysics improved forecast of LWC and droplet size.	Better performance for Delhi, but not in Lucknow, probably due to local variability.	Overprediction of fog reported in some cases

Aditi and Ashrit (2021)	Dimitrova et al. (2021)	Pahlavan et al. (2021)
Delhi, India (Dec 2017- Feb 2018)	Coastal Atlantic Canada (4 cities) (Sep 1-Oct 8, 2018)	Iran (Arak, Ardebil, Rasht) (January and December 2015)
NCUM-G (17), Delhi Model (DM) (0.33)	WRF-, Nested (Domains with resolution of 27 km, 9 km, 3 km and 1 km)	WRF- Ensemble Prediction System (4)
36 h	12 h	96-108 h
NCUM-G: 3 h DM: 1 h,	10 m	1 h
Multiclass (fog: 200 m – 1 km and dense fog: \leq 200 m.)	Binary (visibility <1km)	Probabilistic binary (visibility < 1 km or < 500m)
NCUM-G: POD: 0.62, FAR: 0.34, CSI: 0.45, Bias: 1.3 DM: POD: 0.68, FAR: 0.28, CSI: 0.51, Bias: 1.1	Model forecasted onset 1.5 hours early and dissipation: 30 minutes early than actual. Observed visibility ~80 m and forecasted ~200 m.	PoD (0.6-0.7), BSS (positive values for EPS)
<i>In-situ</i> obs.	<i>In-situ</i> obs., viz., ceilometer, visibility	<i>In-situ</i> observations, SW99/G2009 algorithms
DM better for poor visibility and NCUM-G better in formation conducive conditions	Difficulty in capturing inland fog. Limitations due to land-ocean interface resolution and boundary layer dynamics	Ensemble approach outperformed deterministic forecasts for 10 fog events.

Boutle et al. (2016)	Singh et al. (2018)	Jayakumar et al. (2021)
UK (London) (Sep 2013 - Nov 2014)	IGP (Amritsar, Delhi, Lucknow, Varanasi) (2014-2015)	IGP (Delhi), (Dec 2019 - Feb 2020)
United Kingdom Variable resolution Model-UKVM (1.5), London Model LM (0.33)	NCUM-G (17)	Delhi Model with Chemistry and Aerosol Framework (DM-Chem) (0.330)
48 h	24 h	48 h
1h	6 h	1 h
Binary (visibility < 600m)	Binary (visibility <1km)	Binary (visibility <100 m sustained for more than 1 hour)
Frequency Bias Index (0.8 LM, 0.5 UKV), Mean Error	PoD: 0.48-0.5 FAR: 0-0.29 Bias: 0.36-0.59 ETS: 0.06-0.21	Performance was assessed using visibility, aerosol optical depth.
<i>In-situ</i> obs.	<i>In-situ</i> obs., INSAT-3D satellite fog	<i>In-situ</i> obs., radiometer, MODIS satellite fog,
LM struggled with optically thin fog, producing overly thick fog in some scenarios	Reasonable forecast of fog onset and spatial extent but struggled with intensity, due to fixed aerosol assumptions	Integrates aerosol micophysical processes for polluted urban conditions like Delhi

Payra and Mohan (2014)	Steeneveld et al. (2015)	Román-Casón et al. (2016)
Delhi, India (Fog Episodes from 2006-2011)	Cabauw, Netherlands (2005–2009 (case-specific episodes for October and April)	CESAR site (Netherlands), 2008–2013, CIBA site (Spain) 2014–2015
WRF- multirule diagnostic (MRD) (2)	Weather research and forecasting (2.5), HARMONIE	WRF and statistical model (2.5)
48 h	48 h	48 h (6 h spin up)
30 m	1 h	1 h
Binary (visibility < 1km)	Binary (visibility < 1 km)	Binary (visibility < 1 km)
95% accuracy for foggy/non-foggy classification; onset time within 30-90 mins for 84% cases.	Onset timing errors: WRF accurate, HARMONIE late, fog depth: WRF 100 m thinner than observed, dissipation: WRF too early, LWC under/overestimated.	PoD: 0.867 (CESAR), 0.6(CIBA) FA: 0.217(CESAR), 0.357(CIBA)
<i>In-situ</i> obs.	In-situ observations from the Cabauw Tower and synoptic weather stations	<i>In-situ</i> obs.
Postprocessing using MRD improved diagnostics for fog events.	WRF modelled radiation fog well but struggled with dissipation timing, while HARMONIE captured stratus-lowering instead of radiation fog	Captured fog conditions well but struggled with timing errors and spin-up sensitivity over CIBA

Croft et al. (1997)	Zhou et al. (2007)	Tang et al. (2009)
Gulf Coastal States, USA (1993-1995)	Continental United States	Southern England (Benson and High Wycombe) (Dec 9-10 , 2003)
Conceptual Model	NCEP Short-Range Ensemble Forecast (SREF) system (32)	United Kingdom Met Office Unified Model Single Profile Forcing (1)
6-24 h	48-87 h	12 h
Binary (<800 m)	Probabilistic binary (Rel. humidity at 2m : 100%, cloud base < 10 m, and cloud top < 300 m)	Binary (visibility <200m)
Correlation: 0.267 (6-hour fog forecast at Jackson).	PoD : 0.6 FAR : 0.3	Onset errors: 1–2 hours early (Benson), ~3 hours late (High Wycombe); improved after 6–7 hour spin-up
<i>In-situ</i> obs., radiosondes, satellite imagery	NOAA NESDIS satellite fog products	<i>In-situ</i> obs., radiosonde
Operational fog forecasting using mesoscale and microphysical processes lacks quantitative performance metrics.	Captures fog probability distributions well but struggled with fog intensity (no LWC predictions)	Faces issues during spin-up and struggles with fog onset in complex terrain

A 4.2 FogCast performance with and without lagged input features

Table A4.2. Comparison of model performance with and without lagged features

Metric	Lagged features	Lead time					
		6 hours	12 hours	1 day	2 days	5 days	10 days
CSI	Present	0.440	0.436	0.422	0.399	0.371	0.362
	Absent	0.370	0.365	0.366	0.365	0.363	0.363
PoD	Present	0.766	0.751	0.724	0.668	0.703	0.712
	Absent	0.688	0.658	0.659	0.669	0.681	0.752
Median aleatoric uncertainty	Present	0.282	0.263	0.301	0.246	0.366	0.364
	Absent	0.372	0.340	0.385	0.383	0.389	0.396
Median epistemic uncertainty	Present	0.054	0.038	0.052	0.047	0.072	0.069
	Absent	0.055	0.053	0.058	0.056	0.068	0.063

A 4.3 Model performance during LOOCV

Table A4.3. Model performance for different cities in the test set during the leave-one-out cross-validation method (LOOCV).

	No. of fog observations	Fog proportion in data (%)	CSI	OA	PoD	Precision	FAR
Agra	42	19.33	0.62	0.90	0.84	0.72	0.09
Amritsar	710	24.50	0.38	0.64	0.89	0.40	0.44
Delhi	802	25.33	0.41	0.79	0.60	0.58	0.15
Gorakhpur	51	23.33	0.51	0.87	0.57	0.82	0.04
Gaya	29	3.33	0.22	0.93	0.45	0.30	0.05
Kolkata	87	2.67	0.10	0.86	0.45	0.12	0.13
Lucknow	744	23.50	0.45	0.78	0.74	0.53	0.21

A 4.4 Reliability diagram

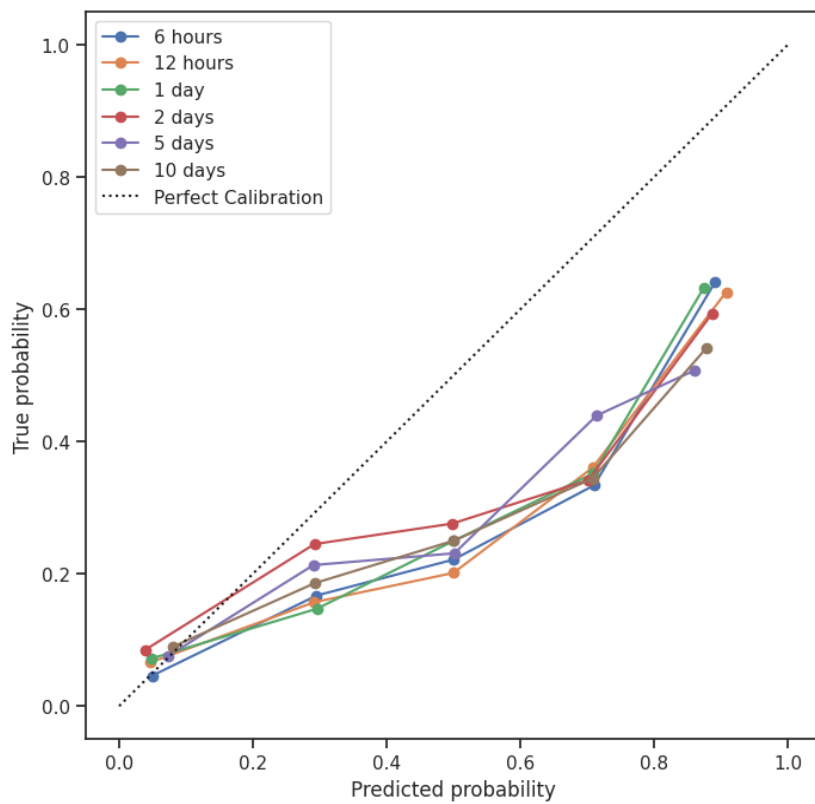


Fig. A4.1. Reliability diagram showing the calibration of the FogCast for different lead times in different colours. The dotted line represents the perfectly calibrated classifier.